Defect and diffusion studies in germanium

MARTIN CHRISTIAN PETERSEN

Department of Physics and Astronomy
Aarhus University, Denmark

PhD thesis
January 2010

This thesis is submitted to the Faculty of Science at Aarhus University in order to fulfill the requirements of obtaining a PhD degree in physics. The work has been carried out under the supervision of Arne Nylandsted Larsen at the Department of Physics and Astronomy (IFA).

Acknowledgments

First of all, I would like to express my thanks to Arne Nylandsted Larsen for competent supervision. I would furthermore like to thank Vladimir Kolkovsky for our collaboration, and in particular for teaching me about Laplace DLTS, during his post doc position in Aarhus. Thanks also go to Abdelmadjid Mesli from InESS, CNRS/ULP in France for his collaboration and for always being helpful in discussing physics. Also his colleague Yann Le Gall is thanked for implanting various elements to produce SIMS references. Additionally I would like to express my deep gratitude to Margareta Linnarsson from FTE, KTH in Sweden for taking her time to do SIMS measurements with and for me.

I would also like to thank John L. Hansen and Pia Bomholt from our group for being very helpful in preparing samples and helping out on technical issues. The electronics department and the workshop have been very helpful as well which I am thankful for.

I am grateful for my friends and fellow physicists Amélie Têtu and Maria F. Jensen helping to proofread the thesis. All my friends and colleagues should know that I appreciate all the time spent and fun had with them during the past 8+ years. Without them it would have been much harder.

Last but not least, my warmest thanks go to my family for their love and support. I owe my sincerest gratitude to Mikala for the extra load she has been pulling at home during my thesis writing.

Martin Christian Petersen,
Aarhus, January 2010.

Contents

List of Publications

List of publications relevant to this thesis

I. **M. Christian Petersen**, C. E. Lindberg, K. Bonde Nielsen, A. Mesli, A. Nylandsted Larsen, *DLTS studies of irradiation-induced defects in p-type germanium*, Materials Science in Semiconductor Processing **9**, 597–599 (2006)

II. Vl. Kolkovsky, **M. Christian Petersen**, A. Nylandsted Larsen, *Alpha particle irradiation-induced defects in n-type germanium*, Applied Physics Letters **90**, 112110 (2007)

III. Vl. Kolkovsky, **M. Christian Petersen**, A. Mesli, J. Van Gheluwe, P. Clauws, A. Nylandsted Larsen, *Gallium interstitial in irradiated germanium: Deep level transient spectroscopy*, Physical Review B **78**, 233201 (2008)

IV. Vl. Kolkovsky, **M. Christian Petersen**, A. Nylandsted Larsen, A. Mesli, *No trace of divacancies at room temperature in germanium*, Materials Science in Semiconductor Processing **11**, 336–339 (2008)

V. A. Mesli, L. Dobaczewski, K. Bonde Nielsen, Vl. Kolkovsky, **M. Christian Petersen**, A. Nylandsted Larsen, *Low-temperature irradiation-induced defects in germanium: In situ analysis*, Physical Review B **78**, 165202 (2008)

VI. Vl. Kolkovsky, **M. Christian Petersen**, A. Mesli, A. Nylandsted Larsen, *Low-temperature irradiation induced defects in p-type Ge*, In press (Physical Review B)

VII. **M. Christian Petersen**, A. Nylandsted Larsen, A. Mesli, *The di-vacancy defect in germanium*, In preparation

Other publications

i. J.S. Jensen, G. Franzo, T.P.L. Pedersen, R. Peireira, J. Chevallier, **M.C. Petersen**, B.B. Nielsen, A. Nylandsted Larsen, *Coupling between Ge-nanocrystals*

and defects in SiO2, Journal of Luminescence, vol. **121**, s. 409-412 (2006)

ii. S. Schneider, H. Bracht, **M. C. Petersen**, J. Lundsgaard Hansen, A. Nylandsted Larsen, *Proton irradiation of germanium isotope multilayer structures at elevated temperatures*, Journal of Applied Physics **103**, 033517 (2008)

iii. A. Nylandsted Larsen, H. Juul Pedersen, **M. Christian Petersen**, V. Kolkovsky, V. Privitera and A. Mesli, *The di-interstitial in proton irradiated silicon*, Submitted

CHAPTER 1

Introduction

Germanium (Ge) is the ancestor of all modern semiconductor technology, in the sense that it was the first material used to successfully demonstrate a working transistor in 1947 [Bardeen 1948]. With the commercial advent of the metal oxide semiconductor field-effect transistor (MOSFET) around 1970[1], silicon (Si) however turned out to be a better choice. Not only does it have a very high abundance in the Earth's crust (28%) but has a very stable native oxide, which can be produced at a high quality by direct oxidation. These reasons contributed to Si dominating the semiconductor device industry for decades.

In the quest for ever smaller semiconductor devices Ge has gained renewed interest and use. As the feature size becomes smaller the transistor density increases and with it the heat production. This is a problem that can be helped by using lower driving voltages. To allow this a higher electron and hole mobility, relating the drift current to the applied electric field, is required from the semiconductor. Ge offers two ways of achieving this goal; 1) the typical electron and hole mobilities are 3–4 times higher in Ge than in Si (cf table 2.1) and 2) building the MOSFET channel from strained Si by adding germanium increases the mobility.

To harvest the maximum potential of Ge, as much fundamental knowledge about it as possible is required. What is mostly relevant for device production is the diffusion of impurities and the nature of electronically active defects. The defects play an even more important role for space electronics as cosmic radiation will inevitably introduce these. From a fundamental point of view Ge is also a very interesting system to study, as it is structurally very similar to Si, having only a 4% larger lattice constant. While there has been an increased research activity on Ge over the last few decades, Si is still more well

[1] Intel launched their first microprocessor based on silicon, the 4004, in 1971 `http://en.wikipedia.org/wiki/Intel_4004`

studied. This allows the comparison of obtained Ge results with knowledge from Si to gain a better understanding of defects and diffusion in elemental semiconductors. The first goal of the present PhD project was to add to the knowledge about electronically active defects in Ge, in particular the divacancy. Secondly the goal was to add to existing experiments on diffusion in Ge by an alternative method, namely the study of diffusional broadening of buried impurity layers.

In chapter 2 the theory required to describe the methods used to study diffusion and electronically active defects in this work is introduced. Chapter 3 outlines the experimental setups used. Chapter 4 is on electronically active defects in Ge studied by transient spectroscopies. Chapter 5 is on the investigation of dopant diffusion studied by SIMS.

CHAPTER 2

Basics: theory and methods

Contents

2.1 Electronic structure of Ge

Being a solid Ge has a band structure formed as a consequence of many body interactions. This structure is shown in figure 2.1 with that of Si included for comparison from [Chelikowsky 1976]. Just as Si, Ge crystallizes in the diamond structure giving a band gap. At 0 K all states below the gap are occupied by electrons while all above the gap are empty, thus yielding a semiconductor. As shown the smallest band gap is indirect between the Γ and L point in reciprocal space. The band(s) at Γ right below the band gap is called the valence band (VB) while that at L right above the band gap is called the

conduction band (CB). At room temperature (RT, 300 K) the size of the band gap is 0.66 eV while increasing with decreasing temperature to 0.74 eV at a temperature of a few K [Macfarlane 1957]. Fundamental parameters of Si and Ge (at RT) are listed in table 2.1. The thermally generated intrinsic carrier con-

Property	**Si**	**Ge**
Atomic weight	28.09	72.60
Lattice constant [nm]	0.543	0.565
Dielectric constant	$11.7 \cdot \epsilon_0$	$16.0 \cdot \epsilon_0$
Melting point (°C)	1415	938
Bandgap (eV)	1.12	0.66
n_i(300 K) (cm^{-3})	1.5×10^{10}	2.4×10^{13}
Relative effective masses (density of states)		
Electron	1.08	0.55
Hole	0.56	0.37
Typical (low doping) values		
Electron mobility ($cm^2/V \cdot s$)	1350	3900
Hole mobility ($cm^2/V \cdot s$)	480	1900

Table 2.1: Comparison of some fundamental properties of Si and germanium at RT.

centration as a function of temperature measured by [Morin 1954] is shown in figure 2.2.

2.1.1 Defects and carrier dynamics

Any deviation from the perfect diamond structure periodicity can give electronic states that are not present in the pure band structure. Not all such structural defects are electronically active in the sense that they yield electronic states inside the forbidden band gap, but those that do are the ones that have the strongest effect on a semiconductor. In this case the deviation is commonly referred to as a *defect*, a *center* or a *trap*.

Point defects are a class of defects that do not extend over many lattice sites and those are the main focus of this work. Possibly the simplest case of these

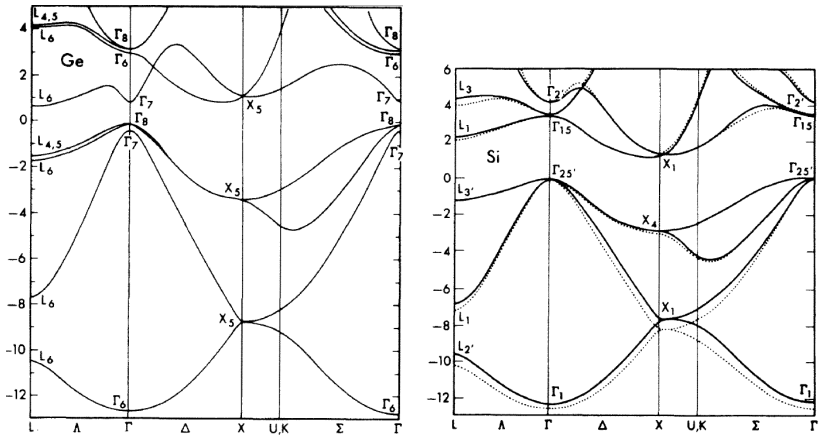

Figure 2.1: The electronic band structure of Ge (left) and Si (right).

are substitutional impurities. When these are from group IV of the periodic table they do not in general provide states in the band gap but do however modify the size of the band gap when present at relatively high concentrations (on the order of percent).

A defect state gives rise to dynamic behavior as illustrated in figure 2.3; when empty it can capture an electron from the CB at L with the rate c_n or emit a hole to the VB at Γ with the rate e_p. Which rate is higher depends on the nature of the defect, the temperature and the carrier concentrations. For example a negatively charged defect would typically be more reluctant to capture electrons than a positively charged one. When the defect has been filled with an electron it can now emit the electron to the CB at a rate e_n or capture a hole from the VB at a rate c_p.

The notation for energy levels in this thesis is as follows. An energy level is labeled by Ex if it is observed in n-type ('E' for electron) where x is the distance from the conduction band in meV, as in E100. If the energy level is observed in p-type it is instead labeled Hy ('H' for hole) where y is the distance to the valence band in meV, as in H100. When the charge states of the defect are known the notation $\mathrm{X}^{(u/v)}$ is used where X is a label describing the defect, u is the charge state of the defect when the energy level is occupied by an electron, and v the charge state when the energy level is empty. If a defect is/contains an impurity atom in a interstitial site this is denoted by subscript 'i', as for example interstitial boron $\mathrm{B_i}$. Likewise a substitutional impurity is

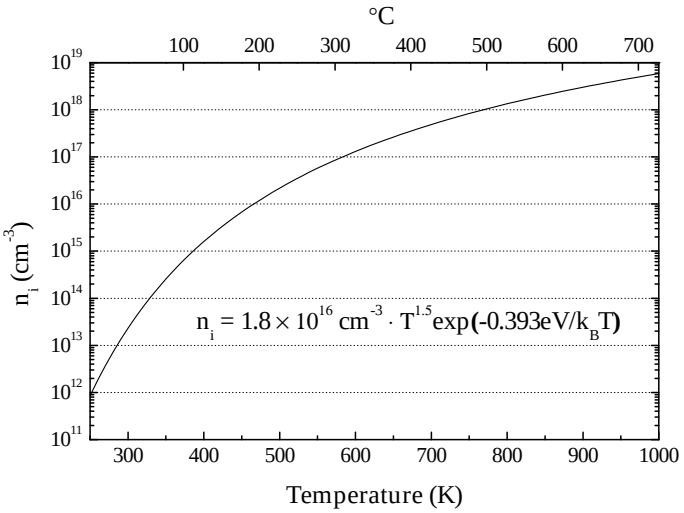

Figure 2.2: The intrinsic carrier concentration in Ge as a function of temperature from 250 K to 1000 K based on [Morin 1954]. The equation shown on the figure is the function fitted to the measured data by the authors.

labeled with subscript 's', such as the boron interstitial-boron substitutional pair B_i–B_s. Finally an energy level where the defect is negatively charged when the level is occupied by an electron is called an acceptor level (single-acceptor ~ singly negative, double-acceptor ~ doubly negative etc.). Likewise an energy level that yield a positively charged defect when not occupied by an electron is called a donor level. An energy level signature will be used loosely to refer to the actual defect as well, even though this is not technically correct; as in "the H100 defect", which should actually be "the defect responsible for the energy level H100".

The impact of such an energy level, introduced by a defect, on an actual semiconductor device depends on the relative magnitude of the capture and emission rates. In the event that $e_n, e_p \ll c_n, c_p$ the defect may act as a recombination center[1] which can in fact be beneficial for making fast devices but detrimental for solar cells. The opposite process dominates if $c_p, c_n \ll e_p, e_n$ and the result is a generation center[2] which will lead to leakage currents in depletion-regions. Finally if the energy level mainly interact with one of the

[1] By alternating between electron capture and hole capture.
[2] By alternating between electron emission and hole emission.

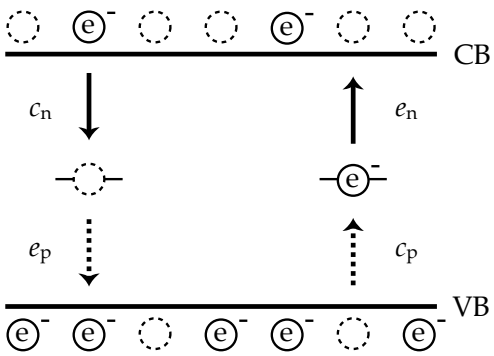

Figure 2.3: Illustration of the dynamics an energy state in the band gap can give rise to. The solid arrows show electron capture/emission while the dashed arrows show hole capture/emission. When empty (left) the defect can capture an electron from the CB (c_n) or emit a hole to the VB (e_p). If populated by an electron the defect can emit this to the CB (e_n) or capture a hole from the VB (c_p).

bands, it will lead to a change in equilibrium carrier concentration.

Expressions for the capture rates are simply given by a capture cross section times the flux of carriers:

$$c_n = \sigma_n \langle v_n \rangle n \tag{2.1}$$

$$c_p = \sigma_p \langle v_p \rangle p \tag{2.2}$$

with the carrier mean thermal velocity given by[3]

$$\langle v_{n/p} \rangle = \sqrt{\frac{3k_B T}{m^*_{n/p}}} \tag{2.3}$$

where m^* is the majority carrier effective mass. Denoting the emission rates by e_n and e_p, the total trap concentration N_t and the concentration of traps occupied by an electron with n_t, the resulting rate equation is:

$$\frac{dn_t}{dt} = (e_p + c_n) \cdot (N_t - n_t) - (e_n + c_p) \cdot n_t. \tag{2.4}$$

Now detailed balance states that in thermal equilibrium ($dn_t/dt = 0$) a process and its reverse occur at the same rate, so in that case we may write

$$e_p \cdot (N_t - n_t) = c_p \cdot n_t \qquad \text{and} \qquad c_n \cdot (N_t - n_t) = e_n \cdot n_t. \tag{2.5}$$

[3]To be precise this is actually the root mean square of the carrier thermal velocity.

The thermal equilibrium occupation is governed by Fermi-Dirac statistics, so:

$$\frac{n_\mathrm{t}}{N_\mathrm{t}} = \frac{1}{1 + \frac{g_0}{g_1}\exp\left(-\frac{E_\mathrm{F}-E_\mathrm{t}}{k_\mathrm{B}T}\right)} \tag{2.6}$$

where g_0 and g_1 are degeneracies for the state being empty and filled respectively. Finally the carrier concentrations can be approximated by Boltzmann statistics:

$$n = N_\mathrm{c}\cdot\exp\left(-\frac{E_\mathrm{c}-E_\mathrm{F}}{k_\mathrm{B}T}\right) \qquad \text{and} \qquad p = N_\mathrm{v}\cdot\exp\left(-\frac{E_\mathrm{F}-E_\mathrm{v}}{k_\mathrm{B}T}\right) \tag{2.7}$$

where N_v is the effective density of states in the VB while N_c is the same for the CB, both proportional to $T^{1.5}$. Combining the above three equations results in expressions for the emission rates:

$$e_\mathrm{n} = \sigma_\mathrm{n}\langle v_\mathrm{n}\rangle\frac{g_0}{g_1}N_\mathrm{c}\exp\left(-\frac{E_\mathrm{c}-E_\mathrm{t}}{k_\mathrm{B}T}\right) = \sigma_\mathrm{n}\frac{g_0}{g_1}\gamma_\mathrm{n}T^2\left(-\frac{E_\mathrm{c}-E_\mathrm{t}}{k_\mathrm{B}T}\right) \tag{2.8}$$

$$e_\mathrm{p} = \sigma_\mathrm{p}\langle v_\mathrm{p}\rangle\frac{g_1}{g_0}N_\mathrm{v}\exp\left(-\frac{E_\mathrm{t}-E_\mathrm{v}}{k_\mathrm{B}T}\right) = \sigma_\mathrm{p}\frac{g_1}{g_0}\gamma_\mathrm{p}T^2\left(-\frac{E_\mathrm{t}-E_\mathrm{v}}{k_\mathrm{B}T}\right). \tag{2.9}$$

The prefactor γ only differs for the two cases by the carrier effective mass and is given by

$$\gamma_\mathrm{n/p} = m^*_\mathrm{n/p}\frac{\sqrt{3}\cdot 2(2\pi)^{3/2}}{h^3} \tag{2.10}$$

where h is the Planck constant. Both σ and E_t can be temperature dependent in the sense that (using electron capture/emission as the example, extension to holes is straightforward)

$$\sigma_\mathrm{n}(T) = \sigma_{\mathrm{n}\infty}\exp\left(-\frac{\Delta E_{\mathrm{n}\sigma}}{k_\mathrm{B}T}\right), \qquad E_\mathrm{c}-E_\mathrm{t} = \Delta G_\mathrm{n} = \Delta H_\mathrm{n} - T\Delta S_\mathrm{n} \tag{2.11}$$

where ΔG_n is the change in the Gibbs free energy of the crystal due to the transition; ΔH_n and ΔS_n are the corresponding enthalpy and entropy changes. While this is not the only possible temperature dependence of σ_n, a given temperature dependence can generally be approximated by (2.11) over a sufficiently narrow temperature interval. Incorporating this gives the final expression for emission:

$$\boxed{e_\mathrm{n} = \sigma_\mathrm{na}\gamma_\mathrm{n}T^2\cdot\exp\left(-\frac{E_\mathrm{na}}{kT}\right)} \tag{2.12}$$

where

$$\sigma_{\mathrm{na}} = \sigma_{\mathrm{n}\infty} \cdot \frac{g_0}{g_1} \exp\left(\Delta S_{\mathrm{n}}/k_{\mathrm{B}}\right), \quad E_{\mathrm{na}} = \Delta H_{\mathrm{n}} + \Delta E_{\mathrm{n}\sigma}. \tag{2.13}$$

Exchanging g_0 and g_1 while replacing n by p, results in the corresponding equation for holes.

2.1.2 Defect introduction and irradiation of a solid

The thermally generated concentration of point defects at feasible temperatures for defect measurements (around RT and below) is way too low to be studied. We use MeV particle irradiation to introduce defect concentrations suitable for measurement. The direct effect of such energetic particles is the kick out of atoms from lattice sites due to scattering on these atoms. In the event that more than the threshold energy, is transferred to the lattice atom in the collision, a vacancy and a self-interstitial are created. This threshold is found to be in the region of 10–30 eV for Ge [Loferski 1958, Callcott 1967]. In addition the newly generated self-interstitial can have gained enough energy to initiate further defect creation events leading to a cascade of defect formation. Higher order defects such as di-vacancies can be formed directly in the collision cascade when two vacancies are formed next to each other. Subsequently secondary defects may form as some of these primary defects become mobile.

Irradiation with electrons create the simplest damage due to the much lower mass as compared to protons or alpha particles. Momentum conservation prevents the electron from transferring a substantial part of its energy[4] and thus the scattered lattice atom will not be able to induce more than a few displacements itself. Due to the negative charge however, the electrons could be expected to have a higher cross section for scattering, making the average distance between damage events for a single particle shorter. A review on radiation damage in semiconductors is given in [Srour 2003].

The implantation of elements from the periodic table can be simulated using the program SRIM, Stopping and Range of Ions in Matter [Ziegler 2008]. This program uses Monte Carlo simulation to simulate the interaction of the

[4] A simple relativistic calculation on momentum and energy conservation gives an upper limit on the transfered energy of about 178 eV, given that the electron has an energy of 2 MeV and collides head on with a free Ge atom.

impinging ions with the solid in question. Of special interest for this thesis, the depth profile of the produced vacancies as well as that of the implanted ions can be computed.

2.1.3 Diode structures

In order to detect the defects present in a semiconductor, a suitable device is needed. As it turns out a diode structure is perfect for this purpose since the capacitance is sensitive to the charge present in the space charge region (SCR). In order to keep the analysis sufficiently simple a Schottky barrier diode (metal-semiconductor junction) or a one-sided pn junction (n^+p or p^+n) is needed. As the junction is fabricated carriers move into the opposite part of the device exposing charged donor/acceptor atoms and thus setting up an electric field, illustrated by figure 2.4. This continues until the electric field is strong enough to prevent further movement of the edge of this so called space charge region (SCR). The approximation that the SCR edge is abrupt will be adopted. That is, inside the SCR no mobile charge are present and outside there is no net electric field.

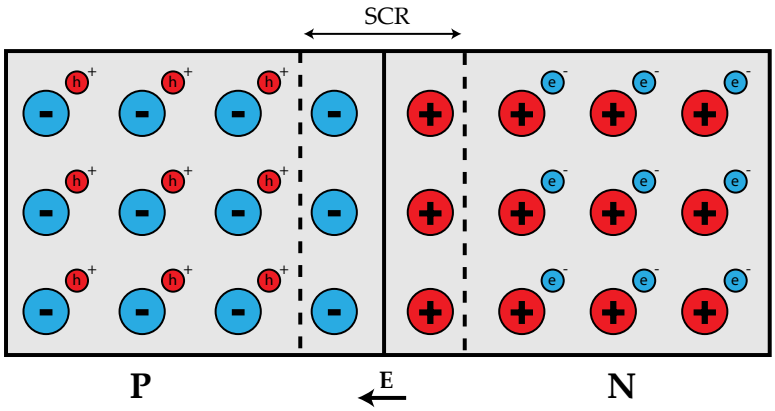

Figure 2.4: Illustration of the formation of a SCR (inside the dashed lines) at a pn junction. The big circles represent the ionized dopants and the small circles electrons and holes. As the two types of materials are brought together (symbolically) there is a strong gradient of electron and hole concentration at the interface. This causes electrons to diffuse into the p side (left) and holes to diffuse into the n side (right), leaving a net charge due to ionized donor and acceptor atoms. The electric field set up by the exposed charge opposes the diffusion, leading eventually to equilibrium.

Equilibrium is described by the built-in potential (V_{bi}) of the diode which is the voltage drop corresponding to the electric field in the SCR with no external bias on the diode. By applying an external negative potential on the p-side of the junction relative to the n-side the SCR width, x, can be increased thus increasing the detection region. This condition is known as reverse bias, and in this case the bias is usually denoted with V_{r}.

In the following the diode capacitance will be related to the applied voltage and the dopant concentration. [Miller 1977] is the main inspiration for the derivations. In what follows $\epsilon = 16.0 \cdot \epsilon_0$ is the dielectric constant of Ge and A is the cross-sectional area of the diode.

The effect of making the reverse bias slightly more negative on the diode by adding ΔV_{r} (< 0), is to expand the SCR by an amount Δx since more charge must be uncovered to reflect the increased voltage drop. This increases the electric field by a constant amount ΔE in the region $0 \rightarrow x$. Since Δx is assumed to be small[5] (compared to x) the potential change is due to the increased electric field in this region:

$$\Delta V_{\mathrm{r}} \approx -\int_0^x |\Delta E| \, \mathrm{d}x' = -|\Delta E| \cdot x. \tag{2.14}$$

From Gauss's law ΔE, due to the charge uncovered in the region $x \rightarrow x + \Delta x$, can be calculated:

$$\Delta E = \int_{x+\Delta x}^{x} \frac{\rho(x)}{\epsilon} \, \mathrm{d}x' \approx -\Delta x \frac{qN(x)}{\epsilon} \tag{2.15}$$

where $\rho(x) = qN(x)$ is the charge density at x and q is the net charge on the ionized dopant. Note that Gauss's law also allows the calculation of the electric field inside the SCR[6]. Combining the two above expressions and introducing the junction capacitance $C \approx -|\Delta Q|/\Delta V_{\mathrm{r}}$, where ΔQ is the charge uncovered by changing V_{r} by ΔV_{r}, gives

$$\Delta V_{\mathrm{r}} \approx x \Delta x \frac{|q|N(x)}{\epsilon} = x \frac{|\Delta Q|}{A\epsilon} \Rightarrow \tag{2.16}$$

$$\boxed{C = \frac{A\epsilon}{x}}. \tag{2.17}$$

[5] The term dropped is of order Δx^2.

[6] For a uniform dopant concentration the result is that the absolute electric field increases linearly with distance from the neutral region to the junction, up to a maximum value of $E_{\mathrm{max}} = 2V_{\mathrm{r}}/x_{\mathrm{r}}$.

Thus the diode in reverse bias behaves as a parallel plate capacitor and the capacitance is directly related to the SCR width. Taking the limit of infinitesimal changes before introducing the capacitance, the following relationship results:

$$\frac{\epsilon}{|q|N(x)} = x \cdot \frac{\partial x}{\partial V_\mathrm{r}} = x \cdot \frac{\partial x}{\partial C}\frac{\partial C}{\partial V_\mathrm{r}} = -\frac{(\epsilon A)^2}{C^3}\frac{\partial C}{\partial V_\mathrm{r}} = \frac{(\epsilon A)^2}{2}\frac{\partial}{\partial V_\mathrm{r}}\left(\frac{1}{C^2}\right) \tag{2.18}$$

and finally:

$$\boxed{N\Big(x(V)\Big) = \frac{2}{\epsilon A^2 e}\left(\frac{\partial C^{-2}}{\partial V_\mathrm{r}}\right)^{-1}} \tag{2.19}$$

where $|q|$ has been replaced with e, the elementary charge, since dopant atoms are usually only singly charged. This allows the depth profiling of the carrier concentration, or more precisely the dopant concentration, since profiling is possible below the temperature where the carriers are starting to freeze in. The conversion from reverse voltage to depth can be done directly with (2.17) when $C(V)$ is known.

If $N(x)$ is known the capacitance as a function of reverse bias follows by integration. In the ideal case when N is constant as a function of depth the result is:

$$\frac{1}{C(V_\mathrm{r})^2} = \int_0^{V_\mathrm{bi}+V_\mathrm{r}} \frac{2}{\epsilon A^2 e N}\mathrm{d}V \Rightarrow$$
$$\boxed{C(V_\mathrm{r}) = A\sqrt{\frac{\epsilon e N}{2(V_\mathrm{bi}+V_\mathrm{r})}}}. \tag{2.20}$$

When N varies with depth however it is much simpler to use (2.18) with separation of the variables and integration to get $x(V_\mathrm{r})$ which is easily transformed into $C(V_\mathrm{r})$ using (2.17),

$$\frac{e}{\varepsilon}\int_0^{x(V_\mathrm{r})} x \cdot N(x)\,\mathrm{d}x = \int_0^{V_\mathrm{bi}+V_\mathrm{r}} \mathrm{d}V = V_\mathrm{bi} + V_\mathrm{r}. \tag{2.21}$$

Along with the Capacitance-Voltage characteristics another important tool in analyzing a diode is the Current-Voltage characteristics given ideally by

$$I = I_s\left[\exp\left(\frac{eV}{kT}\right) - 1\right] \tag{2.22}$$

where V is now the potential applied to the p-side relative to the n-side, and I_s is the saturation current, a device parameter. This relation is that of a rectifier and checking that the diode does in fact act as such is useful in quickly discarding poor samples. Often there are both series and parallel resistance circuit components leading to slight deviations from (2.22).

2.1.4 Deep level transient spectroscopy (DLTS)

The presence of charged defects in the SCR in addition to the dopants will modify the charge profile in the SCR, $N(x)$. It is thus apparent from (2.20) that the capacitance will reflect the presence of charged defects in the SCR. To include the presence of a majority carrier trap, which then contributes to the total charge with the opposite sign of the dopants, N is substituted with $N - n_\mathrm{t}$ where n_t is the concentration of occupied traps and N is understood to contain the contribution from unoccupied traps[7] that may have a net charge. Assuming $n_\mathrm{t} \ll N$ and inserting it in (2.20) with C_∞ denoting the capacitance when the traps are empty then gives

$$\begin{aligned} C(V_\mathrm{r}) = C_\infty(V_\mathrm{r}) + \Delta C(V_\mathrm{r}) &= C_\infty(V_\mathrm{r}) \sqrt{\frac{N - n_\mathrm{t}}{N}} \\ &\approx C_\infty(V_\mathrm{r}) \left(1 - \frac{n_\mathrm{t}}{2N}\right) \Rightarrow \boxed{\frac{n_\mathrm{t}}{N} = -\frac{2\Delta C}{C_\infty}}. \end{aligned} \tag{2.23}$$

The doping level, N, sets a natural scale for measurable defect concentrations. A change in capacitance down to a few fF's is possible to measure while n_t should not exceed more than about 10% of N in order to keep the above approximation valid. It should be noted that (2.23) assumes a uniform concentration of dopants and defects which is often not precisely true. One correction, even in the case of uniform defect and dopant concentration, is given later in (2.40). The present expression however serves the purpose of illustrating the technique nicely. Unless the emission rate as given by (2.12) is very low, due to a low temperature, majority carrier traps will generally be empty in the SCR at thermal equilibrium since there are no mobile carriers to capture.

Let us now assume we have fully populated an electron trap inside the

[7] It is implicitly assumed here that only one carrier is captured/emitted in a given transition.

SCR in an n-type[8] diode somehow, present at the uniform concentration N_t. As a function of time, t, the concentration and thus the capacitance will then decay with the emission rate given by (2.12):

$$n_t(t) = N_t \exp\Big(-e_n(T)\cdot t\Big) \Rightarrow \frac{\Delta C}{C_\infty} = -\frac{N_t}{2N}\exp\Big(-e_n(T)\cdot t\Big). \tag{2.24}$$

In this idealized case the capacitance transient at a fixed temperature, T, then directly gives the emission rate, $e_n(T)$, and the total trap concentration N_t by exponential fitting.

By sampling e_n at a number of temperatures E_{na} and σ_{na} can then be found. This is particularly easy if $\ln[e_n(T)/T^2]$ is plotted as a function of $1/T$, known as an Arrhenius plot (of the T^2 corrected emission rate), as this is theoretically a straight line from (2.12):

$$\ln\Big[e_n(T)/T^2\Big] = \ln(\gamma_n\sigma_{na}) - \frac{E_{na}}{kT}. \tag{2.25}$$

The simplest way to populate traps is to shortly move the edge of the SCR towards the junction by increasing V from V_r to a value V_p, thereby contracting the SCR. Traps in the region $x(V_p) \rightarrow x(V_r)$ will then capture majority carriers according to (2.1), since it is no longer part of the SCR. After a short time, on the order of microseconds or lower and up to milliseconds (cf section 2.1.4.1), τ, the voltage is returned to V_r with the result that the traps in the affected region are now filled and emission dominates. This process is illustrated in figure 2.5.

In reality emission rates are more or less broadened, and often more than one energy level contributes to the transient. The real transient is given by

$$\Delta C = \int_0^\infty F(s)\exp(-st)\,\mathrm{d}s \tag{2.26}$$

where s is emission rate and F is a spectrum containing a peak for every emitting energy level. The conventional way to extract these components from the capacitance transient has been to use a so called rate-window and scan the temperature. This is the implementation of a linear filter that takes the

[8] To get the equivalent expressions for p-type, n can be replaced by p if n_t is replaced with the corresponding hole expression $p_t = N_t - n_t$.

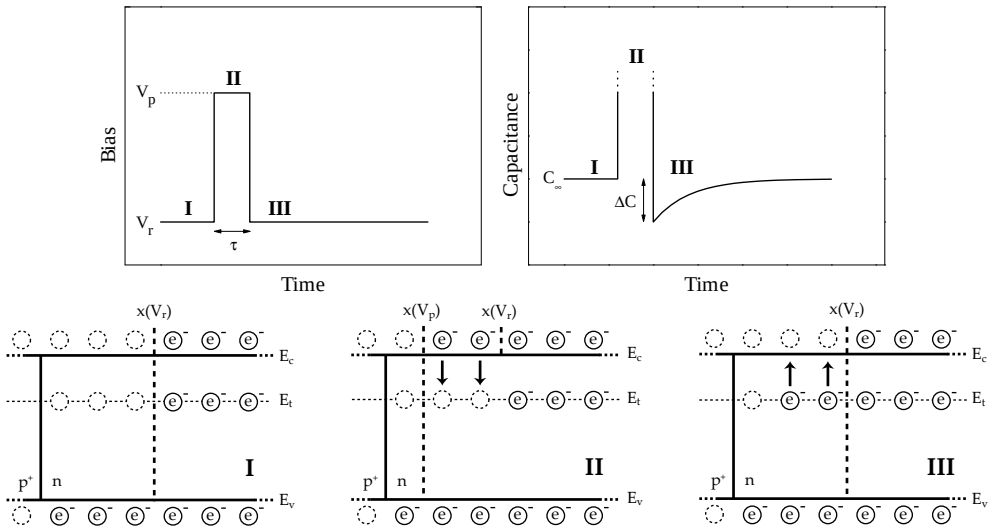

Figure 2.5: Illustration of the introduction of a capacitance transient by pulsing the bias on the diode (an electron trap is used here). The upper left graph shows how the bias is varied with an indication of the three different regimes (I) steady state, (II) carrier capture and (III) carrier emission. In the upper right graph the effect on the capacitance is shown. The lower illustration shows the state of the SCR in the different modes. (I) a steady state has been reached and inside the SCR the trap level, indicated by E_t, is predominantly empty. (II) increasing the bias on the diode shrinks the SCR thereby allowing the trap to capture carriers in the region $x(V_p) \rightarrow x(V_r)$. (III) as the bias is returned to the lower value capture no longer takes place and emission becomes the dominant process giving a transient in the capacitance.

transient as input and outputs a number, here called S. This number has the property that it is maximum when the emission rate has a set value. This will then suppress components that are sufficiently far away in emission-rate. As a function of temperature the result is a spectrum, $S(T)$, with peaks at the temperatures corresponding to the individual traps having the predetermined value of the emission rate. Repeating the process for different rate-windows enables the construction of an Arrhenius plot as $S(T)$ gives matching values of e (set by the rate-window) and T. Despite the fact that this technique of making a DLTS spectrum as a function of temperature is much slower than analyzing the transient at a fixed temperature, as described below, it is extremely useful in getting an overview of the energy levels present. Preliminary analy-

sis will thus always include one or more conventional DLTS spectra.

There are two main types of rate-windows in use for producing DLTS spectra known as the double box-car averager and the lock-in amplifier. The former is discussed in the original paper on the conventional DLTS technique [Lang 1974a] while both are described in a later review on DLTS systems [Day 1979]. The box-car averager in its simplest form gets the output signal by subtracting the capacitance value at two specific times in the transient,

$$S_{\text{boxcar}}(T) = C(t_1) - C(t_2) = -\Delta C\left[\exp(-e \cdot t_1) - \exp(-e \cdot t_2)\right] \tag{2.27}$$

$$= -\Delta C \cdot \exp(-e \cdot t_1)\Big[1 - \exp\Big(-(\alpha - 1)e \cdot t_1\Big)\Big] \tag{2.28}$$

where $\alpha = t_2/t_1$ and a mono-exponential transient has been used for demonstration, $C(t) = C_0 - \Delta C \cdot \exp(-e \cdot t)$. The sampling points can be made into gates of a certain time width to decrease the level of noise in the spectrum.

The lock-in amplifier uses a longer part of the transient by integrating it weighed with +1 the first half of the time and -1 the last half of the time apart from a gate-off window at the beginning of the transient. Only the lock-in amplifier rate-window has been used in this work although the box-car averager rate-window is selectable in the conventional DLTS function of the Laplace DLTS software.

The advantage of the former is a lower level of noise due to the integration of the transient while the latter is simpler in implementation. However when the processing of the transient is done in a computer program this simplicity it not really an issue. The rate window signal, before normalization, from the lock-in amplifier rate window used by the DLS-83d can be approximated by[9]:

$$S_{\text{lock-in}}(T) = f\left(\int_0^{1/(2f)} C(t + \tau + 1/(20f))\,\mathrm{d}t - \int_{1/(2f)}^{1/f} C(t + \tau + 1/(20f))\,\mathrm{d}t\right) \tag{2.29}$$

$$= \Delta C \cdot f \frac{\exp\Big(-e \cdot [\tau + (20f)^{-1}]\Big)}{e}\left[1 - \exp\left(-\frac{e}{2f}\right)\right]^2 \tag{2.30}$$

where f is the frequency of the lock-in averager ($e_{window} = 2.17f$ in this case), and τ is the filling pulse duration; the same capacitance transient as above has been used.

[9] from the equipment manual

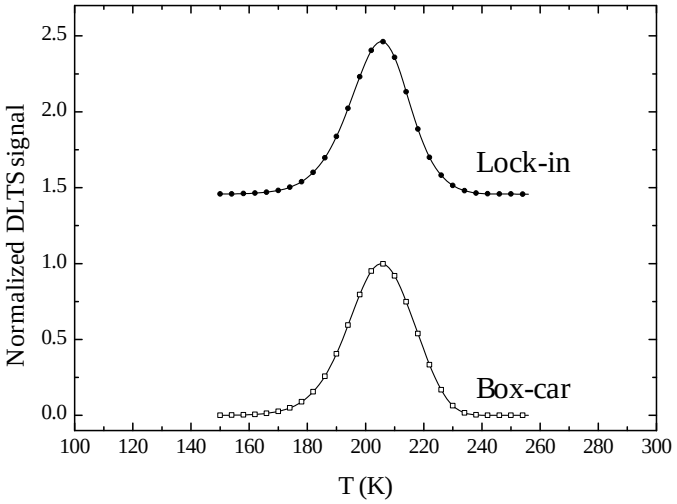

Figure 2.6: Comparison of the double box-car averager (lower) and lock-in amplifier (upper) rate windows. The antimony-vacancy defect in n-type Ge (see 4.3.1 for details) has been used for $e(T)$ in this example. Both rate-windows were set at an emission rate of $e = 500\ \mathrm{s}^{-1}$ and $t_2/t_1 = 10$ was used for the box-car averager. The lock-in algorithm demonstrated is the one used by the DLS-82d DLTS equipment from Semilab.

Figure 2.6 shows calculated DLTS spectra, resulting from the two different types of rate-windows, assuming only one mono-exponential component is present in the transient. It is evident that there is very little difference between the two peaks, although the lock-in version of the peak is slightly narrower. It should be kept in mind though that white noise is not included in this calculation, and with noise present the lock-in approach becomes superior.

2.1.4.1 Determining the capture cross section

The defect signature ($\sigma_{\mathrm{na/pa}}, E_{\mathrm{na/pa}}$) is not as fundamental as the parameters $\sigma_{\mathrm{n/p}}$ and $\Delta H_{\mathrm{n/p}}$. In fact when the capture cross section is not too high[10], it can be determined directly. The method for doing this is based on inspection of (2.4) in the observation region immediately after the beginning of the filling pulse. If the energy level is observed in n-type (p-type) we know that $e_{\mathrm{n}} \gg e_{\mathrm{p}}$

[10]Without special electronics the shortest filling pulse duration is limited to about 1 μs, which limits how high capture cross sections that can be measured, as seen below.

($e_p \gg e_n$), otherwise the level would not show itself to DLTS. Also hole capture (electron capture) does not play a role as the minority carrier concentration is low. Finally electron emission (hole emission) can be neglected at short times when $e_n n_t$ ($e_p[N_t - n_t]$) is small.

Under these conditions, (2.4) reduces to (using η_t instead of n_t to signify trap filling)

$$\frac{d\eta_t}{dt} = c_n \cdot (N_t - \eta_t) \qquad \left(\frac{d\eta_t}{dt} = -\eta_t \cdot c_p \right). \tag{2.31}$$

These differential equations are readily solved giving

$$\eta_t(t) = N_t \cdot \left[1 - \exp(-c_n t)\right] \qquad \left(N_t - \eta_t(t) = N_t \cdot \left[1 - \exp(-c_p t)\right] \right). \tag{2.32}$$

In the discussion of DLTS above, it was implicitly assumed that $c_n \tau \gg 1$ so that $\eta_t(\tau) = N_t$ and the DLTS signal does not depend on τ. For smaller values of τ however, the DLTS amplitude reflects the value of η_t in (2.32), which replaces n_t in the result for ΔC in (2.23):

$$\Delta C(\tau) = -\frac{\eta_t(\tau)}{2N} \cdot C_\infty = \frac{\eta_t(\tau)}{N_t} \Delta C_{max} \tag{2.33}$$

Therefore measuring the DLTS amplitude as a function of filling pulse duration, τ, allows the extraction of c_n (c_p) and thereby σ_n (σ_p) according to (2.1). The easy way to do this is by plotting $\ln[\Delta C(\tau)/\Delta C_{max} - 1]$ as a function of τ; this should give a straight line through (0,0) if the values of τ are low enough, making fitting easy.

The temperature dependence of σ_n (σ_p) can be investigated by repeating the above procedure at different temperatures. Once this has been done the remaining parameters can be calculated. Note however that there is not sufficient information to deduce g_0 and g_1 in (2.13), so these are often implicitly assumed equal.

2.1.4.2 Laplace DLTS

When peaks are overlapping in a DLTS spectrum it can be difficult to extract the temperatures corresponding to the peaks. Numerical methods have been developed known as Laplace inversion to extract the whole emission

spectrum $F(s)$ from the capacitance transient. This improves on the resolution and will, under optimal conditions, allow separation of components as close as about a factor of three in emission rate. The type of DLTS employing these numerical methods is known simply as Laplace DLTS. The details of the Laplace inversion is rather complicated and a detailed review about the extraction of the decay components is given by Istratov and Vyvenko [Istratov 1999]. Fortunately a complete software package has been made for measuring and analysing transients saving the user from the mathematical details [Dobaczewski 2009]. This Laplace DLTS program makes use of three different implementations of Laplace Inversion all using the same basic method to make the problem discrete known as Tikhonov regularization. These three algorithms are named Flog, Ftikreg and Contin. Flog is an algorithm specifically written for the software and the results from this is normally used while the two others are used as a consistency check for the resulting spectrum. The noise in one transient is relatively high, in our case around 25-30 fF. This means that averaging, reducing the noise by about a factor of $\sqrt{K}$ given K transients averaged, is necessary to obtain good results. In addition it is important for the separation of emission components that the duration of a single recorded transient is substantially longer than the corresponding time constant. A good rule of thumb is to have about 10 half lives for the slowest component of interest included in the recorded transient. This amounts to a duration of $10\ln(2)/e \approx 7/e$. A comprehensive review of Laplace DLTS, particularly in connection with this sofware, is given by [Dobaczewski 2004].

2.1.4.3 Defect depth profile

When the dopant concentration, $N(x)$, and/or the defect concentration $n_t(x)$ are not uniform, another expression than (2.23) is needed for describing the capacitance change precisely. A useful expression, when these assumptions are not valid, can be derived by observing from (2.17) that the capacitance change due to a change in the charge in the SCR corresponds to a change in the width of the SCR:

$$\Delta C/C = -\Delta x/x. \tag{2.34}$$

We can thus use (2.16) to determine the signal coming from a small region in voltage δV around V_1 by doing separation of the variables and integration by

parts:

$$V_{\mathrm{bi}} + V_{\mathrm{r}} = \int_0^{V_{\mathrm{bi}}+V_{\mathrm{r}}} \mathrm{d}V = \frac{q}{\epsilon}\int_0^{x(V_{\mathrm{r}})} N(x)x\,\mathrm{d}x. \tag{2.35}$$

The left hand side is constant so the decrease in $N(x)$ due to the defect is balanced by a change in x:

$$\int_{x(V_{\mathrm{r}})}^{x(V_{\mathrm{r}})+\Delta x} N(x)x\,\mathrm{d}x = \int_{x(V_1)}^{x(V_1+\delta V)} N_{\mathrm{t}}(x)x\,\mathrm{d}x = \int_{V_1}^{V_1+\delta V} N_{\mathrm{t}}(x)x\frac{\partial x}{\partial V}\,\mathrm{d}V. \tag{2.36}$$

Using that Δx is very small, assuming that the variation of n_{t} over δV to be negligble, introducing the end result of (2.16) and finally simplifying the notation a bit gives

$$\begin{gathered} N(V_{\mathrm{r}})x(V_{\mathrm{r}})\Delta x = \frac{\epsilon n_{\mathrm{t}}(V_1)}{qN(V_1)}\delta V \Rightarrow \\ \boxed{\delta\left(\frac{\Delta C}{C}\right) = -\left(\frac{\epsilon}{qN(V_{\mathrm{r}})x(V_{\mathrm{r}})^2}\right)\frac{N_{\mathrm{t}}(V_1)}{N(V_1)}\delta V}. \end{gathered} \tag{2.37}$$

This result gives the contribution to the capacitance transient from the region $x(V_1) \rightarrow x(V_1 + \delta V)$ in the SCR. We may note from this result that, as long as the emission-rate does not depend on x, the time dependent factor of the transient does not depend on x since this expression is linear in N_{t}. To extract emission rates it is then sufficient to use (2.23). Using the end result of (2.16) to express (2.37) in terms of depth instead of voltage[11] gives the informative result:

$$\delta\left(\frac{\Delta C}{C}\right) = -\left(\frac{x \cdot n_{\mathrm{t}}(x)\delta x}{N(V_{\mathrm{r}})x(V_{\mathrm{r}})^2}\right). \tag{2.38}$$

From this we can immediately tell that the DLTS signal is more sensitive to defects residing far from the junction compared to defects close to the junction since x measures the distance from the junction in our one-sided junctions and $N_{\mathrm{t}}(x)\delta x$ is the number of defects per area in the slice.

Even when the defect concentration is uniform (2.38) allows a correction of (2.23). This correction is partly due to the so called Debye-tail of carriers which penetrates into the SCR, causing majority carrier capture to be present.

[11] By use of the chain rule.

Furthermore capture is not taking place in the full SCR, and this introduces a correction as well. The penetration length, λ, is defined to [Blood 1992]:

$$\lambda = \sqrt{\frac{2\epsilon|E_F - E_t|}{e^2 N}} \tag{2.39}$$

where N is the doping concentration and E_F is the position of the Fermi level. The absolute value under the square root makes the expression valid for both n- and p-type. Due to this effect the region that contributes to ΔC is $x(V_p) - \lambda \rightarrow x(V_r) - \lambda$. By integrating (2.38) the following corrected version of (2.23) results:

$$\frac{n_t}{N} = -\frac{2\Delta C}{C_\infty} \frac{x(V_r)^2}{[x(V_r) - \lambda]^2 - \left[x(V_p) - \lambda\right]^2}. \tag{2.40}$$

2.1.4.4 Minority carrier injection

So far the conditions discussed (for a n-type diode) have had the minority carrier capture rate, $c_p \approx 0$, since the majority carrier concentration due to doping is usually much higher than n_i ($np = n_i^2$). Thus it has not been relevant if the defect, from its equilibrium charge state inside the SCR, could capture a minority carrier.

There are however conditions under which the minority carrier concentration can be increased. Assuming that the defect has been populated by a minority carrier, it will increase the capacitance since the minority carriers have the same charge sign as the dopants. This is the opposite effect of majority carrier trapping, so minority carrier trapping has a distinct effect on the capacitance transient. Other than the sign of the capacitance change, the transient behavior is the same as a normal majority carrier transient. This form of transient spectroscopy is called minority carrier transient spectroscopy (MCTS).

One obvious method for a n^+p or p^+n diode is to choose a positive bias for V_p, as this causes the injection of carriers across the SCR, as part of the forward current in (2.22). This however requires that $e_p \gg e_n$ (again for n-type), as majority carriers are present as well.

In principle this does not work with Schottky barrier diodes as there is no p-type part to supply holes. However, it has been demonstrated that the high barrier between Au and Ge leads to the formation of an inversion layer, with

a high concentration of holes [Markevich 2004b]. Thus this method works for Au-Ge Schottky diodes as well, clearly demonstrated by several results in the literature fx [Fage-Pedersen 2000].

Another method is the application of pulsed light, instead of voltage pulses (keeping the diode at a constant reverse bias), with an energy exceeding the band gap; this light generates electron-hole pairs in the semiconductor. If the penetration depth of the light $(1/\alpha)$[12] is substantially higher than the SCR width (x_r), the majority of the electron-hole pairs will be generated beyond the SCR. Now, if the minority carrier diffusion length, L_p[13], is larger than the penetration depth, minority carriers will diffuse into the SCR allowing capture. These conditions can be summarized as

$$L_\mathrm{p} > \alpha^{-1} \gg x_\mathrm{r}. \tag{2.41}$$

Figure 2.7 shows the absorption characteristics of Ge at 77 K and 300 K. It is evident from this figure that to satisfy condition (2.41) for the $\mathrm{n^+p}$ Ge mesa-diodes (where the pn-junction is at a depth of 1.7 μm), the photon energy has to be less than 0.81 eV, otherwise α^{-1} is too low (1–2 μm). On the other hand the penetration depth must not be too high, or else $L_\mathrm{p} \gg \alpha^{-1}$ is not satisfied. The figure also shows that the penetration depth increases strongly as the temperature is decreased, which can be a problem.

The minority carrier diffusion length (for holes) is given by $L_\mathrm{p} = \sqrt{D_\mathrm{p}\tau_{\mathrm{p}0}}$, where D_p is the minority carrier hole diffusion coefficient and τ_{p0} is the lifetime of minority carrier holes. The hole diffusion coefficient is related to the hole mobility, μ_p, by the Einstein relation $D_\mathrm{p} = \mu_\mathrm{p} k_\mathrm{B} T/e$.

From [Gaubas 2006] the minority carrier lifetime in CZ-Ge at a doping level of 2×10^{15} $\mathrm{cm^{-3}}$ (for both n-type and p-type) is approximately 5 μs. Mobilities at this doping level are [Sze 1981] $\mu_\mathrm{p} \approx 1700$ $\mathrm{cm^2/(V{\cdot}s)}$ and $\mu_\mathrm{p} \approx 3350$ $\mathrm{cm^2/(V{\cdot}s)}$. Using the Einstein relation then results in the RT values $L_\mathrm{p} \approx 150$ μm and $L_\mathrm{n} \approx 210$ μm.

It just so happens that a wavelength of 1550 nm (corresponding to 0.8 eV) is used for some fiber communications applications, and a commercial laser diode operating at this wavelength is available from Mitsubishi. This laser diode is labeled ML925B45F, has a very fast rise and fall time (<1 ns), a high

[12] The depth at which the light intensity has been reduced to $1/\mathrm{e} \approx 37\%$ of its initial value.
[13] The minority carrier diffusion length is an experimentally determined parameter.

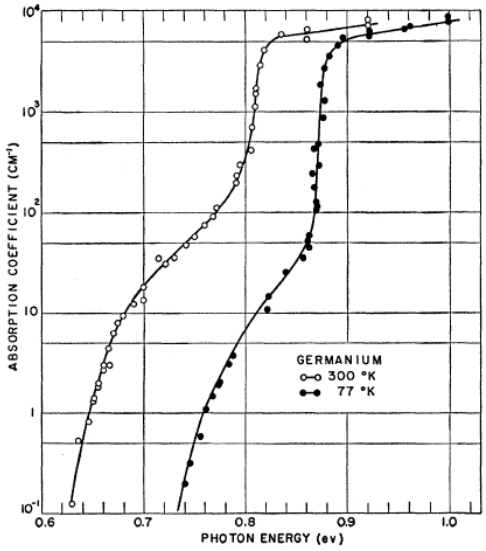

Figure 2.7: The absorption coefficient, α, of Ge at 77 K and 300 K [Dash 1955].

maximum power output (6 mW) and can be purchased from Thorlabs[14]; this makes it perfect for optical MCTS in Ge. Note that these laser diodes are extremely sensitive so care must be taken to protect them from overload.

Evaluating the RT penetration depth from 0.8 eV light using figure 2.7 gives $\alpha^{-1} \approx 20$ μm, which means that (2.41) can be satisfied; x_r at V_r =-10 V is less than 10 μm for all diodes used here. However at 77 K $\alpha^{-1} \approx 1300$ μm, so Ge barely absorbs the light and MCTS will fail[15] at some temperature between 77 K and 300 K. To remedy this a higher photon energy is needed, about 0.87 eV (wavelength 1430 μm) would be optimal to cover the broadest range of temperature. The existence of such an additional high power LED or laser diode was not investigated. The ML925B45F diodes have been used to conduct MCTS on n^+p diodes, however no new peaks (cf section 4.3.2), other than what was seen by forward bias MCTS, appeared.

In the case of Schottky barrier diodes the metal layer on top has to be very thin to let the light through. In the case of Au the penetration depth of 1550 nm light at RT is on the order of 100 nm [Pells 1969], which the thickness

[14] `http://www.thorlabs.com/thorProduct.cfm?partNumber=ML925B45F`

[15] Although the mobility increases with decreasing temperature, this is not enough to counter the decrease of the absorption.

of the Au layer then has to be substantially below. This is entirely doable, and for these optical purposes we routinely deposit 10–20 nm Au on Ge to form a Schottky diode. However the metal film is substantially more fragile than the normal thicker films; so care has to. be taken when bonding the diodes.

2.1.4.5 Defect identification

DLTS suffers from one big flaw namely that very little structural information is contained in the transient. This complicates the identification of the defects responsible for the electronic levels. The information that *can* be deduced is related to the charge of the defect. When there is a Coulomb attraction between the majority carrier and the defect (using a classical picture) the barrier a carrier has to cross to get emitted is lowered by the electric field inside the SCR. This then leads to $e_{\mathrm{n/p}}$ being enhanced by the electric field.

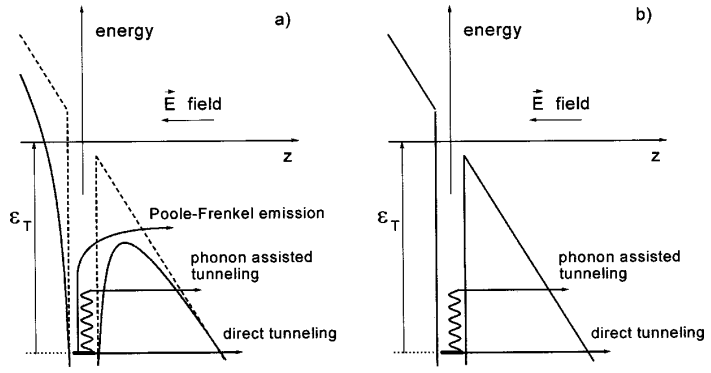

Figure 2.8: The modification of the defect-carrier interaction potential by an external electric field in the case of a) a charged defect and b) a neutral defect. The figure is from [Ganichev 2000]

Assuming a Coulomb potential between the defect and the carrier, as illustrated in figure 2.8, a simple expression can be derived for the field enhancement. Using a one-dimensional model and denoting the charge of the defect in units of e by Z, the attractive potential is given by:

$$U(x) = -\frac{1}{4\pi\epsilon}\frac{e^2 Z}{|x|}. \tag{2.42}$$

Given the small dimensions of a point defect (~1 nm) compared to typical SCR dimensions (micrometers), the variation of the electric field over the defect can

be neglected and the contribution to the potential from the external electric field, $\mathcal{E}$ is[16]:

$$U_f(x) = -e\mathcal{E}x. \tag{2.43}$$

Adding this contribution and finding the local maximum for $x > 0$ gives:

$$\begin{aligned} U_{tot}(x) &= -\left(\frac{1}{4\pi\epsilon}\frac{e^2 Z}{|x|} + e\mathcal{E}x\right) \\ \left.\frac{\partial U_{tot}(x)}{\partial x}\right|_{x>0} &= 0 \Rightarrow \frac{1}{4\pi\epsilon}\frac{e^2 Z}{x_0^2} = e\mathcal{E} \Rightarrow x_0 = \sqrt{\frac{Ze}{\mathcal{E}4\pi\epsilon}} \\ \Delta E_t &= -U_{tot}(x_0) = e\mathcal{E}x_0 + \frac{1}{4\pi\epsilon}\frac{e^2 Z}{x_0} = \sqrt{\frac{\mathcal{E}Ze^3}{\pi\epsilon}}. \end{aligned} \tag{2.44}$$

This lowering of the barrier is known as the Poole-Frenkel effect and was first noted by Frenkel [Frenkel 1938]. Some authors add a factor of a half in the lowering of the barrier related to an image charge interaction [Hartke 1968]. The end result for the variation of e with $\mathcal{E}$ is then:

$$e(\mathcal{E}) = e(0) \cdot \exp\left(-\frac{\Delta E_t}{kT}\right) = e(0) \cdot \exp\left(-\frac{\sqrt{\mathcal{E}}}{kT}\sqrt{\frac{Ze^3}{\pi\epsilon}}\right). \tag{2.45}$$

The signature of a defect oppositely charged to the majority carriers is thus that $\ln[e(\mathcal{E})]$ is a linear function of $\sqrt{\mathcal{E}}$. Experiments give often though this dependence without having exactly the prefactor to $\sqrt{\mathcal{E}}$ predicted by (2.45). This could be anticipated from the fact that a Coulomb potential between carrier and the defect is an optimistic idealization.

The presence of a field dependence itself is not enough to conclude that the defect has the opposite charge sign of the carrier since phonon-assisted tunneling yields a quadratic dependence on the field for strong fields, even for a neutral defect, so that $\ln\left[e(\mathcal{E})\right]$ is a linear function of $\mathcal{E}^2$ [Ganichev 2000]. It is possible to have the former effect for weaker fields and the latter for stronger fields for the same trap.

A repulsive trap, that is a defect with the same sign of charge as the majority carriers, can be indicated by a very low capture cross-section, such

[16]The direction of the field is of no importance since in this simplified analysis it is implicitly assumed that the attractive potential is symmetric.

as on the order of 10^{-18} cm^2 for the double acceptor of the antimony vacancy pair in n-type Ge which is singly negative before capture of an electron [Fage-Pedersen 2000]. It is also not uncommon that the capture cross section is thermally activated for such a trap. Note though that the reverse statement is not necessarily true.

Apart from this information related to the charge state of the defect it is possible to use hydrostatic pressure along the crystal axes to lift the corresponding degeneracy and thus obtain the point defect symmetry from the splitting of the energy level. This technique has not been used in this work and will thus not be mentioned further. The remaining chances of defect identification then include:

- Comparison with theory
- Annealing studies
- In-situ cold measurements
- Increasing an impurity concentration
- Extrapolation from SiGe

Density Functional Theory (DFT) can potentially predict charge states and corresponding electronic levels of a given defect in a semiconductor. However different studies can give very different results both for the possible charges as well as level positions. Therefore the theoretical predictions are mainly considered as guidelines as to what is possible and what one could expect.

Annealing can reveal if two or more energy levels correspond to the same defect, since the annealing behavior will then be identical. More evidence is needed to make the conclusion firm though, such as an identical concentration of the two DLTS peaks and/or the same depth profile.

Irradiation at low temperature will limit the ability of defects to anneal or migrate. Not only does *in situ* measurements allow the observation of defects that are not stable at RT. With some luck the conversion of these defects to more stable secondary defects can be observed. This additional information can help in the identification of the defects. An example of this is a study using p-type Si where annealing of the vacancy was seen to give rise to the increase of other peaks [Zangenberg 2002].

By implanting an impurity or growing samples with an elevated content of the impurity, defects related to that impurity can be revealed. A prominent example of this is the identification of energy levels of the vacancy-oxygen pair in Ge (cf section 4.3.3).

A much larger number of defects have been identified in Si than in Ge. This can be exploited in the attempt to predict energy levels of defects in Ge. There are a number of studies following defect parameters in $Si_{1-x}Ge_x$ starting at pure Si and moving towards Ge by increasing x. They however do not go further than about $x = 50\%$, so the information has to be extrapolated to pure Ge. In chapter 4 this is discussed for the different defect studies in $Si_{1-x}Ge_x$.

2.2 Atomic diffusion

Atomic diffusion is the process by which atoms, native as well as foreign, move in a solid. In the case of a crystalline solid (as is the case for the Ge studied in this work) the microscopic mechanism responsible for diffusion is jumping between lattice sites or interstitial sites.

Macroscopically the diffusion can be described by the so called *diffusion equation*. In our case the equations can be simplified to one dimension since samples are produced so that the concentration is only varying along one direction. To have a net change in the concentration profile over time a concentration gradient is required. The resulting diffusional flux of X, J_X is given by

$$J_X = -D_X \frac{\partial C_X}{\partial x}. \tag{2.46}$$

where x is the spatial coordinate, $C_X(x)$ the concentration profile of X and D_X the *diffusion coefficient* or *diffusivity* of X. The conservation of X can be expressed in the form of a local continuity equation,

$$\frac{\mathrm{d}C_X}{\mathrm{d}t} = -\frac{\partial J_x}{\partial x}. \tag{2.47}$$

What this equation says is that the local change in the amount of X as a function of time as described by the concentration must be balanced by a corresponding variation in the flux as a function of distance. Combining these two

equations leads to the diffusion equation also known as *Fick's second law*:

$$\frac{\mathrm{d}C_\mathrm{X}}{\mathrm{d}t} = \frac{\partial}{\partial x}\left(D_\mathrm{X}\frac{\partial C_\mathrm{X}}{\partial x}\right). \tag{2.48}$$

In the case that D_X does not depend on concentration, and thus on distance, the diffusion equation takes the simple form:

$$\boxed{\frac{\mathrm{d}C_\mathrm{X}}{\mathrm{d}t} = D_\mathrm{X}\frac{\partial^2 C_\mathrm{X}}{\partial^2 x}}. \tag{2.49}$$

This is usually the case when the impurity in question (X) is substitutional and isovalent, thus not affecting the carrier concentration, or the concentration is below the intrinsic carrier concentration, n_i, at the temperature in question.

It is instructive to write down the integral equivalent of the differential equation (2.49):

$$C(x,t) = \int_{-\infty}^{\infty} G(x,x',t)\cdot C(x',0)\mathrm{d}x' \tag{2.50}$$

where G is given by

$$G(x,x',t) = \frac{1}{2\sqrt{\pi D_\mathrm{X} t}}\cdot\exp\left(-\frac{(x-x')^2}{4D_\mathrm{X}t}\right). \tag{2.51}$$

The validity of G can be checked directly by inserting (2.50) into (2.49). From (2.51) it is evident that the effect of diffusion is Gaussian broadening of the concentration profile. In particular a Gaussian impurity profile with width[17] $\sigma = \sigma_0$ will become broadened to a Gaussian profile with $\sigma^2 = \sigma_0^2 + 2D_\mathrm{X}t$. This is simply the general result of the convolution of two Gaussian functions. On this basis it is reasonable to term the distance $l_\mathrm{D} = \sqrt{2D_\mathrm{X}t}$ the *diffusion length*. This length is useful in estimating proper parameters for an annealing experiment given that D_X can be estimated.

The microscopic nature of the diffusion is contained in D_X. As the individual atomic jumps involve overcoming a potential barrier the process is thermally activated and D_X can normally be assumed to follow an Arrhenius law:

$$D_\mathrm{X}(T) = D_{0,\mathrm{X}}\cdot\exp\left(-\frac{Q_\mathrm{X}}{\mathrm{k_B}T}\right). \tag{2.52}$$

[17] The standard deviation in the case of a normal probability distribution.

In our case we focus entirely on impurities that are predominantly dissolved on substitutional sites. Since concerted exchange of a substitutional atom directly with a neighboring lattice atom is not believed to play an important part [Bracht 2007], interaction with point defects is required to allow the atoms to diffuse. The major reactions describing this are:

$$X_s + V \rightleftharpoons XV \qquad \text{(Vacancy mechanism)} \tag{2.53}$$

$$X_s + I \rightleftharpoons X_i \qquad \text{(Kick-out mechanism)} \tag{2.54}$$

$$X_s + I \rightleftharpoons XI \qquad \text{(Interstitialcy mechanism)} \tag{2.55}$$

$$X_s \rightleftharpoons V + X_i \qquad \text{(Dissociative mechanism).} \tag{2.56}$$

If a strong enough attractive potential exists at a third nearest neighbor distance[18] in the impurity-vacancy pair (XV) appearing in reaction (2.53) the pair can diffuse as a unit. This likely represents an enhancement in diffusion rate compared to the case where the pair has to fully dissociate in order to enable net diffusion. Reaction (2.54) represents an interstitial mechanism where the foreign atom diffuses through interstitial sites. The third reaction (2.55) applies to the case of diffusion via an impurity-interstitial pair also known as an interstitialcy. The final reaction is mainly relevant for metal impurities.

The charge states have been omitted in the reactions above but the existence of different charge states of the point defects are actually important for diffusion. The charge state affects the probability of the reactions above and more importantly the concentration of the defect in the various charge states

[18]To give a net diffusion in the diamond lattice, the vacancy in the XV pair has to move to a third nearest neighbor distance, in order to shift to a different nearest neighbor position.

is affected by the Fermi level [Fahey 1989]:

$$\frac{C_{Z^{=}}}{C_{Z^{-}}} = \frac{\theta_{Z^{=}}}{\theta_{Z^{-}}} \cdot \exp\left(-\frac{E_{Z^{=/-}} - E_F}{k_B T}\right) \tag{2.57}$$

$$\frac{C_{Z^{-}}}{C_{Z^{0}}} = \frac{\theta_{Z^{-}}}{\theta_{Z^{0}}} \cdot \exp\left(-\frac{E_{Z^{-/0}} - E_F}{k_B T}\right) \tag{2.58}$$

$$\frac{C_{Z^{0}}}{C_S} = \theta_{Z^{0}} \cdot \exp\left(-G^f_{X^0}/k_B T\right) \tag{2.59}$$

$$\frac{C_{Z^{+}}}{C_{Z^{0}}} = \frac{\theta_{Z^{+}}}{\theta_{Z^{0}}} \cdot \exp\left(-\frac{E_F - E_{Z^{0/+}}}{k_B T}\right) \tag{2.60}$$

$$\frac{C_{Z^{++}}}{C_{Z^{+}}} = \frac{\theta_{Z^{++}}}{\theta_{Z^{+}}} \cdot \exp\left(-\frac{E_F - E_{Z^{+/++}}}{k_B T}\right) \tag{2.61}$$

where Z represents one of the point defects V or I, C_S the density of available sites, θ are degeneracy factors and $G^f_{Z^0}$ the Gibbs free energy of formation for the neutral point defect. The effect of the Fermi level can be summarized, based on the above equations, as

$$\frac{C_{Z^{=}}}{C^{i}_{Z^{=}}} = \left(\frac{n}{n_i}\right)^2, \quad \frac{C_{Z^{-}}}{C^{i}_{Z^{-}}} = \frac{n}{n_i}, \quad C_{Z^{0}} = C^{i}_{Z^{0}}, \quad \frac{C_{Z^{+}}}{C^{i}_{Z^{+}}} = \frac{n_i}{n}, \quad \frac{C_{Z^{++}}}{C^{i}_{Z^{++}}} = \left(\frac{n_i}{n}\right)^2. \tag{2.62}$$

From this it is clear that charged impurity concentrations around n_i or above can increase the concentration of negatively charged point defects (donor impurity) or positively charged points defects (acceptor impurity). The resulting enhanced diffusion under conditions where $C_X > n_i$ is called *extrinsic* and the effective diffusion coefficient, making (2.48) remain valid, will contain relevant terms from (2.62). In the case of a donor impurity and a single point defect with three relevant charge states (=,- and 0) mediating the diffusion the effective diffusion coefficient can be shown to be [Fahey 1989]:

$$D_{eff} = h \cdot \left[D^{i}_{X^{+}Z^{0}} + D^{i}_{X^{+}Z^{-}} \cdot \left(\frac{n}{n_i}\right) + D^{i}_{X^{+}Z^{=}} \cdot \left(\frac{n}{n_i}\right)^2\right] \tag{2.63}$$

where the three diffusion coefficients on the right hand side are the intrinsic contributions to the diffusion coefficient from the respective defect-impurity pairs and h is an enhancement factor arising due to an internal electric field:

$$h = 1 + \frac{C_{X^{+}}}{2n_i\sqrt{1 + \left(\frac{C_{X^{+}}}{2n_i}\right)^2}}. \tag{2.64}$$

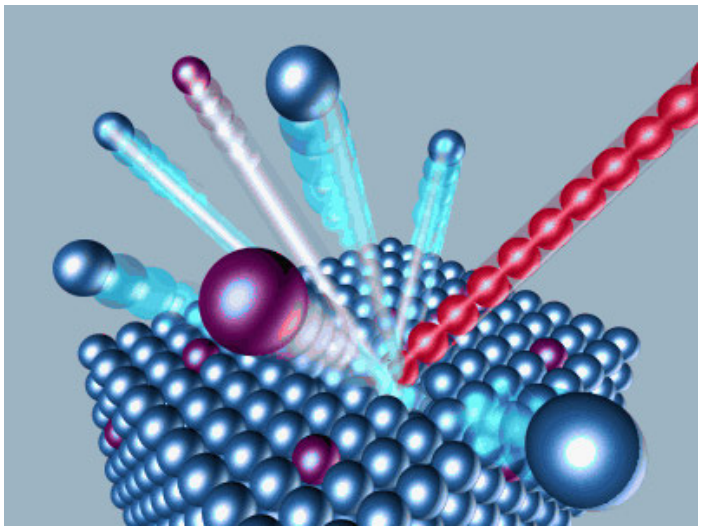

Figure 2.9: An illustration of Secondary Ion Mass Spectrometry. The red atom is the primary ion while the outgoing atoms are secondary ions and neutral atoms. Source: `http://epswww.unm.edu/iom/SIMSgear.html`.

A similar expression holds for acceptor impurities where p should be substituted for n and negative charge states changed to positive charge states.

The carrier concentration follows from the law of mass action, $np = n_i$ and charge neutrality, $n = p + C_{X^+}$:

$$\frac{n}{n_i} = \frac{C_{X^+}}{2n_i} + \sqrt{1 + \left(\frac{C_{X^+}}{2n_i}\right)^2}. \tag{2.65}$$

2.2.1 Secondary ion mass spectrometry (SIMS)

In order to track the evolution of the concentration profile as governed by (2.48) a technique for depth profiling the impurity in question is needed. In this work secondary mass ion spectrometry (SIMS) is used for that purpose. The basic principle of SIMS is to use an ion gun (oxygen and cesium are commonly used primary ions) for sputtering a crater in the sample as illustrated by figure 2.9. Using a high voltage potential and electrostatic lenses the secondary ions leaving the sample, as a result of the sputtering and extraction potential, are extracted and directed into a mass spectrometer. Thus a signal from certain mass ranges can be formed as a function of time. In order to con-

vert the time scale to a depth scale the final crater depth is measured. Assuming a constant sputter yield (this is usually checked by measuring the primary ion current before and after the measurement) the conversion is straightforward. As long as we are working in the dilute limit where the concentration of the impurity is low enough so as to not effect the sputter yield the measured intensity corresponding to a particular ion can be described by

$$I_{\mathrm{Y}} = C_{\mathrm{X}} \cdot \frac{I_{\mathrm{M}}}{\mathrm{RSF}_{\mathrm{M,Y}}} \Rightarrow C_{\mathrm{X}}\Big(x(t)\Big) = \mathrm{RSF}_{\mathrm{M,Y}} \cdot \frac{I_{\mathrm{Y}}(t)}{I_{\mathrm{M}}(t)} \tag{2.66}$$

where Y is an isotope of the impurity in question, X or a molecule involving an isotope of X and an isotope of the matrix element, M. I is the detection rate of the mass spectrometer of the mass in question. Choices involving the primary ion are also possible, but in that case (2.66) might not hold. The optimal choice of Y depends on the actual impurity and possible other impurities present. In particular mass interferences can force the use of other marker molecules. The constant of proportionality, RSF is called the relative sensitivity factor and depends on the matrix, M and the chosen Y as well as the settings of the SIMS instrument being used. Thus the RSF should be determined when a measuring session is stated with a given set of parameters. The way to determine the RSF is by having a reference sample with either a constant known concentration (grown by MBE and determined by RBS for example) of the impurity or a known implanted dose of the impurity. In the former case the RSF can be read off directly by comparing with (2.66). The latter case requires a little more calculation. Letting S_{X} denote the implanted dose of X, by summing the second expression in (2.66) with i being the index of the data points from the concentration profile and Δ the distance between the points, we get:

$$S_{\mathrm{X}} = \sum_i \Delta \cdot C_{\mathrm{X}}(x_i) = \Delta \cdot \mathrm{RSF}_{\mathrm{M,Y}} \sum_i \frac{I_{\mathrm{Y}}(t_i)}{I_{\mathrm{M}}(t_i)} \Rightarrow$$

$$\mathrm{RSF}_{\mathrm{M,Y}} = \frac{S_{\mathrm{X}}}{\Delta \sum_i \frac{I_{\mathrm{Y}}(t_i)}{I_{\mathrm{M}}(t_i)}}. \tag{2.67}$$

Examples of both types of calibration samples are given in chapter 5.

2.2.2 Simulation of annealing

In order to study the diffusion we use 1-dimensional structures, in the sense that the impurity concentration does not vary substantially in the direction

parallel to the surface. One dimension is enough since for samples grown by Molecular Beam Epitaxy (MBE, as described in the next chapter), the impurity concentration only varies as a function of the depth from the surface of the semiconductor. The concentration profile can thus be measured by SIMS. At RT the diffusion is extremely slow so elevated temperatures are used to make the atoms diffuse.

A heat treatment or *annealing* consists of keeping a piece of as-grown sample at an elevated temperature for a predetermined time. The furnace is preheated to the wanted temperature before insertion and upon extraction the sample is extracted quickly out of the hot region of the furnace. Annealing times are chosen long enough that it can be assumed that the ramp up and down in temperature do not contribute significantly to the diffusion.

In order to extract the diffusion coefficient, D_X, the diffusion must be simulated according to (2.48). The input to the simulation is a depth profile, measured by SIMS, of the as-grown sample and D_X is varied until the simulation fits the measured profile after diffusion. The result, assuming that the simulation gives good agreement with the measured profile, is then $D_X(T)$.

By repeating the experiment at several temperatures (adjusting the annealing time to keep the broadening at a reasonable value) an Arrhenius plot of $\ln\left[D_X(T)\right]$ versus $1/T$ can then be constructed and a linear fit yields $D_{0,X}$ and Q_X according to (2.52). The simulation itself is based on approximating (2.49) to finite but small steps in time and space:

$$\begin{aligned}
&\frac{C_X(x,t+\tau)-C_X(x,t)}{\tau} \\
&\approx D_X\frac{\partial}{\partial x}\left(\frac{C_X(x+\Delta/2,t)-C_X(x-\Delta/2,t)}{\Delta}\right) \\
&\approx D_X\left(\frac{C_X(x+\Delta,t)-C_X(x,t)}{\Delta^2}-\frac{C_X(x,t)-C_X(x-\Delta,t)}{\Delta^2}\right) \\
&= \frac{D_X}{\Delta^2}\Big(C_X(x+\Delta,t)+C_X(x-\Delta,t)-2C_X(x,t)\Big)
\end{aligned}$$

where Δ is the spacing between data points in the concentration profile and τ is the time step taken in the simulation. Rewriting the above finally leads to

$$C_X(x,t+\tau) = C_X(x,t) + \frac{\tau\cdot D_X}{\Delta^2}\Big(C_X(x+\Delta,t)+C_X(x-\Delta,t)-2\cdot C_X(x,t)\Big). \quad (2.68)$$

This result allows easy simulation, for example using MATLAB, where the task can be readily formulated using matrices. Special care has to be taken about the first and last point of the profile since (2.68) is not the same there. In particular the 3rd term does not apply for the first point while the 2nd term does not apply for the last. This however is pretty apparent when using matrices since there are no entries for adding those terms.

The last term has to be modified at the boundaries as well since it represents atoms lost to neighboring sites. In the case of a fully impenetrable boundary the 2 would become a one. In general however if there is a certain amount of loss to for example evaporation or into a capping layer the 2 would be replaced by $1 + \delta$ with δ representing the amount of loss. In the ideal situation when using MBE grown samples a sufficient buffer is added on top of the impurity profile so that the surface does not come into play. But there are situations when it becomes necessary to take this into account (see chapter 5).

The matrix version of (2.68) is:

$$\begin{pmatrix} C_1(t+\tau) \\ C_2(t+\tau) \\ \vdots \\ C_{N-1}(t+\tau) \\ C_N(t+\tau) \end{pmatrix} = \left(\mathbf{I} + \frac{\tau D_X}{\Delta^2} \cdot \begin{bmatrix} -(1+\delta_1) & 1 & 0 & \dots & 0 \\ 1 & -2 & 1 & \dots & 0 \\ \vdots & & \ddots & & \vdots \\ 0 & \dots & 1 & -2 & 1 \\ 0 & \dots & 0 & 1 & -(1+\delta_2) \end{bmatrix} \right) \cdot \begin{pmatrix} C_1(t) \\ C_2(t) \\ \vdots \\ C_{N-1}(t) \\ C_N(t) \end{pmatrix} \tag{2.69}$$

where $(C_1(t), C_2(t), \dots, C_N(t))$ is the concentration profile data points at $(x_0, x_0 + \Delta, \dots, x_0 + (N-1) \cdot \Delta)$ at time t, $\mathbf{I}$ is the identity matrix and $0 \leq \delta_1, \delta_2 \leq 1$ takes into account partially absorbing boundaries. Appendix A documents the MATLAB code written with the purpose of simulating diffusion.

In the event that the simplification to a diffusion coefficient independent of position does not hold, because of the impurity concentration being higher than n_i[19], the derivatives leading to (2.68) should be taken on $D_{\text{eff}} \cdot C(x,t)$ instead of $C(x,t)$; with D_{eff} given by (2.63). Therefore this can be taken into account by modifying (2.69) from $\mathbf{C}(t+\tau) = (\mathbf{I} + \tau D/\Delta^2 \mathbf{M})\mathbf{C}(t)$ to

$$\mathbf{C}(t+\tau) = \left(\mathbf{I} + \frac{\tau}{\Delta^2} \mathbf{M} \cdot \mathbf{D} \right) \cdot \mathbf{C}(t) \tag{2.70}$$

[19] Assuming the material is intrinsic apart from the impurity diffusing.

Where D is the diagonal matrix:

$$\mathbf{D} = \begin{bmatrix} D_{\text{eff}}\big(C_1(t)\big) & & \cdots & & 0 \\ & D_{\text{eff}}\big(C_2(t)\big) & & & \\ \vdots & & \ddots & & \vdots \\ & & & D_{\text{eff}}\big(C_{N-1}(t)\big) & \\ 0 & & \cdots & & D_{\text{eff}}\big(C_N(t)\big) \end{bmatrix} \tag{2.71}$$

with D_{eff} being given by an appropriate version of equation (2.63). This makes the simulation of diffusion much heavier computationally as **D** has to be recalculated for every time step. Nevertheless it it simple to allow for the description of extrinsic diffusion in this manner. Even if D_X is independent of C_X, $C_X > n_i$ requires the inclusion of the field effect, making this kind of simulation needed.

CHAPTER 3

Experimental setup

Contents

3.1 Sample growth by molecular beam epitaxy (MBE)

Molecular beam epitaxy (MBE) is a crystal growth technique, primarily for growing single crystal thin films. The growth takes place under ultra high vacuum (UHV, in our case $\sim 4 \times 10^{-10}$ mbar), to keep the sample clean, and is based on an existing single crystal substrate. Atoms or molecules of the elements to be part of the film are evaporated, thermally (with an effusion cell) or by electron gun evaporation, onto the rotating substrate.

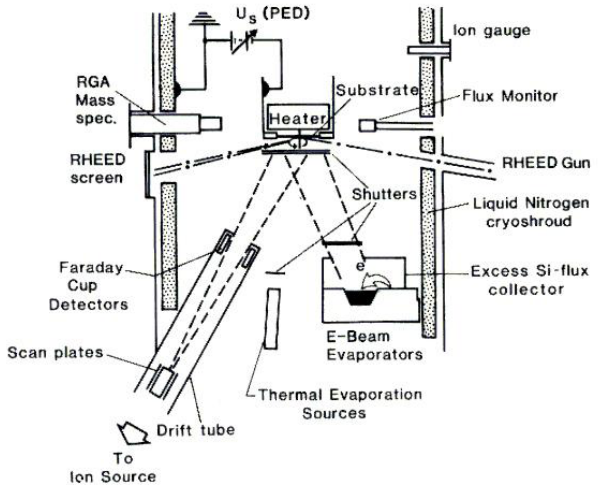

Figure 3.1: The layout of a vacuum chamber for Molecular Beam Epitaxy (MBE) thin film growth.

The deposition rate is kept low enough (less than about 1 μm/hour), and the substrate temperature is elecated (150–400°C for Ge), so that the incoming atoms have time to align themselves with the underlying crystal. The incorporation of dopants is enabled by opening a shutter in front of the respective source. How high the concentration of an impurity gets is determined by substrate temperature and the output of the source. Figure 3.1 illustrates the layout of a MBE chamber. The system used at IFA is a VG Semicon MBE product.

3.2 Diode preparation

Regardless of the diode type an ohmic contact can be made by scratching a eutectic indium-gallium (InGa) alloy on the surface of the germanium sample. This is used to make a contact to the back side of the diodes. After applying the InGa alloy the samples are glued on TO5 headers (see figure 3.2) using silver paste. If needed it is also possible to form an alternative ohmic contact to p-type Ge by evaporating aluminum on the surface. This however was only used to test if the properties of the diodes were any different with this kind of contact; no significant improvement was seen, so InGa was used.

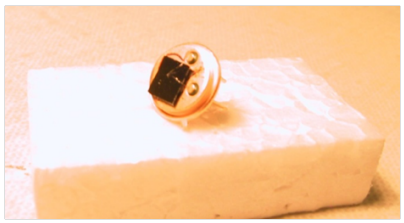

Figure 3.2: A Ge diode mounted on a TO5 header.

The front side contact is made by ultrasonic bonding of a thin aluminum wire to the front using a Bonding Tool, Model 4123 made by Kulick & Soffa industries inc. The other end of the wire is fixed to one of the two pins on the TO5 header again by ultrasonic bonding. In cases where the top side of the diode is fragile the bonding is instead done manually using a small drop of silver paste at both ends of the wire.

All the diodes used in this work are based on substrates grown by the Czochralski (CZ) process from UMICORE[1]. The n-type substrates are doped with antimony (Sb) and the p-type with gallium (Ga).

3.2.1 n-type

Gold (Au) has a high work function (5.1 eV) compared to the electron affinity of Ge (4.13 eV) meaning that Au on Ge will act as a rectifying Schottky barrier. To prepare the n-type Schottky diodes used in this work, Au was evaporated onto the polished side of Ge through a mask. This mask produces three different sizes of circular patches of Au with the area ranging from 0.25 mm^2 to 1.33 mm^2. One cluster with the three different areas fit on a TO5 header.

3.2.2 p-type

For p-type the situation is more difficult since the work function of the metal has to be lower than the Ge electron affinity to form a Schottky barrier. Indium (In) has a work function (4.12 eV) slightly less than the Ge electron affinity, so it is theoretically possible to produce p-type diodes by depositing In on Ge. In practice this only works for low doping levels, and the diodes suffer from high leakage currents; this might be due to problems with the interface quality.

[1] http://www.umicore.com

We have received a few of this kind of p-type Ge diodes from the *Department of Solid State Sciences, Ghent University*. These diodes are doped with Ga to a concentration of 2×10^{14} cm^2, and In has been evaporated on the polished side of Ge in vacuum.

The limitation on the acceptor concentration can be avoided by producing n^+p structures. The procedure for growing a n^+ layer on top of a Ge wafer was optimized in connection with a Master's thesis by *C. E. Lindberg*. MBE is used for growing this top layer, with a thickness of about 0.8 μm, which consists of 8 sub-layers of increasing Sb concentration, and involves two *in situ* annealing steps after certain sub-layers.

The first annealing step has the highest temperature of the two, at 750 °C for about 10 minutes, leading to substantial diffusion of Sb into the p-type substrate ($l_{D,Sb} \approx 500$ nm). This pushes the pn-junction to about 1.7 μm from the surface, cleverly moving the space charge region away from the interface between CZ-Ge and MBE grown Ge. This is good because the interface is defective and would lead to a poor diode. Also the MBE layer contains impurities such as oxygen and carbon, which although lower in concentration are desirable to avoid in the active region.

Figure 3.3 shows a SIMS depth profile of the resulting n^+p diode structure (again from the mentioned Master's thesis), showing the presence of O, C and Sb in the top layer. A side effect of the diffusion of Sb is that defects involving it can form inside the p-type part of the SCR (cf section 4.3.1).

The diode area has to be reduced to less than about 1 mm^2 to keep the leakage current and capacitance low enough to be optimal. This is achieved by a so called mesa[2]-etch. By hand, spots of ~ 0.4 mm^2 on top of the n^+p structure is covered with melted wax. When the wax has solidified this protects a column of semiconductor from being etched as the etching is preferentially normal to the surface. A 3:1 solution of 65% nitric acid (HNO_3) and 40% hydroflouric acid (HF) is used, and the etch lasts 20–30 seconds. After removing the wax with trichloroethane, the end result is columns, termed mesa-diodes, of n^+p material that limit the junction area to ~ 0.4 mm^2. This procedure is illustrated in figure 3.4.

[2] 'mesa' is Spanish for 'table' and is used to describe rock formations with a flat plateau and steep sides. The structures resulting from this process resemble such a rock formation, thus the name.

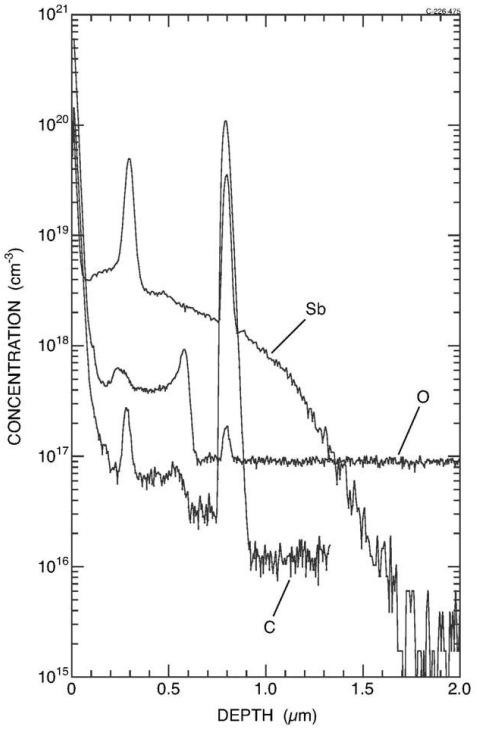

Figure 3.3: SIMS depth profile of the n^+p structure, where the top layer is grown by MBE, showing O, C and Sb concentrations. The MBE grown part if from a depth of 0 to 0.8 μm.

We have Ge mesa diodes available at Ga concentrations of 4×10^{14} cm^3 and 1.8×10^{15} cm^2.

3.3 Sample irradiation

All irradiations in this work were carried out at the 5 MeV Van de Graaf accelerator at the Department of Physics and Astronomy, Aarhus University. As the name indicates this accelerator builds up its acceleration voltage by the Van de Graaf principle. This is illustrated in figure 3.5; a moving belt is transporting charge onto the high-voltage terminal increasing the potential.

The ion source is placed inside the terminal and the emitted particles are accelerated as they pass down the acceleration tube. Our accelerator has been modified to be able to switch to having a negative terminal voltage. This al-

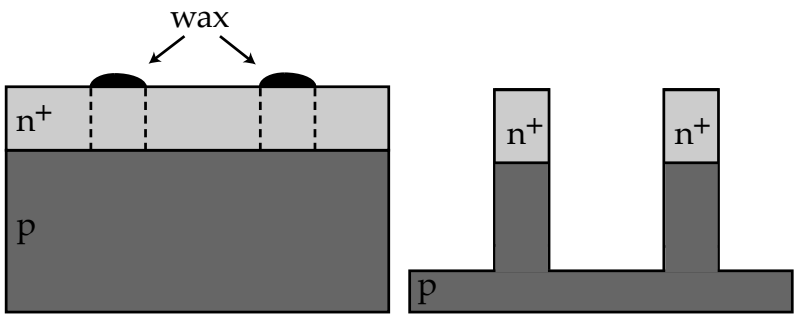

Figure 3.4: Left: Two wax spots on top of the n^+p structure. Right: The mesa-diodes remaining after etching and removal of the wax.

lows the acceleration of negative particles; in this case electrons are the ones of interest. There are additional requirements for successfully irradiating the sample, ~10 m down the beam line, with electrons. Namely more fine control of the beam steering is needed, primarily in the form of a different (low-power) power supply for the switching magnet. Additionally a quadrapole steering magnet is installed and the beam line is shielded with mu-metal (to minimize the influence of outside magnetic fields). The gas in the ion source can be switched been helium (He) and hydrogen (H_2) for extracting respectively He^+ and H^+ or electrons.

The target chamber for irradiating the samples is shown schematically in figure 3.6. The sample holder is made from copper (Cu) and there are two positions for samples mounted on TO5 headers. Four electrical sample connections enable *in situ* measurements. The chamber can be moved horizontally to expose one of the samples or the central pass through to a Faraday-cup to the beam. Additionally a vertically movable copper screen in front of the sample holder will shield everything but the desired spot.

A copper cryo-head, attached to a cooling unit employing liquid helium, is in thermal contact with the sample holder (electrical contact is avoided using mylar foil). This allows the sample to be kept at a constant temperature from RT down to 20–30 K, using the built in heater to stabilize the temperature. Temperature measurements are done at two point; one near the sample to get the sample temperature, and one near the heater to get the best possible heater feedback for the temperature controller.

One feature that is not shown is a brass slit right in front of the samples on

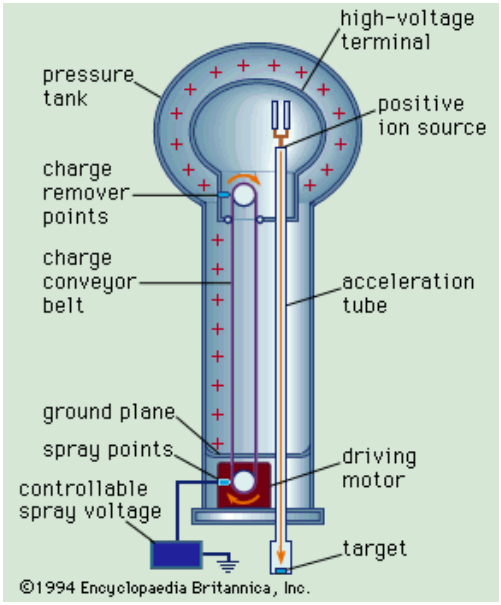

Figure 3.5: Illustration of the general principle of a Van de Graaf accelerator from Encyclopaedia Britannica.

the sample holder. This slit is at the same temperature as the sample holder and thus the sample, and can be moved from the outside. The reason for having this is that black body radiation from the chamber wall (which are at RT) will disturb the DLTS measurements at low temperature [Nielsen 1996]. After irradiation of the sample the slit is therefore moved in front of the sample.

3.4 DLTS setups

3.4.1 SEMILAB equipments

The Hungarian company Semilab has developed integrated DLTS solutions that contain all the electronics necessary to conduct DLTS measurements. A PC running the included software in DOS interfaces with the equipment to control the measurements. Both the newest version, the Semilab DLS-83D (shown in figure 3.7, as well as the previous version, the less compact Semilab DLS-82E, has been used in this work. The older version has an unsurpassed low level of noise in the built in capacitance meter, making it superior for low

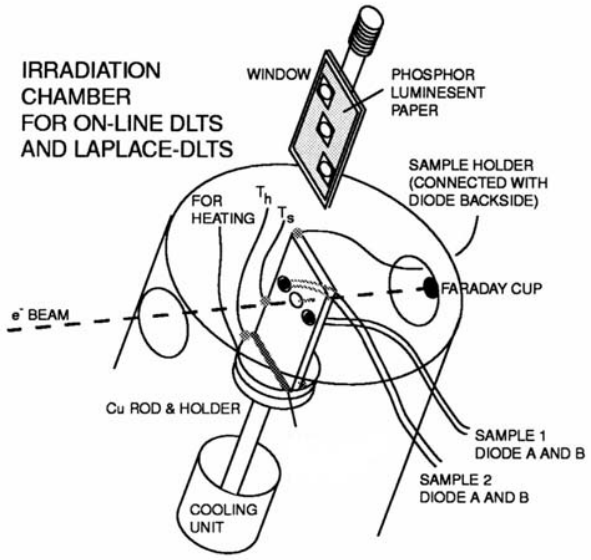

Figure 3.6: The target chamber using for irradiating samples at the Van de Graaf accelerator.

signal measurements.

Figure 3.7: The commercial Semilab DLS-83D DLTS equipment.

3.4.2 PC-based custom system

A custom DLTS system requires first of all electronics to apply pulses to the sample, measure the sample capacitance, record the capacitance as a function of time and finally a temperature controller. Apart from this there are a host of

optional components that could be added, such as for example an I-V meter for measuring current-voltage characteristics.

Finally a piece of software is required to control the pulse application, data acquisition and so on, which could relatively easy be written in for example LabVIEW. However this is time consuming and, as mentioned previously, a lot of work has been put into developing a full-featured DLTS and Laplace-DLTS application by L. Dobaczewski and collaborators [Dobaczewski 2009].

In conjunction with the Laplace-DLTS software, an ISA-bus PC add on card for applying pulses and measuring a capacitance-meter signal, was developed at the University of Manchester, known as the UMIST-card. However, recent years it has become possible to purchase a suitable commercial digital acquisition card (DAQ) for the PC, such as the national instruments NI-6251 (costing less than 750 €). This PCI-bus add on card is what we use in our setup, and it has two analog outputs (±10 V maximum) suitable for applying voltage pulses.

Figure 3.8: The Boonton 7200 capacitance meter.

Boonton Electronics has a capacitance meter in their product line that is ideal for DLTS measurements. Figure 3.8 show the latest version, Boonton 7200, while we use the previous version, Boonton 72B. This meter has two terminals for the sample as well as two terminals for a reference capacitance. What is measured is the capacitance difference between the sample and the reference. This allows the measurement of capacitance transients, even when the sample capacitance is out of the meter range (normally ±30 pF[3]). Addi-

[3]Choosing a higher range increases the absolute level of noise significantly.

tionally the capacitance meter has a feed-through input for the application of voltage pulses. The output signal is a DC voltage proportional to the measured capacitance which is then read by an analog input channel on the NI-6251 card.

Figure 3.9: The external pulse generator, Hewlett Packard HP8110A, used to enable reverse biases down to -20 V as well as the application of light pulses for MCTS.

An external pulse generator, the Hewlett Packard[4] HP8110A (shown in figure 3.9, is used to allow pulsing all the way to -20 V or operate a laser diode/LED for optical MCTS. The Laplace DLTS software is able to remote control the HP8110A via a GPIB connection. However the current version (v3.3) of the software does not trigger correctly in this mode, so the pulse generator is instead configured manually. In this operating mode the output pulses from the NI-6251 DAQ card is used for triggering the pulse generator. When working with light pulses an external power supply is used to reverse bias the sample.

3.5 SIMS instruments

The main difference between different variants of SIMS instruments lies in the mass spectrometer, used to analyze the outgoing secondary ions from the sample. The two different variants used here are described below.

3.5.1 Cameca magnetic sector SIMS

The Cameca 4f SIMS instrument uses a magnetic sector mass spectrometer to pick out the mass for analysis. This means that only one mass signal can be

[4]Now known as Agilent Technologies.

analyzed at a given time. However the analysis time can be split between several masses.

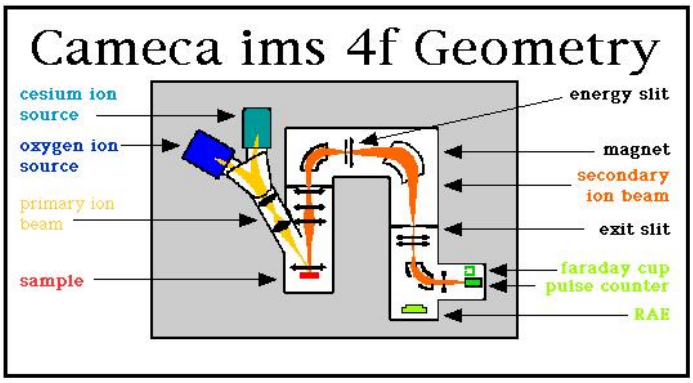

Figure 3.10: A schematic of the geometry of the Cameca 4f SIMS instrument. Borrowed from `http://epswww.unm.edu/iom/SIMSgear.html`.

As primary ion O_2^+ is used for observing elements that primarily form negative ions (typically the case for acceptors), while Cs^+ is used for positive ions (typically the case for donors). Figure 3.10 shows the layout of the instrument.

Measurements with a Cameca 4f equipment were carried out at the KTH royal institute of technology, Sweden, with the precious help of Margareta Linnarsson.

3.5.2 IonToF Time of Flight SIMS

As implied in the name, the IonToF[5] SIMS is based on time of flight (ToF) mass analysis, which implies that all collected secondary ions pass through the analyzer. This has the important feature that the whole mass spectrum can be recorded as a function of depth; therefore depth profiles of additional elements can be constructed post-measurement. Also the monitoring of extra elements is not at the expense of statistics, which is the case for "conventional" equipments.

The ToF principle requires pulsed operation of the primary ion gun, since the secondary ions must start out synchronized. Furthermore the sputtering rate, and thus the primary ion current, must be very low in order not to satu-

[5] `http://www.ion-tof.com`

rate the detector. For a magnetic sector instrument this is not the case as the bulk of the ions are rejected.

Bismuth (Bi) ions (in this work only Bi^+) at an energy of 25 keV are employed as primary ions in our IonToF IV system at IFA. For depth profiling, a second more powerful ion gun is needed to sputter material away. This is achieved using Cesium (Cs) sputtering using Cs^+ at an energy of up to 10 keV, interlaced with Bi primary pulses; the default cycle time is 100 μs. The full instrument is illustrated in figure 3.11.

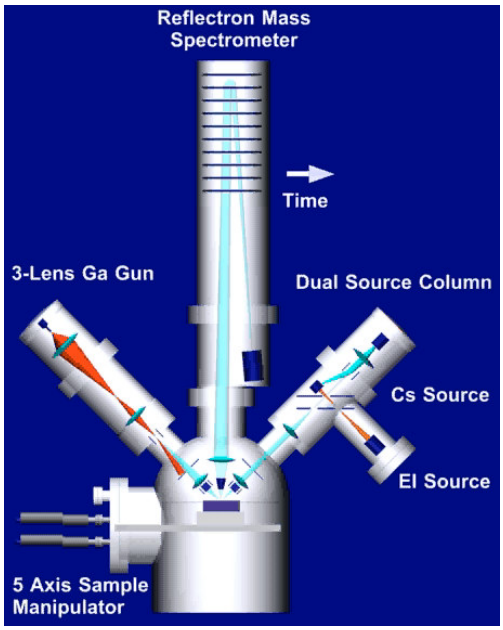

Figure 3.11: The schematic layout of an IonToF SIMS equipment. Left is the primary gun (for our equipment Bi instead of Ga) and right is the Cs sputtering gun while the mass spectrometer is at the top. Source: IonToF SIMS introduction.

The Cs^+ sputtering energy can have a strong impact on secondary ion yield, even though the sputtering is not producing secondary ions directly. This effect is in addition to the sample erosion rate being sensitive to not only the sputtering current, but also the sputtering energy. It is important to realize that the sputtering with Bi^+ at such a high energy, as 25 keV is, in Ge has a tendency to produce di-atomic ions at a higher rate than mono-atomic ions. This means that generally it gives a better sensitivity to detect an impurity, X, through the di-atomic ion ^{74}Ge-X. Unfortunately this is detrimental to the

detection limit.

3.6 Annealing furnaces

It is a poor idea to carry out annealing experiments in atmospheric air, in particular due to the presence of oxygen, but also due to other possible contaminants. Two different strategies are employed to avoid this influence, annealing in a flow of very pure nitrogen or annealing in vacuum.

3.6.1 Flow annealing

The flow furnace used to carry out annealing in a nitrogen flow is shown in figure 3.12. It is built around a resistively heated quartz tube and has a built in temperature controller, stabilizing the temperature at the setpoint. The temperature feedback used to control the heater power comes from a thermocouple in contact with the tube. The nitrogen flow enters on the left end of the furnace, and exits through an exhaust in the load lock seen at the right end.

Figure 3.12: The flow furnace used to anneal Ge samples in a nitrogen flow.

Samples are placed in a quartz boat fixed at the end of a quartz rod, enabling quick insertion and extraction to and from the central hot region. A thermocouple is held inside the tube, positioned right above the sample position, giving an accurate sample temperature reading. As will be demonstrated

in chapter 5, the nitrogen flow is actually not enough to keep Ge from oxidizing.

3.6.2 Vacuum annealing

Our vacuum furnace is a modified version of the "Red Devil" vacuum furnace made by the R. D. Webb Company[6], Inc. This system is based on a resistively heated aluminum oxide tube, pumped by an oil free turbo pump system. However it is a closed system that does not allow sample insertion after vacuum establishment, which makes it very unsuitable for diffusion experiments (which requires a fast ramp up and down in temperature).

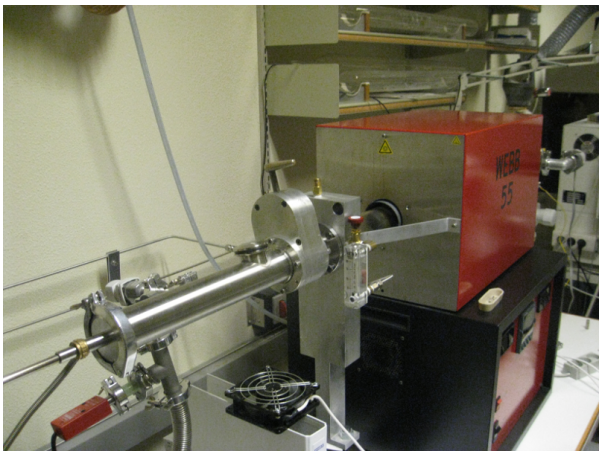

Figure 3.13: The modified "Red Devil" furnace used for annealing of Ge in vacuum.

To remedy this our workshop produced a loading system that has a loadlock which can be sealed from the tube. Quick insertion and extraction to and from the hot zone is therefore possible. In addition we switched to a quartz tube as this is less sensitive to temperature changes and allows visual inspection of the samples. The resulting setup is shown in figure 3.13. With these modifications the base pressure during annealing is $\sim 4 \times 10^{-4}$ mbar.

The insertion/extraction system is made from stainless steel, while the samples are kept in an aluminum oxide boat. Like in the case of the flow furnace, a thermocouple is floating in the tube right above the sample position to read the temperature. However by switching to a quartz tube that did not

[6] http://www.rdwebb.com

have precisely the same length, it was not initially realized that the thermocouple position was no longer exactly in the center.

For the vacuum furnace the thermocouple inside the vacuum is used to control the heater power, since the outside thermocouple in contact with the tube responds too slowly. The incorrect position of the thermocouple meant, that the temperature in the center was much higher than the reading. After exchanging the thermocouple with one of the correct length, the temperature reading was checked by determining the melting point of Ge (938.3°C) and Sb (630.6°C). This was correct within a few degrees, and the extracted calibration allows improvement of the temperature accuracy.

CHAPTER 4

Electronically active defects

Contents

While electronically active defects in Si have been studied intensively Ge has not received the same amount of results. This is in part due to the fact that Ge was almost completely abandoned in favor of Si in the infancy of semiconductor device technology (as mentioned in the introduction).

Also the electron paramagnetic resonance (EPR) technique which has been an important tool in defect studies in Si [Watkins 2000] is difficult for Ge. Isotopically pure ^{74}Ge is needed for EPR due to the many lines from the other

four isotopes in natural Ge. Furthermore a strong inhomogeneous broadening due to the high spin and large nuclear momentum of ^{73}Ge [Khirunenko 1995] means this isotope must be avoided. Due to the similarity of Si with Ge as mentioned earlier, Si will serve as a tool for comparison and a possible hint on what to expect throughout this chapter.

4.1 Elementary point defects

Lattice vacancies and interstitial host atoms, also known as *self-interstitials*, are the most fundamental defects in a crystal. They are present even in a perfect crystal at non-zero temperatures, being generated thermally either in pairs by displacement of a bulk atom or at the surface one by one. One could also imagine forming a correlated pair of an interstitial atom and a vacancy, known as a Frenkel-pair (FP), if the temperature is not high enough for the constituents to annihilate or separate.

Elementary point defects are intimately connected with the diffusion of impurities as described in section 2.2.Studying these defects directly is thus an important addition to diffusion studies.

The equilibrium concentrations at RT of these simple defects are however too low to allow DLTS. Based on the findings for Si [Watkins 2000] and the low concentrations in equilibrium, these simple defects are very mobile at RT. This then means that low temperature irradiations and subsequent *in situ* DLTS measurements are needed to have a chance at observing energy levels of these defects. This section deals with the information that can be extracted about elementary point defects by doing in situ DLTS measurements. We reported the main discoveries from *in situ* measurements on Ge in [Mesli 2008]. The following is a discussion of these results with additional results included.

4.1.1 The vacancy (V)

In Si the lattice vacancy has 5 different charge states, from $V_{Si}^{=}$ to V_{Si}^{++}, and thus four energy levels. However, the two donor levels have an inverted (negative-U) ordering meaning they will act as one energy level with respect to DLTS. Indications of all these charge states have been seen while only two of the energy level positions have been firmly established [Watkins 2000].

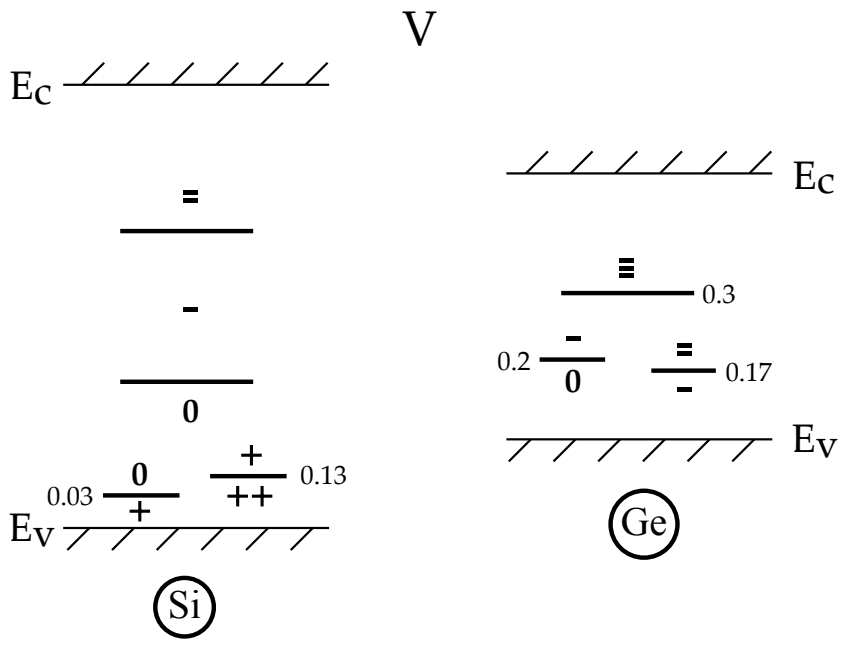

Figure 4.1: Energy levels of the vacancy in Si [Watkins 2000] and the ones predicted by theory (DFT) [Coutinho 2005] in Ge. Numbers shown next to the energy levels are distances to the nearest band in eV.

For Ge DFT calculations have predicted the existence of 4 charge states of the lattice vacancy, from $V^{\equiv}_{Ge}$ to V^{0}_{Ge}, and thus 3 energy levels in the band gap [Coutinho 2005]. The single and double acceptors are predicted close enough to be consistent with a negative-U ordering, but within the uncertainty of the calculations a normal positive-U ordering is possible as well.

The energy levels of the vacancy found in Si and the ones predicted in Ge are shown in figure 4.1. Additionally the calculations were extended to give migration barriers for three of the charge states in Ge giving 0.4, 0.1 and 0.04 for V^{0}_{Ge}, V^{-}_{Ge} and $V^{=}_{Ge}$ respectively [Pinto 2006].

From diffusion experiments with donor concentrations exceeding the intrinsic carrier concentration [Bracht 2006a], the presence of doubly negative vacancies and possibly triply negative vacancies as well [Canneaux 2009] have been indicated. However, it should be noted that those observations would also be consistent with respectively single and double negative donor-vacancy pairs mediating the diffusion.

Trapping of presumably neutral vacancies at negative ^{111}In probes indicated the existence of an acceptor state in the neighborhood of E_v + 0.20 eV [Haesslein 1998]. It appears thus that there is quantitative agreement between these observations and the theoretical predictions. The authors attribute the energy level to a single acceptor, $V^{(-/0)}$ and observed the vacancy becoming mobile in the neutral state at about 200 K.

It is worth commenting that In has a larger covalent radius (0.14 nm) compared to that of Ge (0.12 nm). Therefore one may speculate that an attraction between In^- and V^- could be made possible due to the local strain. In this case a double acceptor may also be an explanation. However, this possibility would require theoretical calculations to substantiate. In the following the observations we have made regarding the vacancy in Ge will be presented.

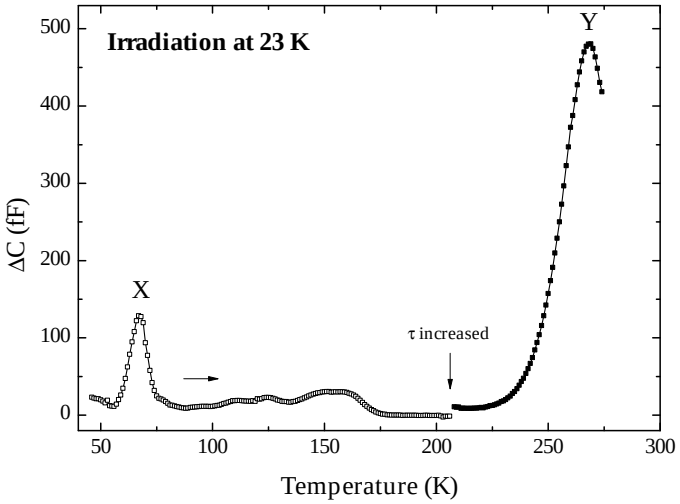

Figure 4.2: DLTS spectrum showing the two dominant peaks, X and Y, introduced by low temperature 2 MeV electron irradiation. The DLTS settings were e_p = 4.1 s^{-1}, V_r = −5 V and V_p = 0 V. Up to a temperature of 210 K a pulse duration of τ = 200 μ was used, and above this temperature it was increased to 17 ms.

Low temperature electron irradiations have given us indirect evidence for the presence of vacancies in n-type Ge. After irradiation with 2 MeV electrons at 20–30 K it is possible to form dips in the donor profile, $N(x)$, by reverse biasing the diode for a few seconds at 90 K. That the dips are formed because of conversion of substitutional Sb into the Sb-vacancy pair (E-center), is clearly

seen by DLTS as a strongly non-uniform depth distribution of SbV. The dips are formed in the bulk (low-field) end of the SCR and consecutive deeper dips can be formed by using more negative biases. Since the electric field is pointing towards the metal-semiconductor interface this is clear evidence that the vacancies are negatively charged in line with both theory and experimental observations mentioned above [Mesli 2008].

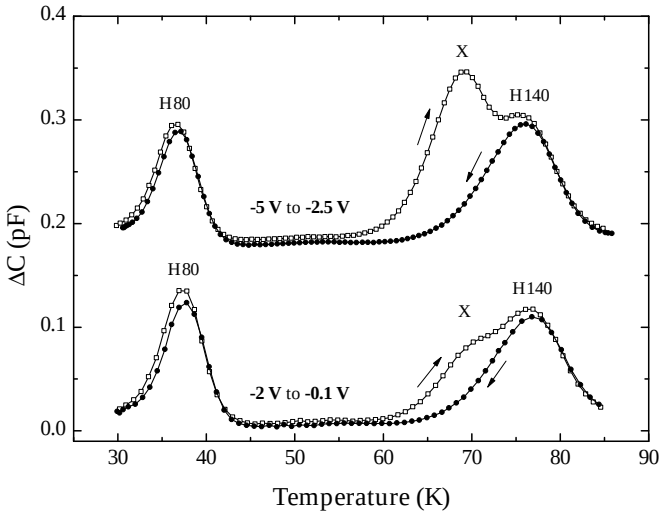

Figure 4.3: DLTS spectra demonstrating the instability of the defect responsible for the X peak inside the SCR. The lower spectra are recorded first and then subsequently the upper spectra. The diode has been previously irradiated and brought to RT leaving the two stable peaks H80 and H140 (cf 4.2.2). This demonstrates that the annealing of X does not appear to affect the defects giving these peaks.

After electron irradiation of n^+p Ge mesa diodes at 20–50 K a clear peak, labeled X, is seen in the DLTS spectrum at low temperature as shown in figure 4.2. It is observed that this peak disappears during the crossing of the peak in the DLTS scan up in temperature such that it is not present, or at least has become very weak, in a subsequent scan down in temperature. This is demonstrated by the lower part of figure 4.3. It therefore appears that the corresponding defect becomes unstable somewhere between 60 and 70 K. With such a low temperature of annealing the defect responsible for this energy level should be expected to be one of the three elementary defects mentioned above.

It turns out that by starting a new DLTS scan up in temperature with a more negative reverse bias V_r, and thus probing a region further from the junction that was previously neutral material, the peak can be seen once more. Again the observation is that the peak is gone on the way down in temperature, as shown in the upper spectra of figure 4.3. We can then conclude that the defect has in fact not become thermally mobile in neutral material at 85 K. There are now two possible contributions to the disappearance of the defect; either the defect becomes mobile due to a change in charge state (it will become more negative inside the SCR at these temperatures due to the hole emission) or the electric field is lowering the migration barrier enough to allow migration very similarly to the way the Poole-Frenkel effect increases the emission rate. In Si the vacancy is seen to show such a charge state dependent stability [Watkins 2000] and in reality this in fact plays the major part here, as the lowering of the migration barrier should be expected to be quite small, on the order of meV. Also the theoretical calculations mentioned above give lower migration barriers the more negative the vacancy is in line with the observations. The barrier lowering however serves to make a preferred direction of migration since many jumps of the defect are required for substantial movement, and the directional preference multiplies up.

If we have a look at (2.38) along with the knowledge that the electric field is pointing towards the neutral p-type region increasing from zero at the SCR boundary to a maximum at the junction, we can in fact deduce the charge sign of the defect. Assuming that the defect is positive inside the SCR would mean that the preferred direction of migration would be towards the p-type neutral region. This then leads to an increase in DLTS signal at the onset of the annealing according to (2.38), since the barrier lowering is stronger the closer to the junction. This does not appear to be the case from the DLTS measurements and also Laplace DLTS measurements do not show any such increasing tendency. We thus conclude that the defect must be negatively charged.

In fact, using high resistivity (HR, [Ga] = 4×10^{14} cm^{-3}) samples and low reverse bias it turned out to be possible to stabilize the defect enough in the low-field region of the SCR to measure the emission rate at higher temperatures by Laplace DLTS. This supports the fact that the field is actually en-

hancing the migration. In addition this also enabled the measurement of the emission rate as a function of varying reverse bias and thus electric field. It should be noted that using the average electrical field for the field-dependence is a crude approximation since the DLTS signal is not equally sensitive all the way through the SCR again according to (2.38). Furthermore the depth profile of the defect is not uniform due to the electric field. However, it can be used to get a quantitative idea of the field-dependence.

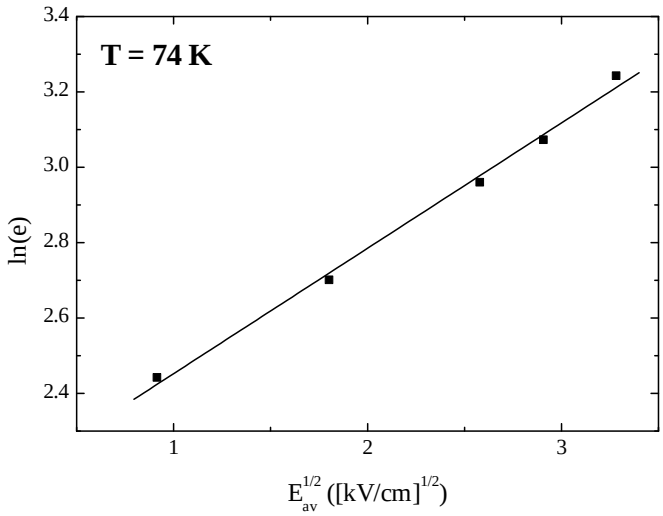

Figure 4.4: Demonstration of the Poole-Frenkel effect of X. The line shown is a straight line fit to the points.

Figure 4.4 shows the logarithm of the emission rate as a function of the square root of the average electric field in the observation area, $x(V_r) \rightarrow x(V_p)$. We see that the field assisted emission is in accord with the Poole-Frenkel effect, thereby confirming that the defect is negatively charged before the capture of a hole. The magnitude of the charge before hole capture can however not be deduced in this quantitative analysis.

Figure 4.5 shows the Arrhenius plot obtained where the activation energy has been corrected for the found Poole-Frenkel-like behavior[1]. In the majority[2] of the SCR there is nothing to pair up with for the defects since, as will

[1] Assuming that the field effect is due to a lowering of the emission barrier as described by (2.45).

[2] As has been noted in the description of these diodes in chapter 3, there is a weak tail of Sb

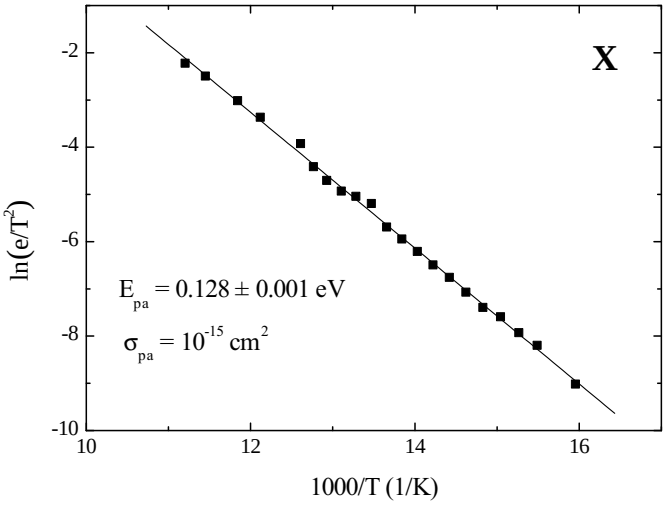

Figure 4.5: An Arrhenius plot of the emission rate of X measured by Laplace DLTS.

be discussed later, the CZ-Ge p-type material has a very low concentration of oxygen and carbon. This means that the only major impurity available for trapping is negatively charged substitutional Ga. Coulomb repulsion makes it very unlikely for the negatively charged defect to pair up with Ga and form a secondary defect inside the SCR. In addition the covalent radii of Ge and Ga are very close, leaving no room for an attraction due to mismatch. This means that we should not expect X to take part in the formation of a substantial amount of secondary defects inside the SCR.

The self-interstitial is seen to be positively charged in n-type Ge as will be discussed below, so we can rule that out as being the defect in question. Ruling out the FP takes a little more thought as it has a double acceptor in the upper half of the band gap, as argued in section 4.1.2, meaning that it could in principle introduce a single acceptor in the lower part of the band gap and could therefore be the defect in question. In this case the annealing of the defect would then correspond to annihilation and/or separation of the partners in the pair. It has been shown experimentally that the pair anneals by annihilation of the constituents in n-type Ge [Emtsev 2006]. However, given the energy levels found for the Ge interstitial this part of the pair is at least

from the top layer.

doubly positive charged while the vacancy part must then be at least doubly negative charged to give an acceptor level. The attraction would thus appear to be much stronger than in n-type where the interstitial part is presumably neutral or singly negative. Therefore the conclusion is that the annealing temperature of the FP in the configuration observed in n-type by DLTS would be substantially lower p-type.

Thus the defect in question cannot be the close FP as the former is stable at least up to 85 K while the FP anneals in n-type around 65 K. In the end there is then only the vacancy left to attribute this energy level to since there is no doubt that one of the three above mentioned elementary defects would be responsible given the quite low temperature that this defect is able to migrate at.

An additional support for this attribution is given by the $SbV^{(-/0)}$ energy level, present due to the Sb tail from the n^+ top-layer, which starts to appear[3] at around 115 K, as shown in [Mesli 2008]. This proves that vacancies have indeed been moving in the SCR, since it is very unlikely to form this defect directly at the given irradiation doses and Sb concentrations.

Studying the annealing of the vacancy is troublesome in this DLTS experiment since the capacitance is recovering, after having increased strongly due to irradiation, all the way up to around 200 K. This means that as the temperature is increased the SCR width increases uncovering more vacancies but also moving the observation region. Getting meaningful annealing results was therefore not possible. In figure 4.6 the mentioned recovery of the capacitance at a fixed reverse bias is shown.

It is not likely that the vacancy is responsible for the bulk of the capacitance increase for several reasons. First of all the vacancy is introduced at the same concentration as the self-interstitial since they are mainly formed in pairs by electron irradiation. This means that in order to increase the negative charge from Ga^- in the SCR the vacancy would have to be at least triply negative charged to compensate the doubly positive self-interstitials[4] and thereby give a net capacitance increase from V and I. Even if this was the case there should then be an enormous amount of self-interstitials available for forming the Ga_i

[3] This requires the application of a slight forward pulse bias to move the observation region closer to the top-layer.

[4] See next section.

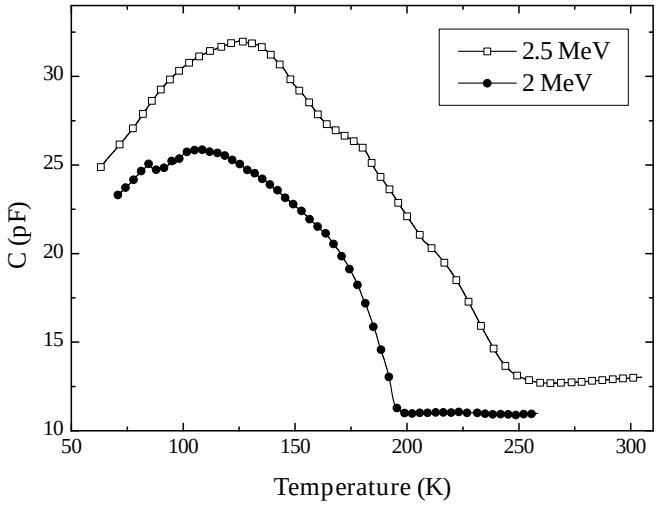

Figure 4.6: Recovery of n^+p junction capacitance after electron irradiation at low temperature with an electron energy of 2.5 MeV (open squares) and 2 MeV (filled circles). The capacitance was measured at -2 V.

defect[5] which however is not seen to be formed at excessive concentrations.

Secondly the vacancy was seen above to be even more unstable in its negative charge state than the 200 K reported for the neutral charge state [Haesslein 1998]. Therefore the contribution to the capacitance from V should not be able to prevail to the higher temperatures demonstrated in figure 4.6. The conclusion is thus that FPs (section 4.1.2) must be responsible since no other elementary defects are left. A distribution of Frenkel-pairs in different configurations (mainly separation distance) would explain the different recovery behavior for 2 MeV and 2.5 MeV electron irradiation.

Although we originally used the capacitance change to argue in favor of a double acceptor energy level [Mesli 2008], the later investigation of the capacitance increase goes against this point, since the vacancy is not the main contributor. We can therefore not make a definite conclusion about a single or double acceptor level. However, a single acceptor level, $V^{(-/0)}$ agrees quite well both with PACS results [Haesslein 1998] and theory [Coutinho 2005]. An additional piece of compelling existence, in favor of a single acceptor level,

[5] See section 4.3.2.

is that diffusion of Ga in Ge is mediated by neutral vacancies (cf 5.3). This requires the presence of such a level All in all we conclude that the vacancy level observed is most likely a single acceptor.

4.1.2 The Frenkel-pair (V-I)

In Si no defect that could firmly be identified as the vacancy-interstitial or Frenkel pair (FP) has been observed. The presence of FPs in Si has though allegedly been observed by X-ray diffraction after irradiation with 1 MeV electrons [Zillgen 1997] but there are no other observations backing this up. In Ge however there is general agreement that an annealing step at 65 K in n-type Ge after low temperature irradiation is due to FP annihilation [Emtsev 2006].

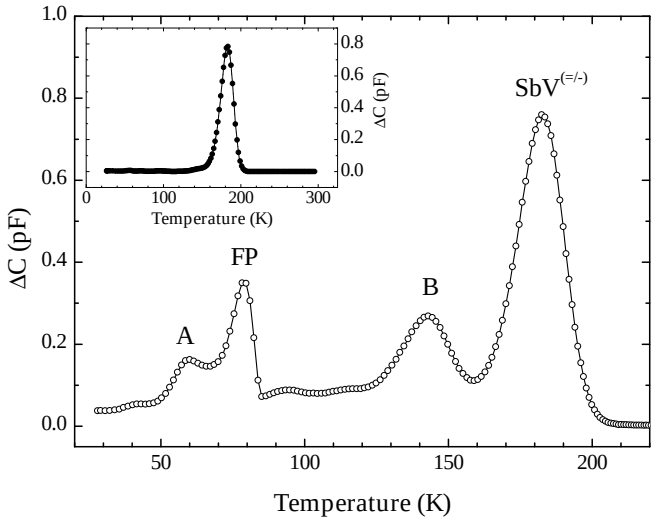

Figure 4.7: DLTS spectrum recorded on a n-type Ge Schottky diode after irradiation with 2 MeV electrons at 27 K to a dose of $1.6{\times}10^{14}$ cm^2. DLTS settings were $e_p = 20\ s^{-1}$, $\tau = 1$ ms, $V_r = -5$ V and $V_p = 0$ V. The inset shows a DLTS spectrum recorded with the same settings after a few minutes at RT.

Remarkably we observe a DLTS peak (labeled FP) in the vicinity of 65 K which disappears as the temperature crosses the peak. Figure 4.7 shows the DLTS spectrum measured after low temperature electron irradiation with the unstable peak labeled FP. A detailed fitting of the asymmetric peak showed that the amplitude was in fact up to seven times higher than what appears

from the DLTS spectrum and thus the defect responsible for the FP peak is very dominant. In addition estimates of the parameters of the corresponding energy level follows from the fit and are $\Delta E_{\mathrm{pa}}(\mathrm{FP}) \approx 0.14$ eV and $\sigma_{\mathrm{pa}} \approx 10^{-15}$ cm^2. Furthermore detailed investigations showed the introduction rate of the FP peak to depend strongly on irradiation energy and temperature [Mesli 2008]. All these observations strongly favor the conclusion that the peak marked FP is indeed due to an energy level of the FP previously concluded to be a double acceptor [Callcott 1967]. As has been previously noted (cf 4.1.1) the E-centers, in this case SbV, are predominantly formed in the low-field end of the SCR where DLTS is most sensitive. This means that the SbV double acceptor peak is larger than the actual uniform vacancy concentration introduced by the irradiation. Thus the ratio between the FP concentration and the vacancy concentration is even higher than the 2-3 times indicated by the correction to the FP amplitude found from fitting.

4.1.3 The self-interstitial (I)

The self-interstitial in Si is elusive in the sense that in p-type Si, even at 4 K, immediately after electron irradiation there is no sign of it by DLTS or EPR. Instead secondary defects such as B_i and C_i, produced by the so called Watkins replacement mechanism [Watkins 2000] are present. By this mechanism interstitial defects are formed by a kick-out reaction induced by mobile self-interstitials. It is believed that this athermal motion of self-interstitials is due to a Bourgoin-Corbett mechanism [Bourgoin 1972] where the alternation between charge states, made possible by the ionization due to the irradiation, equals defect motion through the lattice.

Some theoretical DFT calculations predict the Ge self-interstitial to have the same possible charge states as the Si self-interstitial from zero to doubly positive [Carvalho 2007]. While the two levels are calculated to have a negative-U ordering in Si this is not the case in Ge where the levels $\mathrm{I}^{(0/+)} \sim E_{\mathrm{v}} - 0.08$ eV and $\mathrm{I}^{(+/++)} \sim E_{\mathrm{v}} - 0.24$ eV are found by DFT. In fact the peaks labeled A and B in figure 4.7 fit these parameters exactly so it is likely that $\mathrm{A} \sim \mathrm{I}^{(0/+)}$ and $\mathrm{B} \sim \mathrm{I}^{(+/++)}$. This attribution is further backed up by a very similar annealing behavior of A and B, as well as an apparent field dependence of at least the A peak indicating a donor level [Mesli 2008]. A and B are therefore tentatively

assigned to the donor levels of the Ge self-interstitial. Note that the fact that these peaks are somewhat lower than the SbV double acceptor peak, can be explained by the fact that the latter is higher than the initial uniform vacancy concentration as previously argued. In addition the mentioned DFT calculations found the existence of an inert neutral self-interstitial configuration which could account for part of the produced self-interstitial concentration. The observations are thus not inconsistent with an expected equal concentration of vacancies and self-interstitials immediately after electron irradiation.

4.2 The di-vacancy (V_2)

In Si the vacancy-vacancy pair or di-vacancy defect (V_2) consisting of two empty adjacent lattice sites has 4 possible charge states and thus 3 energy levels in the band gap [Watkins 2000] corresponding to the transitions $V_2^{(0/+)}$, $V_2^{(-/0)}$ and $V_2^{(=/-)}$. The energy levels of these transitions will be shown below when comparing to the levels expected in Ge.

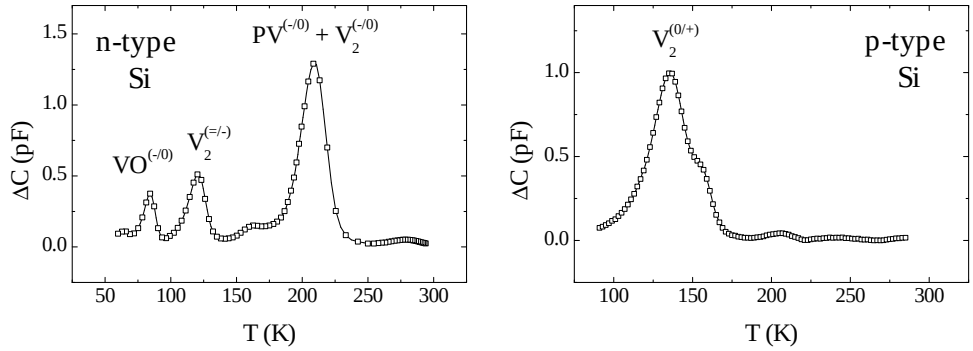

Figure 4.8: DLTS spectra from irradiations of n-type (left) and p-type (right) Si diodes showing the di-vacancy and phosphorus E-center energy levels. Substrates for both types of samples were grown by chemical vapor deposition (CVD, low oxygen and carbon content) and doped with 5×10^{15} cm^{-3} phosphorus (n-type) or 4×10^{15} cm^{-3} boron (p-type). For n-type measurement settings were $e_n = 20$ s^{-1}, $\tau = 1$ ms, $V_r = -9$ V and $V_p = -1$ V while for p-type they were $e_p = 543$ s^{-1}, $\tau = 200$ µs, $V_r = -5$ V and $V_p = 0$ V.

It is an important defect in Si with a resistivity of $\sim 1\Omega$cm or higher, being

typically electrically dominant in p-type and only surpassed by the donor-vacancy pair in n-type Si for oxygen and carbon lean material[6]. Figure 4.8 shows representative DLTS spectra of irradiated Si diodes with a low content of oxygen (the samples are CVD grown).

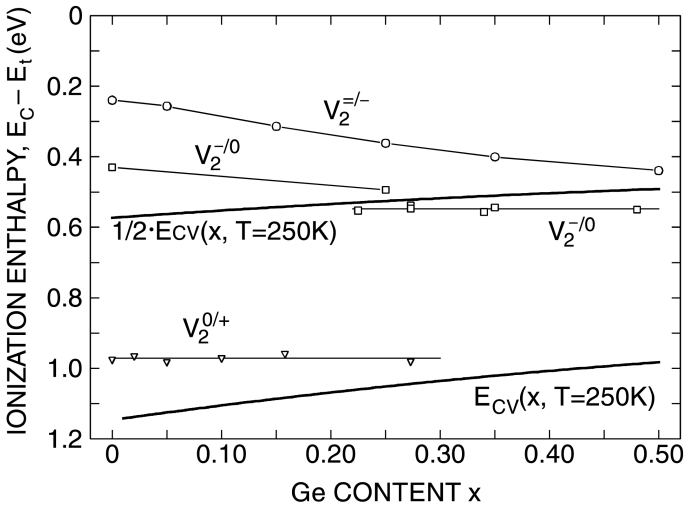

Figure 4.9: Figure from [av Skardi 2002] showing the evolution of the di-vacancy energy levels as the Ge content is increased in $Si_{1-x}Ge_x$.

With the di-vacancy being such a prominent defect in Si one would intuitively expect it to play a role in Ge as well. The energy levels of V_2 have been followed in SiGe alloys as a function of Ge content up to 50% Ge by [av Skardi 2002] as shown in figure 4.9 from the paper. All three energy levels are seen to move towards the valence band with increasing Ge content. The result is that the donor level moves too close to the valence band to be observed by DLTS after about 30% Ge, the single acceptor crosses midgap becoming a hole trap while the double acceptor has almost crossed midgap at 50% Ge. Assuming now that this trend continues all the way to pure Ge, we should then not expect to see di-vacancy energy levels in n-type Ge. This is unless of course a triple acceptor emerges from the conduction band, the existence of which is not predicted by theory. After crossing midgap the single acceptor is observed to be pinned to the conduction band at about E_c - 0.55 eV. Let us assume that this continues to hold to pure Ge and that the same

[6]In sufficiently oxygen rich material the oxygen-vacancy pair is dominant in n-type Si.

will happen when the double acceptor crosses midgab. Appoximate energy levels for the di-vacancy in Ge would then be: $V_2^{(-/0)} \sim E_v$+0.12 eV and $V_2^{(=/-)} \sim E_v$+0.19 eV[7]; using $E_g = 0.66$ eV to get positions relative to the valence band. Along the same lines the donor level would then be resonant with the valence band or too close to be observed by DLTS[8]. Another important finding from the study by av Skardi *et al*. is that the annealing temperature of V_2 shows no tendency to change markedly with Ge content. Thus we would expect an annealing temperature in the neighborhood of 250°C in pure Ge.

Only one theoretical study of the di-vacancy electrical properties has been carried out [Coutinho 2006]. The result of this is the prediction of the existence and position of the three di-vacancy energy levels also present in Si. These levels are: $V_2^{(0/+)} \sim E_v + 0.03$ eV, $V_2^{(-/0)} \sim E_v + 0.3$ eV and[9] $V_2^{(=/-)} \sim E_v + 0.26$ eV. Note that the single and double acceptor are predicted to have a negative-U ordering when the RT band gap is used. This means that the second hole on V_2^0 is weaker bound than the first, and thus that the single acceptor level is above the double acceptor level. However, using the low temperature band gap size ($E_g = 0.74$ eV) does not predict a negative-U ordering so all we can say is that the levels are predicted to be so close that a negative-U ordering is not precluded. While the authors do not comment on this possibility in the above paper private communications with *J. Coutinho* has revealed that he agrees that a negative-U ordering is possible. This would mean that only the transition $V_2^{(0)} \leftrightarrow V_2^{(=)}$ would be visible as a single level (with twice the amplitude) to DLTS. While this is not in precise agreement with the above extrapolations and theoretical predictions as to the positions of the acceptor levels, there is qualitative agreement that the levels are in the lower part of the band gap and relatively closely spaced. In addition, typical uncertainties on the level positions predicted from DFT calculations are on the order of 0.1 eV making the agreement acceptable. Particularly when keeping in mind that

[7]This is a very rough estimate since the actual crossing has not been observed by DLTS. Assuming the same crossing trend as for the single acceptor would give almost degenerate single and double acceptor levels, however there should be a barrier for electron capture at the singly negative di-vacancy pushing the levels apart.

[8]The emission rate would be too high to detect by DLTS for levels more shallow than about 35 - 40 meV in Ge assuming a capture cross-section on the order of 10^{-15} cm^2

[9]Where the RT value of the band gap size $E_g = 0.66$ eV has been used for definiteness to convert position relative to the conduction band into a position relative to the valence band.

the extrapolation is rather approximate in nature. Also, the donor level is calculated to be very close to the valence band which is in agreement with the prediction that the level is very close to or resonant with the valence band. Theoretical as well as extrapolated energy levels are shown in figure 4.10.

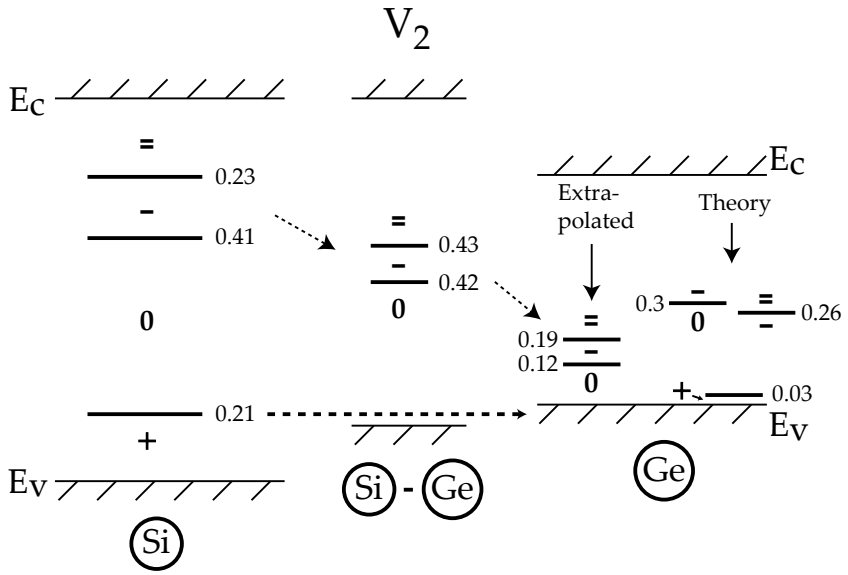

Figure 4.10: The energy levels of the di-vacancy in Si (left) as well as those found in SiGe with an equal content of Si and Ge (middle) [av Skardi 2002]. Also shown are the expected acceptor levels in Ge by extrapolating the SiGe results (right), assuming they stay pinned to the conduction band all the way to pure Ge, as well as the levels resulting from DFT calculations (right) [Coutinho 2006]. Note that the donor level is seen to be pinned to the conduction band (indicated by the horizontal dashed arrow) until it becomes too shallow to detect.

As to the thermal stability of the di-vacancy in Ge there are two theoretical studies calculating the binding energy [Janke 2007] and the migration energy [Chroneos 2006]. While the former study uses both a supercell and a cluster method the cluster method is argued to be more trustworthy. The result is that the migration barrier for V_2 is 1.1 eV, being lower than the dissociation barrier of 1.6 eV. The latter study only calculates the binding energy which is found to be 1.17eV. In the case of Si the migration barrier was found to be 1.3 eV [Watkins 1965] which is not too far off from the theoretical value mentioned for Ge. Based on this it is not unreasonable to expect the di-vacancy

to be stable at RT in Ge. On the other hand the rather low binding energy calculated by [Chroneos 2006] could indicate the opposite. This different conclusion despite comparable energy barriers is due to the fact that dissociation only requires one jump of the defect while migration to a sink or trap requires a vast amount of jumps. Therefore the prefactor of the annealing rate differ by many orders of magnitude.

The observation of stable di-vacancies above 473 K (200°C) by positron annihilation spectroscopy (PAS) has been reported by [Kuitunen 2008]. The authors irradiated n-type Ge with fast neutrons and subsequently observed a lifetime component consistent with a di-vacancy. This is in line with the indications that the di-vacancy is stable at RT from the calculations by Janke *et al*. and the trend mentioned above that the annealing temperature does not appear to change with composition in $Si_{1-x}Ge_x$. Note that the lifetime component attributed to V_2 was seen by the authors to depend on the temperature after the crystal has recovered. This indicates that the di-vacancy has at least one energy level in the band gap since the charge state changed.

In relation to the extrapolation introduced above between Si and Ge, through $Si_{1-x}Ge_x$, other experimental results should be mentioned. A similar experiment regarding the vacancy-oxygen pair [Markevich 2003] fit qualitatively quite well with the single acceptor electron trap shifting down towards the valence band and becoming a hole trap in Ge. In addition in pure Ge a double acceptor has emerged from the conduction band, or at least moved far enough away from the band to become observable by DLTS. In the case of the Sb E-center the single acceptor is seen to show the same trend moving down in the band gap until about $x = 20\%$ becoming a hole trap [Larsen 2008]. The level continues to shift down in the band gap as x is increased consistent with the single acceptor hole trap position in pure Ge. Furthermore in this case as well a double acceptor has emerged/moved away from the conduction band. The general trend then is interestingly that electron traps are relatively more efficient at binding electrons in Ge than in Si and can even in several cases (SbV and VO at least) accommodate one more electron than in Si. In conclusion it is considered a good way to try and predict level positions in Ge based on those in Si through $Si_{1-x}Ge_x$. Also it is not entirely impossible to have a triple acceptor di-vacancy level emerge from the conduction band in Ge from

the looks of it.

4.2.1 N-type

Inspecting RT electron irradiations of n-type CZ-Ge diodes show indeed that there are no clear peaks in the DLTS spectrum apart from the donor-vacancy pair (cf figure 4.31). Additional peaks are however formed after a while at RT or after annealing at higher temperatures [Fage-Pedersen 2000]. On the other hand the di-vacancy would definitely not be expected to form as a secondary defect in n-type since the vacancy is unquestionably negative. Thus there is a Coulomb barrier for the association of two mono-vacancies, when the Fermi-level is in the upper part of the band gap as shown in figure 4.1. This is perfectly in line with the observation of the di-vacancy in n-type Si as a primary defect [Corbett 1961]. Additionally larger vacancy clusters, which could be thought to break up into smaller clusters including di-vacancies, should not be expected. This is due to (1) the negativity of the vacancy and (2) the rather low energy transfer to the primary knock-on atom (PKA) from 2 MeV electrons[10]. There is thus no sign of di-vacancy states in the upper part of the band gap after RT electron irradiation.

4.2.1.1 Displacement threshold

Before proceeding it is of interest to go into some detail as to the displacement process induced by the incoming radiation which is responsible for the formation of defects. A certain minimum energy, denoted E_{d}, has to be transfered to the PKA in order to allow the atom to move out of the lattice site and into an interstitial site. In reality this energy depends on the direction of displacement of the atom so we denote the minimum of all such energies by E_{th}, the displacement threshold energy. There is a substantial spread in this parameter in the literature for Si as well as for Ge varying both in the region around 10-30 eV. Early results gave very similar values for Si and Ge, 12.9 eV and 14.5 eV respectively [Loferski 1958]. A later study using more detailed modeling and taking into account the anisotropy of E_{d} on the other hand gave 22 eV for

[10] As previously estimated a maximum of 178 eV is transfered to the PKA when the incident electron energy is 2 MeV.

Si [Hemment 1969]. Yet another study estimated a threshold of about 27.5 eV for Ge [Callcott 1967].

While it is clear from this that it is definitely not an easy task to determine the true E_{th} it appears that the variation is due to the different methods used. One may then speculate that the value for the two semiconductors is not too different given the very similar lattice. In addition, due to the lower melting point of Ge, and thus a lower binding energy of the atoms, one would expect a higher value for Si if the binding energy plays a major role; as seen from the values given above this is not the trend.

Comparing now the irradiation of Si and Ge with 2 MeV electrons we deduce that while a Ge PKA can gain up to about 178 eV by scattering with a 2 MeV electron this value is around 470 eV for Si. Assuming a similar value of E_{th} as discussed above the situation is then that a Si PKA can gain energy to induce substantially more displacements.

The generation of more complicated vacancy defects such as the di-vacancy may then be suppressed due to too low an energy transfer in Ge. To investigate this matter the energy of irradiation or the mass of the particles used for irradiation can be increased to transfer more energy to the displaced atoms. The latter is opted for in our case since the energy can not be increased substantially, while still maintaining a stable terminal voltage, on our Van de Graff accelerator.

4.2.1.2 Irradiation with heavier particles

In fact an earlier study [Fage-Pedersen 2000] on n-type Ge observed a shoulder to the E-center in proton irradiated samples, which was tentatively suggested to be related to the di-vacancy or di-interstitial defect. To investigate this further we carried out alpha particle irradiations of n-type Ge as published in [Kolkovsky 2007]. If this shoulder is indeed related to the di-vacancy one could then expect that alpha particles would enhance it even further, thus our choice of irradiation particle.

Figure 4.11 shows the DLTS spectrum after the lowest dose (2×10^{10} cm^{-2}) 2 MeV α-particle irradiation of an n-type Ge Schottky diode. The spectrum contains one major peak corresponding to the E-center double acceptor, SbV$^{=/-}$ and two minor peaks labeled according to their activation energy as found

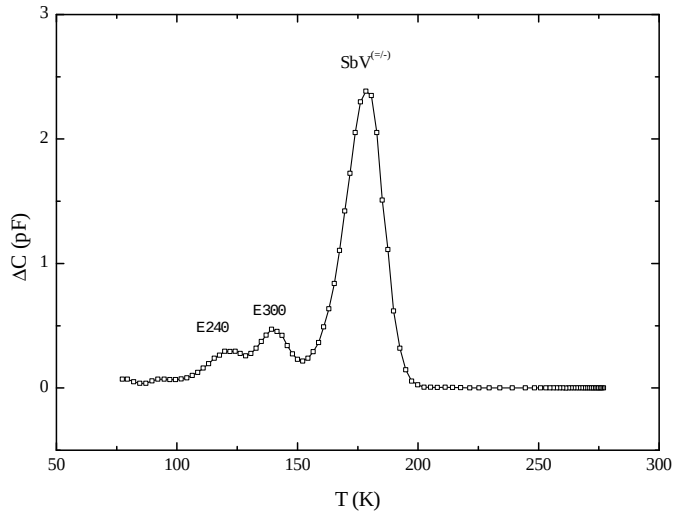

Figure 4.11: A DLTS spectrum measured after RT irradiation of an n-type Ge Schottky diode with 2 MeV alpha particles to a dose of 2×10^{10} cm^{-2}. Measurement settings were $e_n = 20$ s^{-1}, $\tau = 1$ ms, $V_r = -5$ V, $V_p = -0.5$ V.

by Laplace DLTS, E240 and E300. The two minor peaks resemble features present in previous studies after electron irradiation [Poulin 1980] (E_1 and E_5), neutron irradiation [Nagesh 1988] (E_2 and E_3) as well as in the mentioned study where the shoulder of interest is seen [Fage-Pedersen 2000] ($E_{0.23}$ and $E_{0.27}/E_{0.30}$). The first study attributed the peak similar to E300 along with another peak (E_4) to the di-vacancy based on the displacement threshold being higher. Judging from the position of this second peak in their DLTS spectrum, it could well be the shoulder seen by Fage-Pedersen *et al*. However, the irradiation fluence used by Poulin *et al*. was extremely high ($10^{15} - 10^{16}$ cm^{-2}) especially compared to the low doping level of their diodes ($\leq 10^{13}$ cm^{-3}), which makes the results questionable in the light of the difficulty of determining the displacement threshold as discussed above.

Coming back to the observed DLTS spectrum in figure 4.11, there is only a weak sign, if any, of the shoulder that was seen in [Fage-Pedersen 2000]. We decided to try higher irradiation doses to see if the shoulder would stand out. This did not turn out to be the case and in fact the DLTS spectrum changed radically. With irradiation doses of 4×10^{10} cm^{-2} and higher, a new prominent peak labeled E290 appears in the spectrum. Also the Sb-vacancy double

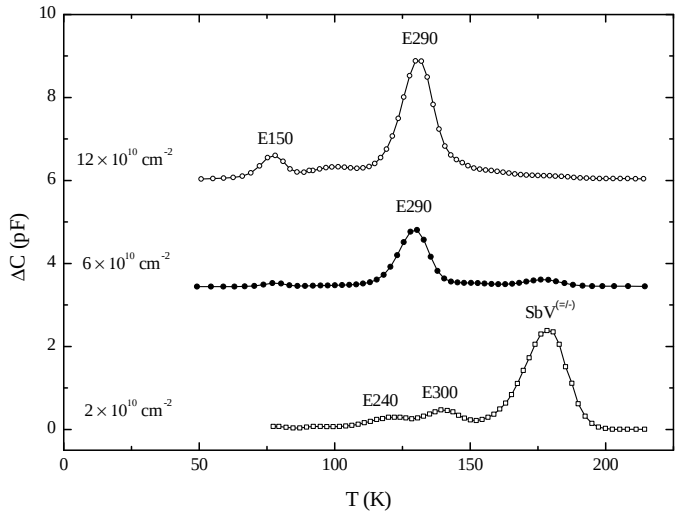

Figure 4.12: DLTS spectra recorded on n-type Ge Schottky diodes after irradiation with different doses of 2 MeV alpha particles at RT. The dose is noted next to the respective spectrum.

acceptor peak decreases rapidly as demonstrated in figure 4.12 where three different doses of alpha particles are compared. E290 is characterized by an electron capture cross-section of $\sigma_n = 3 \times 10^{-16}$ cm^{-3}, measured directly by varying the filling pulse; found to be independent of temperature. The position of the energy level is $E_{na} = 0.286 \pm 0.004$ eV. No dependence of the emission rate on the electric field, and thus no Poole-Frenkel effect, was observed. Together with the absence of a barrier for electron capture, this could indicate that E290 is a single acceptor.

With the sudden appearance of E290 as a function of dose, it would appear that we are dealing with a secondary defect. This suspicion is confirmed by the introduction rate as a function of dose being a quadratic function, figure 4.13. This is the signature of a diffusion-limited formation process involving two primary radiation introduced defects, as treated theoretically in great detail by [Waite 1957]. Furthermore the fact that the Sb-vacancy pair is only present at a very low concentration when E290 is present, indicates that vacancies are effectively trapped in the process of the formation of E290.

Both vacancies and Sb-vacancy pairs are negatively charged in n-type material as shown by the energy levels discussed elsewhere (figure 4.1 and 4.24)

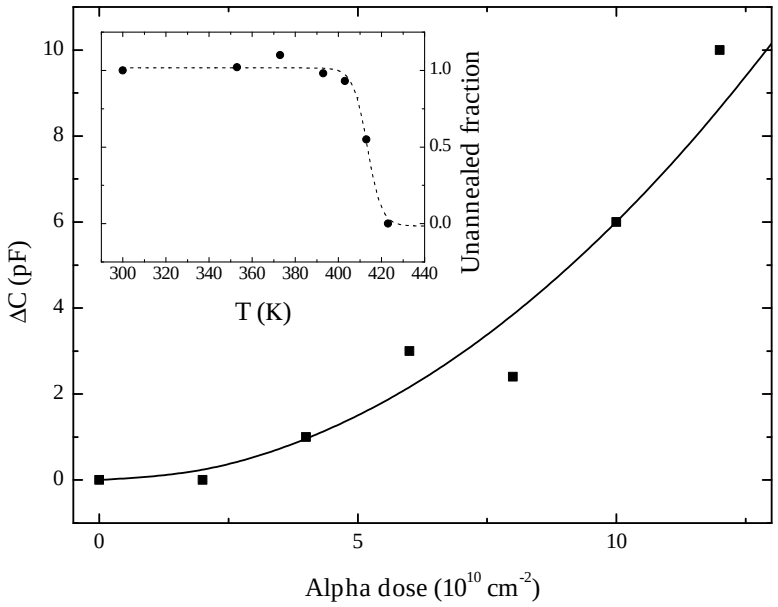

Figure 4.13: The dose dependence of the amplitude of the E290 energy level including a quadratic fit demonstrating the secondary nature of the underlying defect. In the inset the annealing characteristics resulting from 20 minutes isochronal annealing steps are shown.

so we do not expect E290 to be related to V_2 or Sb-V_2 due to Coulomb repulsion. Also the involvement of Sb in the defect does not appear to be the case as the introduction rate is found to be similar in higher resistivity (lower Sb concentration) material.

Interestingly a very similar peak has been seen in DLTS studies after ion implantation into n-type Ge by [Auret 2006] and [Peaker 2005]. They however did not observe its formation as a secondary defect. Note from the SRIM simulation in figure 4.14 that E290 is not related to an end of range defect or helium for that matter (assuming helium is immobile at RT). The observation region of our DLTS spectrum is shown in the figure by the double arrow, and is far from the end of range.

This is in line with the findings of Auret *et al*. who found that the emission rate did not depend on the implanted ion. However, a SRIM simulation shows that the projected range of their implantation, 160 keV indium into Ge, is only

about 52 nm. Meanwhile the DLTS observation region for their settings can be estimated to be about 1 μm → 1.6 μm. Since the implantation could be expected[11] to form a shallow p-type layer of $N_a \approx 10^{16}$ cm^{-3} (calculated from SRIM) the observation region might be even deeper.

On the basis of this one would then expect the introduced defects seen by DLTS to be due to point defects that has diffused into the sample from the implantation region. This is in contradiction with the DLTS spectrum being quite different from that after electron irradiation. In fact this very situation has been observed in the case of p-type Si [Nielsen 2003] where Si and Ge were implanted into the top layer of n^+p Si mesa diodes. In the end it was found that there was significant channeling of the incident ions far beyond the projected range. This was based on crystal-TRIM simulations [Posselt 2000] explaining the observation of end of range damage in the DLTS region. Crystal-TRIM takes into account the crystal structure of the semiconductor (which SRIM does not), allowing for channeling. Auret *et al*. do not comment on this point which is most likely the reason they can actually observe complicated radiation damage in their experiment.

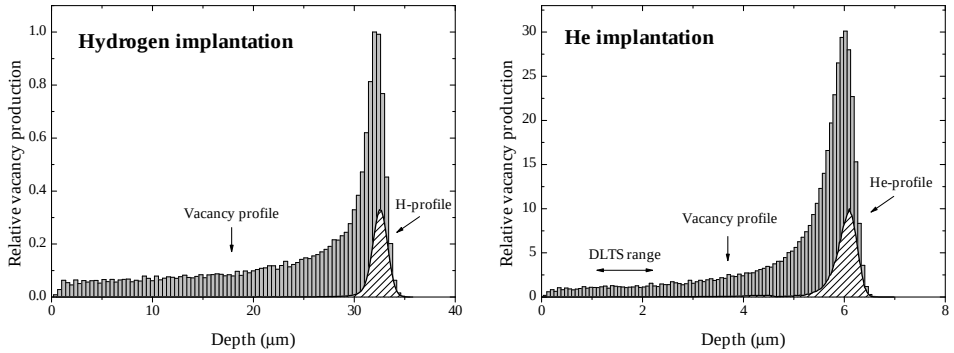

Figure 4.14: SRIM monte carlo simulation of the vacancy production resulting from 2 MeV proton (left) and helium (right) implantation.

What we have witnessed here is the transition from simple electron-like radiation damage to ion implantation-like damage. Our observations are not inside the end of range (EOR) region, but we still observe a dominant peak in the

[11]This is assuming all implanted indium is electrically active which is probably not the case without annealing.

DLTS spectrum very similar to that observed inside the EOR by [Peaker 2005] and [Auret 2006]. We can then conclude that the dominating defect, E290 introduced by ion implantation and active in the upper part of the band gap is in fact not necessarily a primary defect.

Since vacancies (figure 4.1) and di-vacancies (figure 4.10) are believed to be negative in n-type Ge one could speculate that E290 is formed by a vacancy-complex with more than 2 vacancies in its structure capturing a vacancy[12]. The result is that either the vacancy complex is stabilized, allowing the observation, or it is simply made electrically active (in the upper part of the bandgap at least) by the vacancy capture.

The secondary nature of E290 rules out it being related to the di-vacancy which should be present as a primary defect in n-type Ge as argued above. Isochronal annealing showed the defect to anneal at around 140°C (see the inset on figure 4.13), which is surprisingly low for a defect that is dominant in the damage introduced by implantation. The annealing temperature found by Auret *et al*. appears to be higher, but their annealing study was not detailed enough to give a more precise value than in the range 100 to 200°C.

Annealing was carried out for the lowest dose irradiation as well in which case a new small peak, EN300 appeared coinciding with the shoulder observed by Fage-Pedersen *et al*. We must then conclude that EN300 is only present after dissociation of more complicated defects, possibly interstitial clusters and can thus not be related to the di-vacancy which should be present immediately after irradiation.

The bottom line is that we must conclude that either the di-vacancy is unstable at RT in n-type Ge or it does not introduce any levels in the upper part of the band gap. In the low temperature electron irradiations discussed previously there are no clear candidates left for attributing to the di-vacancy. Even if V_2 is unstable at RT we are then not able to observe any energy levels of it in the upper part of the band gap before it anneals. As mentioned above though, it is not really a surprise not to find energy levels related to the di-vacancy in the upper part of the band gap. Based on everything discussed above we do not find it likely that the di-vacancy is highly unstable at RT.

[12]This is naturally assuming that the di-vacancy is immobile at RT leaving only the mono-vacancy as a candidate.

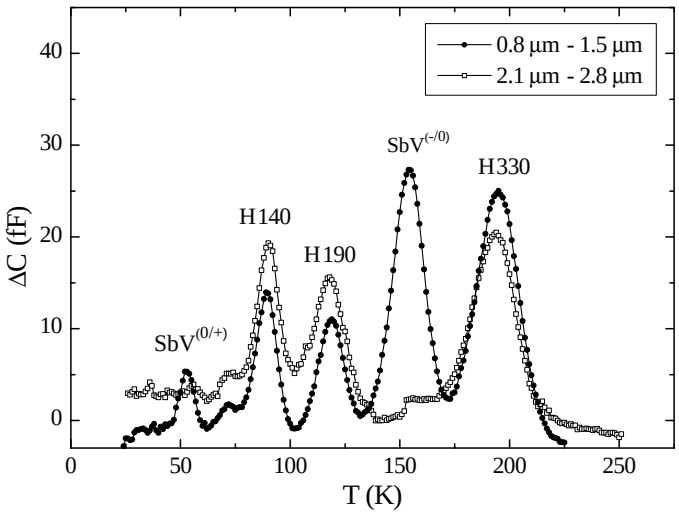

Figure 4.15: DLTS spectra recorded on an n^+p Ge diode after RT irradiation with 2 MeV electrons to a dose of 2.3×10^{15} cm^{-2}. In the shallow region (filled circles) the two E-center energy levels are visible while in the deeper region (open squares) they are absent. DLTS measurement settings were $e_p = 868$ s^{-1} and $\tau = 80$ µs for both spectra. For the shallow region pulse settings were $V_r = -2$ V, $V_p = 0$ V and for the deeper region they were $V_r = -10$ V, $V_p = -5$.

4.2.2 P-type

Having concluded that the di-vacancy is not visible by DLTS in the upper part of the band gap we continue our search in the lower part using n^+p Ge mesa diodes. A spectrum from such a diode after 2 MeV electron irradiation is shown in figure 4.15. Two energy levels of the SbV defect, present due to the Sb tail from the top-layer, appear under the proper bias conditions. The peak labeled H330 will be identified in a later section.

In order to check if the remaining unidentified peaks, labeled H140 and H190 are related to the dopant Ga, two diodes with the Ga concentration differing by about a factor of four were irradiated with the same nominal dose of 2 MeV electrons. The resulting DLTS spectra are shown in figure 4.16 demonstrating that there is no major change in the spectrum with the increase of Ga content. Also the H330 peak, which will later be seen not to be Ga related, shows about the same increase as the other peaks. Thus it can be concluded that the increase is most likely due to an uncertainty in the dose rather than

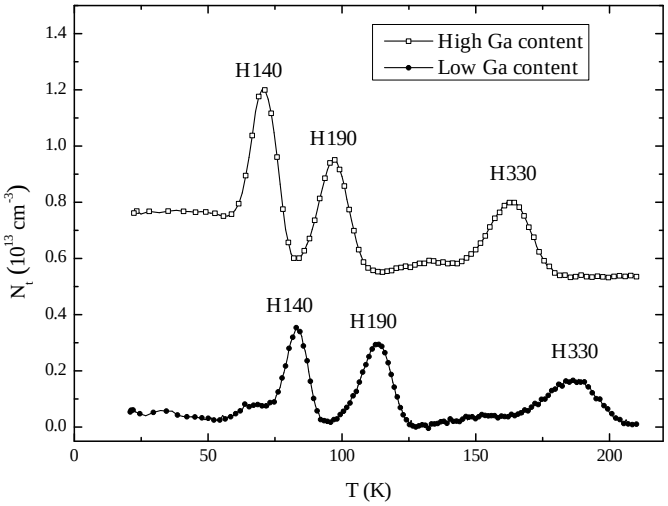

Figure 4.16: Comparison of DLTS spectra from two p-type Ge diodes with different Ga concentrations. Both diodes were irradiated with 2 MeV electrons at RT to a dose of 1.4×10^{15} and both DLTS spectra were recorded using $\tau = 1$ ms, $V_r = -2$ V and $V_p = -0.5$. The spectrum for the diode with the high Ga concentration (upper), [Ga] = 1.8×10^{15} cm^{-3} was recorded using $e_p = 20$ s^{-1} while that with the low concentration (lower), [Ga] = 4.4×10^{15} cm^{-3} was with $e_p = 400$ s^{-1}.

an increase in Ga content. It appears thus that H140 and H190 do not involve Ga.

H140 has an activation energy of $E_{pa}(\text{H140}) = 0.138$ eV and a capture cross section of $\sigma_{pa}(\text{H140}) = 1.2 \times 10^{-14}$ cm^2. For H190 the parameters are: $E_{pa}(\text{H190}) = 0.186$ eV and $\sigma_{pa}(\text{H190}) = 5 \times 10^{-15}$ cm^2. H140 exhibits a field effect compatible with a phonon-assisted tunneling mechanism, $\ln[e(\mathcal{E})/e(0)] \propto \mathcal{E}^2$, as shown in figure 4.17 and thus could appear to be a donor level. In addition the capture cross-section of H140 has a weak temperature dependence with $\Delta E_{p\sigma} = 2.9 \pm 0.2$ meV and $\sigma_{p\infty} = 4.2 \times 10^{-15}$ cm^2 supporting a donor nature. Given the intermediate value of the capture cross-section a single donor level is plausible.

Since we only expect to detect acceptor levels related to the di-vacancy, based on the extrapolation as well as theory introduced earlier, H140 is preliminarily discarded as a di-vacancy level candidate. Meanwhile H190 does not exhibit a substantial field effect, but based on the absolute value of the

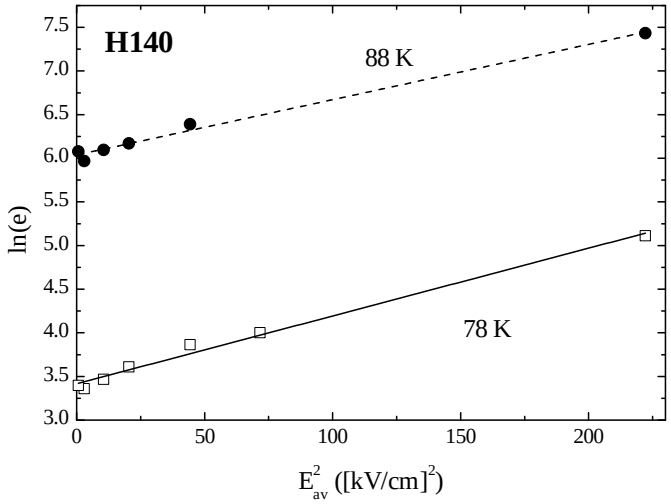

Figure 4.17: Demonstration of the field dependence of H140 at two different temperatures, 78 K (lower) and 88 K (upper). Straight line fits to the two datasets are included to show clearly that $\ln[e(\mathcal{E})/e(0)] \propto \mathcal{E}^2$ so phonon assisted tunneling is likely responsible.

apparent hole capture cross section a single acceptor or single donor level character seems plausible. H190 being a donor level is not compatible with an energy level of the di-vacancy since this would imply that one (in the case of a negative-U ordering) or two additional higher temperature DLTS peaks should be seen while this is the last peak left.

In fact the real capture cross section of H190 is so high that a reduction of the filling pulse duration to 50 ns[13] does not give a measurable reduction in the DLTS amplitude. Based on this observation the capture cross section can be estimated to be at least $\sigma_p \approx 10^{-13}$ cm^2 which strongly favors an acceptor character due to the high value. In addition the large ratio between the apparent (σ_{pa}) and real (σ_p) capture cross section indicates a large entropy change upon hole emission.

In the case of a negative-U ordering one could imagine the capture process, in addition to the emission process, to be limited by the second hole capture in effect making the level act as a single acceptor even though the full transition

[13]Reduction of the pulse duration to this short a time requires special electronics to avoid overload of the CV-meter during the filling pulse.

probed by DLTS would be $V_2^= \leftrightarrow V_2^0$. H190 can therefore in principle account for both di-vacancy acceptor levels assuming this ordering. In the absence of a negative-U ordering a single acceptor is however not compatible since the double-acceptor should then give a DLTS peak as well.

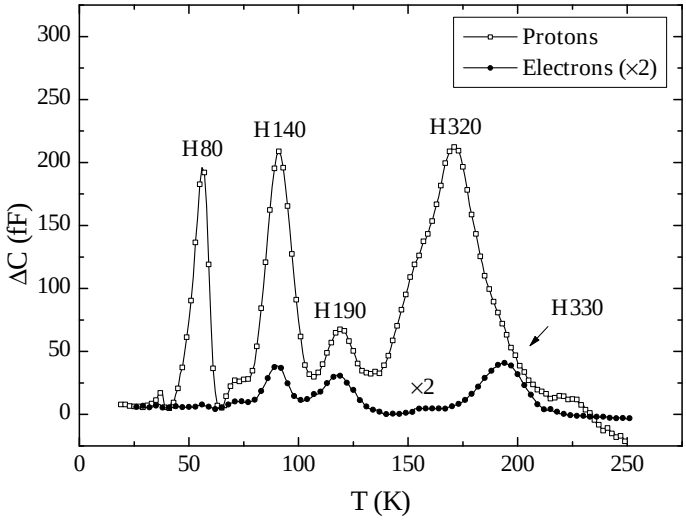

Figure 4.18: The DLTS spectrum from a p-type n^+p Ge diode irradiated with 1.8 MeV protons to a dose of 2.2×10^{13} cm^2. Measurement settings are $e_p = 868$ s^{-1}, $\tau = 80$ μs, $V_r = -10$ V, $V_p = -5$ V. The spectrum from an electron irradiation is included for comparison (multiplied by a factor of 2).

As in the case of n-type a natural next step to gain insight into the nature of the defects seen by DLTS is to use heavier particles for the irradiation. The DLTS spectrum resulting from a 2 MeV proton irradiation at RT is shown in figure 4.18. Surprisingly a peak denoted H80 appears at the position where the SbV donor level is present near 0 V (cf section 4.3.1). The characteristics of H80 are $E_{pa}(\text{H80}) = 0.076$ eV and $\sigma_{pa}(\text{H80}) = 6 \times 10^{-14}$ cm^2 with the emission rate having a field dependence fitting the Poole-Frenkel effect, $\ln[e(\mathcal{E})/e(0)] \propto \sqrt{E}$, as shown in figure 4.19. This field dependence shows that H80 is an acceptor level and thus not the donor level of the Sb-vacancy pair, which has very nearly the same position in DLTS spectra when the bias settings are right to reveal it. The capture cross section does not exhibit a variation with temperature and is measured to be $\sigma_p(\text{H80}) = (3.6 \pm 0.4) \times 10^{-15}$ cm^2.

At this point one can speculate that H80 is not formed (at a high enough

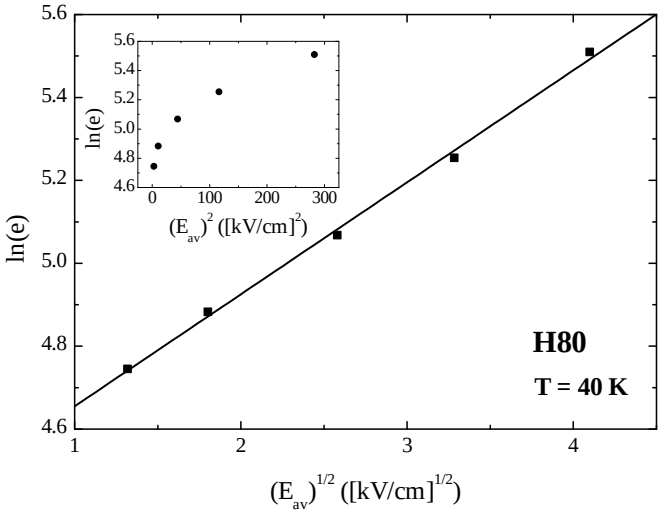

Figure 4.19: Demonstration of the Poole-Frenkel effect, $\ln[e(\mathcal{E})/e(0)] \propto \sqrt{\mathcal{E}}$, of H80 and thus that the level is an acceptor level. The inset shows that a Phonon-assisted tunneling mechanism is not consistent with the field dependence.

concentration to defect) by 2 MeV electron irradiation due to the energy transfer being too low. In addition a second dominant peak denoted H320 appears with an unresolved shoulder both of which there was virtually no sign of in the case of electron irradiation. It can be ruled out that H320 as well as H80 are proton-related since the same features are seen in alpha-particle irradiations as shown in figure 4.20 and reported in [Petersen 2006]. Furthermore the proton end of range is far from the DLTS region (a SCR width of about 7 μm represents the maximum reachable depth with our samples) as seen in the already shown figure 4.14 showing SRIM simulations (the end of range is not until a depth of about 25 - 30 μm). The characteristics of H320 are E_{pa}(H320) = 0.324 eV and σ_{pa}(H320) = 2×10^{-15} cm^2.

While it is tempting to think that H80 and H320 are energy levels of the same defect due to the way they emerge and a similar amplitude, it will be seen later that they do not always appear together. These two levels then cannot be related to the same defect. Also both peaks are present in DLTS spectra even after the lowest proton doses as shown in figure 4.20. And so there is no indication of a secondary nature of these new peaks as was the case for the peak emerging in n-type alpha particle irradiations (section 4.2.1).

Therefore it appears that the formation of the defect responsible for H80, H320 and the unresolved features are made possible by the higher amount of energy transfer to the PKA, and thereby ability to induce a higher number of adjacent displacements.

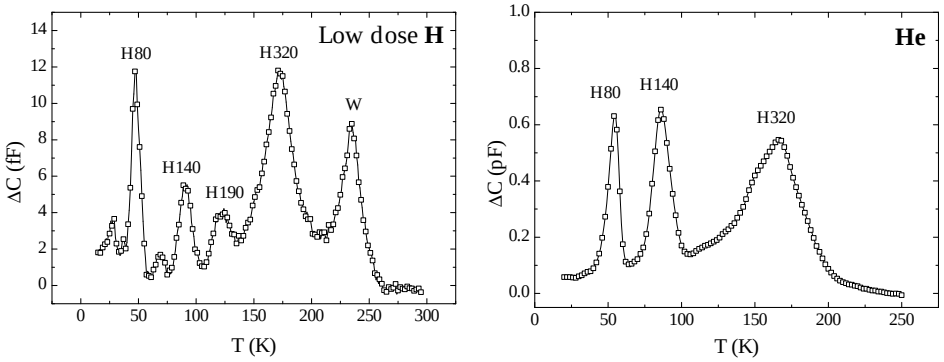

Figure 4.20: DLTS spectra of n^+p Ge diodes irradiated at RT with a very low (unknown) dose of 2 MeV protons (left) and a moderate dose (1.3×10^{13} cm^{-2}) of 2.5 MeV alpha particles (right). Measurement settings for the proton irradiated diode (left) were $e_p = 1085$ s^{-1}, $\tau = 100$ µs, $V_r = -8$ V and $V_p = -5$ V. For the alpha particle irradiation (right) the settings were $e_p = 868$ s^{-1}, $\tau = 80$ µs, $V_r = -10$ V and $V_p = -5$ V. The peak marked W is not seen consistently and has not been investigated.

At this point it is important to note that high levels of radiation damage could in principle void the assumption that the pn-junction is one-sided. The irradiation will in particular form Sb-vacancy pairs (cf 4.3.1) in the Sb-doped n-type top-layer which will lower the carrier concentration. In addition vacancies created inside the SCR will be drifted towards the top-layer making the effect even stronger close to the end of the SCR on the n-side. If the carrier concentration is lowered enough in this region the SCR will expand and contract at both ends in response to voltage changes giving then also DLTS signals from the n-side. If this is the case here we should see the SbV double acceptor peak as a clear marker since SbV would be very abundant in the active region on the n-side under the above assumptions.

From the emission data in [Markevich 2004b] the peak position of the double acceptor is calculated to be $T_{max} = 210$ K at an emission rate of $e_n = 868$ s^{-1} and $T_{max} = 180$ K at an emission rate of $e_n = 20$ s^{-1}. There is no clear sign of a

peak at these positions in any of the DLTS spectra recorded on p-type diodes in this study. The conclusion is then that we can be sure that none of the new peaks that appeared after proton irradiation originate from the top-layer side of the diode as SbV is definitely the dominant defect there.

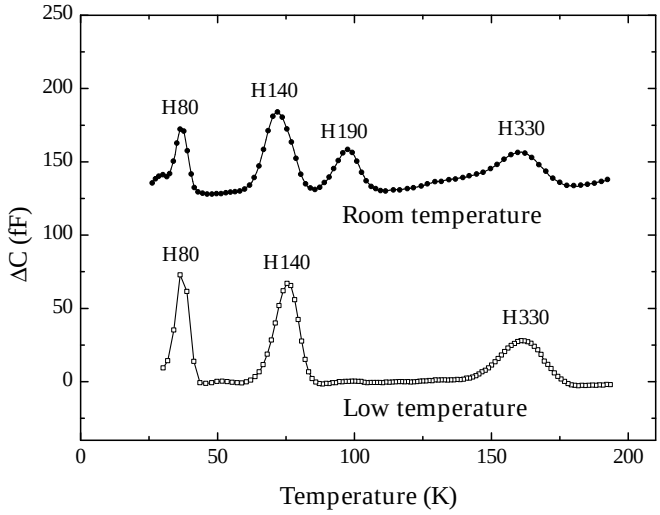

Figure 4.21: DLTS spectra comparing irradiation with 2 MeV electrons at low temperature (lower spectrum) with subsequent irradiation at RT (upper spectrum). Both spectra were recorded with the settings $e_p = 20\ s^{-1}$, $\tau = 1$ ms, $V_r = -5$ V and $V_p = -0.1$ V.

In fact H80 can actually be formed by electron irradiation under the right conditions. It was found that low temperature irradiation with 2 MeV electrons and subsequent heating to RT (under zero bias) is the key. A DLTS spectrum resulting from this treatment is shown in the lower spectrum of figure 4.21. It should be noted that the doses required to get sufficient DLTS signal from the peaks stable at RT are too high to allow DLTS before the diodes have been brought to 200–250 K, thus the need for the heating step.

Figure 4.22 demonstrates that the peaks stable at RT are indeed introduced at a rate several hundred times lower than the Y peak (scaled down by a factor of 100 in the figure). This peak is the topic of section 4.3.2 and will be seen to have the self-interstitial concentration as an upper limit. The explanation is thus that at the required dose the concentration of elementary point defects (vacancies, self-interstitials and FPs) is too high immediately after irradiation

to allow the diode to function. Note that the minority signal marked by Q in figure 4.22 is likely due to the E-center double acceptor where the observation is made possible by a weak injection of electrons across the SCR. This signal is only visible at very low irradiation doses which makes sense since the amplitude should be limited by the leakage current which in turn does not change much unless the dose is extremely high.

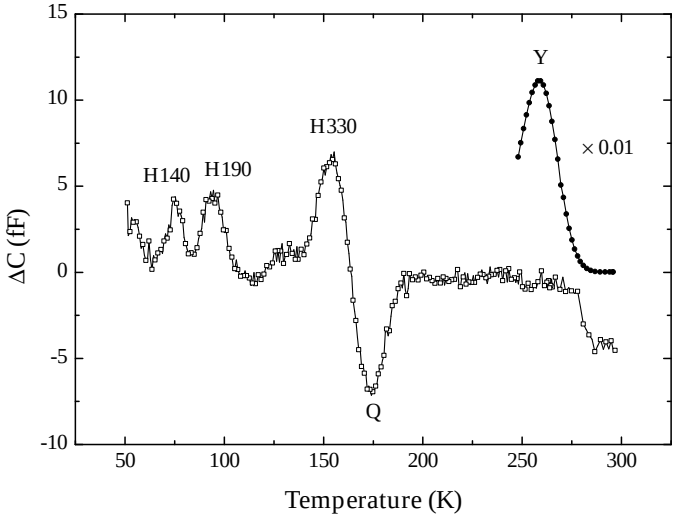

Figure 4.22: DLTS spectra comparing the amplitudes of the peaks stable at RT (open squares) with the amplitude of the Y peak discussed in section 4.3.2 (filled circles) after 2 MeV electron irradiation. Both spectra were measured with a rate window of $e_p = 20\ s^{-1}$, pulse duration of $\tau = 3$ ms and quiescent reverse bias of $V_r = -2$ V. For the open squares the pulse bias was $V_p = 0$ V while for the filled circles $V_p = -0.5$ V.

Yet another feature emerges from the low temperature irradiation, namely that H190 is not present or at least strongly reduced referring again to figure 4.21. To check that the lack of H190 was in fact due to the low temperature irradiation the DLTS spectrum shown in the same figure resulted from a subsequent RT electron irradiation of the same sample. Since the RT irradiation caused H190 to appear it is thus confirmed that low temperature electron irradiation allows the formation of H80 while retarding the formation of H190.

It is hard to imagine a mechanism that would prevent the formation of a primary defect just because of temperature well below the annealing temperature of the defect. Therefore a more likely description is that due to different

charge states at lower temperatures, as the Fermi-level moves down in the band gap when the temperature is lowered, H190 can pair up with another defect to form something else, presumably H80. This is consistent with the fact that H80 can also be formed at RT by proton irradiation indicating that it is a more complicated defect.

In p-type the Fermi-level moves up in the band gap as the temperature is increased and thus the more negative charge states of defects are populated at higher temperatures. Since low temperature by assumption makes it possible for H190 to pair up with another defect, this other defect must then be negatively charged at RT for the pairing to be prevented. The likely candidate is then the vacancy, as the self-interstitial is not negatively charged (cf section 4.1.3), and in fact at 200 K where V becomes mobile in the neutral charge state, the Fermi-level is positioned at $E_F \approx E_v + 0.15\,eV$ which is below the H190 level. At RT $E_F \approx E_v + 0.24\,eV$, about 50 meV above H190, which is perfectly in line with the assumption of the conversion of H190 being prevented by the negativity of the defect at RT.

The above considerations mean that H80 and H190 are vacancy-type defects since H190 becomes a more complicated defect by vacancy capture. As argued above Ga does not appear to be involved in H190 (and H140) and thus neither in H80. Apart from oxygen no impurities are expected to be present at non negligible concentrations especially since the carbon solubility is extremely low (cf 4.3.4). The only thing to consider then is if these vacancy-clusters are decorated with oxygen. In the case of Si the oxygen-decorated di-vacancy, V_2O is not seen until V_2 becomes mobile [Mikelsen 2005] except at very high irradiation doses. Based on this it will be assumed that the same goes for Ge and thus that H190 and H80 does not contain oxygen.

As argued previously the energy transfer to the PKA when irradiating with 2 MeV electrons is relatively low. Therefore one would not expect H190 to contain a large amount of vacancies. In fact the natural suggestion for the defect responsible for H190 is V_2 since, as mentioned above, there are indications that the di-vacancy should be stable at RT and that at least one energy level should be introduced in the lower part of the band gap. On these grounds H190 is hereby tentatively assigned to the di-vacancy.

It should be noted that we have earlier argued that the di-vacancy did

not give any electronic levels, or is not present, in Ge after RT irradiations [Kolkovsky 2008a]. This was based on the observation that the peaks discussed above were not present immediately after alpha particle irradiations at low temperature, and thus appeared to be secondary defects. However after studying the large capacitance changes introduced by low temperature irradiation (cf figure 4.6), we no longer believe that we can conclude on the absence of peaks before the capacitance has recovered (at around 200 K).

Since no other DLTS lines correlated with H190 are seen this implies that the di-vacancy has a negative-U ordering of its acceptor levels and H190 is due to the transition $V_2^{(=/0)}$. Note that this means that the di-vacancy concentration is actually half of that implied by the peak amplitude. In the emission of this transition the rate-limiting step is the emission of a hole from the singly negative state meaning that it will behave as a single-acceptor. This is consistent with the remarks above that H190 could be a single acceptor based on the capture cross-section. Worth mentioning again is also the PAS study [Kuitunen 2008] which indicated that the di-vacancy has an acceptor type level in the band gap in agreement with the assignment of H190 to the di-vacancy.

The assignment of H190 to the di-vacancy means that H80 should be assigned to a tri-vacancy defect. Due to the fact that H80 exhibits a Poole-Frenkel effect, it is an acceptor level. However, the prefactor to $\sqrt{\mathcal{E}}$ does not fit a theoretical value so whether it is a single- or a double-acceptor can not be deduced. On the other hand the capture cross-section is rather low so a single-acceptor state is most probable. Therefore H80 is assigned to the transition $V_3^{(-/0)}$. The final remaining energy level H140 is seen to have annealing characteristics very similar to $V_2^{(=/0)}$ (H190) with an annealing temperature of 415 K for both as it is shown in figure 4.23. There is no apparent correlation between the amplitude of $V_2^{(=/0)}$ and H140 after irradiation (warranting also the earlier dismissal of H140 as a di-vacancy candidate), in particular the difference increases strongly when going from electron to proton irradiation as was seen in figure 4.18. Therefore we are dealing with two different defects and unless the identical annealing behavior is a remarkable coincidence it appears then that the two defects corresponding to these energy levels are annihilating with each other or some defect invisible to DLTS.

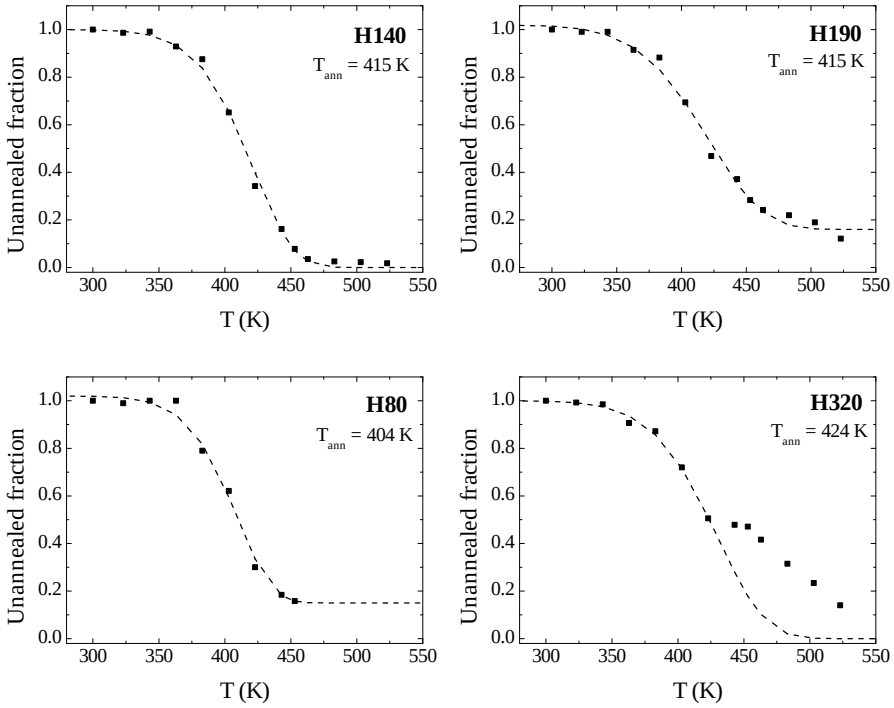

Figure 4.23: The isochronal annealing characteristics of the 4 dominant lines in proton irradiated p-type Ge extracted by DLTS. Individual annealing steps are of 15 minutes duration. Dashed lines are fits to guide the eye and extract the temperature of 50% concentration remaining, T_{ann}. The deviation from the dashed line for H320 is due to difficulty in resolving the corresponding peak from nearby features.

Assuming there is no invisible defect (to DLTS) which is dissociating and thus causing annihilation, this indicates that H140 is an interstitial-type defect possibly I_2, I_3 or I_4 since higher-order interstitial clusters than this seem unlikely as primary defects from electron irradiation as well as secondary defects due to Coulombic repulsion between mono-interstitials at RT. Unfortunately no theoretical studies of these higher order interstitial clusters are available. It does however seem unlikely that H140 is vacancy-related given we have already assigned V_2 and V_3, implying also that an annihilation process between H140 and H190 is in fact likely. In fact strong evidence of an I_2 defect in p-type Si has recently been observed [iii]. Therefore this defect is not unlikely to encounter in Ge, and being the simplest candidate H140 is preliminarily

assigned to I_2.

We can conclude (barring a remarkable coincidence) that the real annealing temperature of V_2 might very well be higher in line with the observation that the annealing temperature does not appear to depend on x in $Si_{1-x}Ge_x$ (up to $x = 0.5$), staying constant at around 250°C as mentioned above. In addition the previously mentioned PAS measurements [Kuitunen 2008] indicated that the di-vacancy is stable above 200°C which is also in favor of a higher intrinsic annealing temperature.

4.3 Impurity related defects

Defects involving impurities such as dopants, oxygen or carbon are usually not formed directly at great numbers by irradiation. Instead mobile primary defects (I and V) react with the impurities, pairing up or kicking out the impurity into an interstitial site. The following subsections treat the impurity related defects that typically form in Ge.

4.3.1 The donor-vacancy pair (E-center)

The donor-vacancy pair or E-center is the dominant defect as seen by DLTS in electron irradiated n-type oxygen lean Ge [Fage-Pedersen 2000]. Using DLTS and MCTS has resulted in the identification of two energy levels corresponding to the Sb-vacancy E-center [Fage-Pedersen 2000, Markevich 2004b]. The E-center versions from the other possible donors (As, P and Bi) have been studied in detail as well [Markevich 2004a].

The n^+p diodes developed by our research group has allowed the identification of a third energy level linked with the Sb-vacancy pair via the in-diffused tail of Sb from the top-layer [Lindberg 2005]. The complete level scheme for the Sb version of the E-center is shown in figure 4.24 for Si and Ge. The level scheme for the Si version of this is also shown, including the donor level which has in fact only recently been discovered [Larsen 2006].

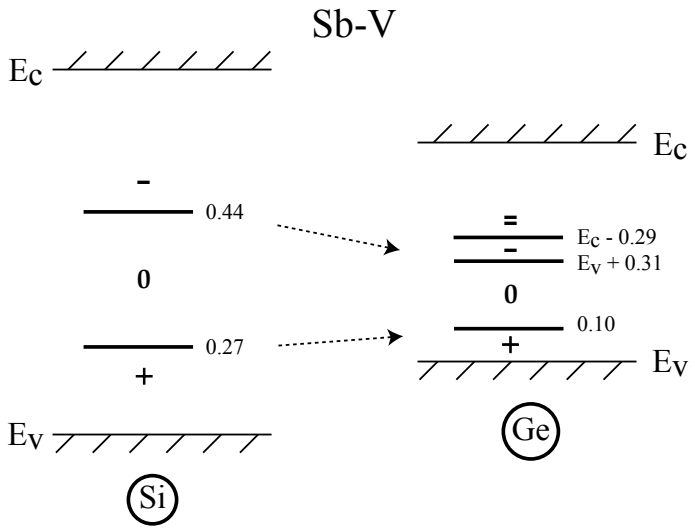

Figure 4.24: The donor and acceptor level of the Sb-vacancy pair (E-center) in Si (left) and the three energy levels of the same defect in Ge (right). The dotted arrows indicate the shift of the levels where only the single acceptor has been studied in SiGe [Larsen 2008]. The extra energy level in Ge is a double acceptor that has moved away from or emerged from the conduction band.

4.3.2 The interstitial gallium defect (Ga_i)

Being an acceptor in Si and Ge, Ga is negatively charged at all but the lowest temperatures (lower than 20 K). Since self-interstitials are positively charged in p-type Ge (see section 4.1.3) one could expect Ga-Ge_i complexes to form. In the case of Si the self-interstitials are seen to react with substitutional atoms such as aluminum (Al), boron (B), carbon (C) and Ga via the so called Watkins-replacement mechanism where the target is kicked out of the lattice site by the self-interstitial [Watkins 2000]. Electronic levels in the band gap exist in Si for Al_i, B_i and C_i while none has been found for Ga_i.

In the following it will be argued that the peak present after low temperature electron irradiation of p-type Ge labeled Y and previously shown in figure 4.2 is in fact an energy level of the Ga interstitial defect, Ga_i. These results were published in [Mesli 2008] and extended in [Kolkovsky 2008b].

Figure 4.25 shows a DLTS spectrum with the Y peak and a forward bias MCTS spectrum included showing the peak labeled Z. Since there is no sign of Y in the MCTS spectrum this indicates that the defect responsible for the

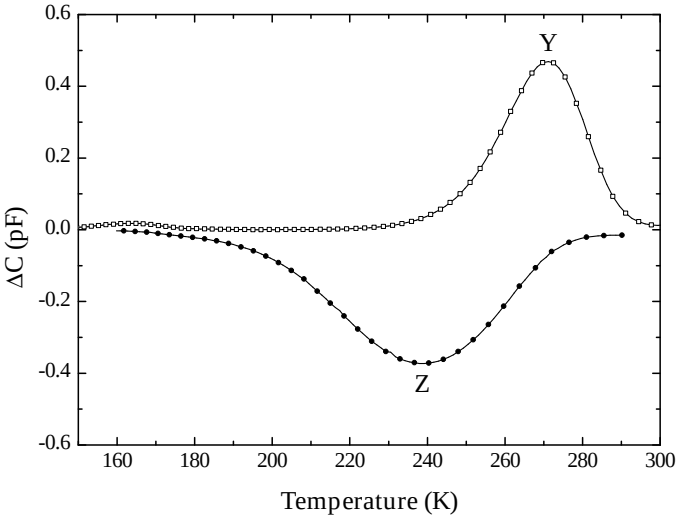

Figure 4.25: DLTS (open squares) and MCTS (filled circles) spectra showing the two peaks labeled Y and Z. For both DLTS and MCTS the rate-window was set at 20 s^{-1} and the filling pulse was τ = 5 ms. DLTS voltages were V_r = −8 V and V_p = −2 V. MCTS voltages were V_r = −3 V and V_p = +2 V.

energy level giving Y can capture both electrons and holes. It would thus appear that the defect has at least two energy levels giving rise to Y and Z.

Quite importantly no sign of a peak anywhere near the position of Z has been seen in DLTS spectra on n-type Ge diodes (cf figure 4.31). Additionally Y and Z are seen to have very similar annealing behavior under isochronal annealing. To ensure that the top layer is not involved in the formation of the defect we irradiated p-type Schottky Ge diodes with a lower doping level (see section 3.2) with 2 MeV electrons. Laplace DLTS as shown in figure 4.26 shows that Y is present in these diodes and confirms also that the top-layer is not involved. On these grounds we therefore conclude that Y and Z are energy levels of the same defect and that this defect is native to p-type Ge. Since the only impurity present at a high enough concentration to account for Y and Z is Ga this defect definitely involves Ga.

Laplace DLTS analysis of the Y peak shows that the transient is very purely exponential containing only one component. In line with this no field dependence is seen, which if present would broaden the emission rate in frequency space. Figure 4.27 shows the Arrhenius plot of the extracted emission rates

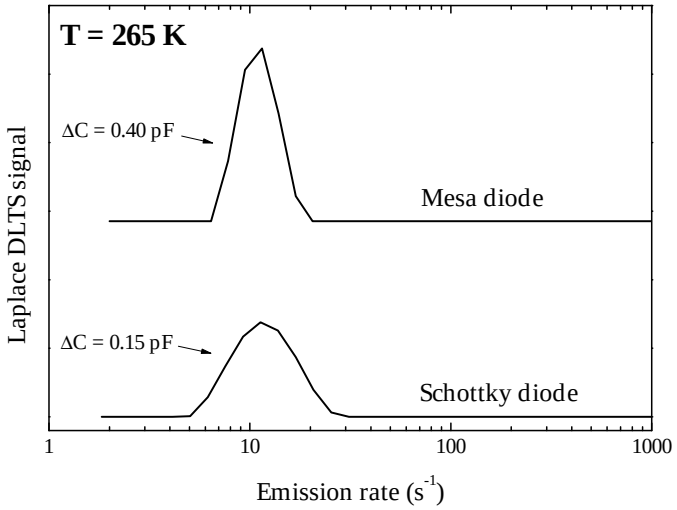

Figure 4.26: Comparison of Laplace DLTS spectra recorded after 2 MeV electron irradiation of a n^+p Ge mesa diode (upper) and a p-type Ge schottky diode (lower). Both spectra show the presence of the emission component giving rise to the Y peak.

giving $E_{pa}(Y) = 0.65$ eV and $\sigma_{pa} = 3.0 \times 10^{-13}$ cm^2. Such a high activation energy, nearly the full band gap, is unexpected for a defect interacting with the valence band since energy levels in the opposite part of the band gap typically emit too slowly for detection by DLTS. The answer lies in a temperature dependent capture cross section as the barrier for capture is then included in the activation energy found by DLTS measurements. Figure 4.28 shows the capture cross section, measured by varying the width of the filling pulse, as a function of temperature. The parameters extracted are $\Delta E_{p\sigma} = 0.32$ eV and $\sigma_{p\infty} = 10^{-13}$ cm^2 giving a capture cross section of $10^{-19} - 10^{-18}$ cm^2 in the temperature range 250 - 300 K. Combining emission and capture data leaves $\Delta H_p = 0.34$ eV. Note that σ_{pa} and σ_p are rather close to each other indicating a small or vanishing entropy change upon hole emission.

The analysis of Z is not as simple and it was not possible to isolate the main component in the transient by Laplace DLTS. However, the parameters of the Z energy level can be estimated from standard DLTS spectra to be $E_{na}(Z) \approx 0.3$ eV and $\sigma_{na} \approx 10^{-17} - 10^{-16}$ cm^2. This complies with the fact that the absence of Y in the MCTS spectra indicates that $\sigma_n \gg \sigma_p$ as both electrons and holes are injected in forward bias MCTS.

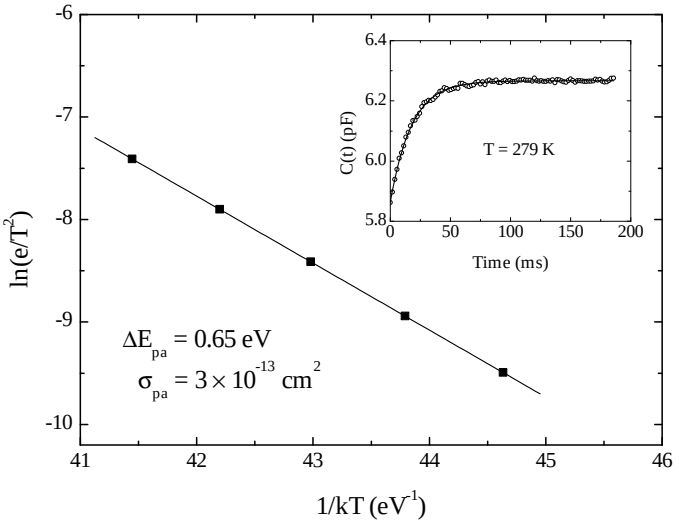

Figure 4.27: An Arrhenius plot for the energy level giving the Y peak measured by Laplace DLTS. The inset shows a measured transient fitted to a single exponential (solid line).

In order to investigate Z properly we grew n-type Ge counter-doped with Ga by MBE as an extension of the samples described in section 4.3.4. While the Schottky diodes made from this material did show a decreased donor concentration no peaks were seen anywhere near where Z should have been. This result is probably due to the fact that MBE samples are grown at elevated temperatures (in this case about 350°C) and an increased mobility of atoms on the surface causes Ga and Sb to pair up due to Coulomb attraction. The result of this is that the donor concentration is decreased even though no isolated Ga is introduced. It appears therefore that to do this kind of experiment properly the Ga would have to be implanted or incorporated during CZ crystal growth.

As both the capture cross section for holes and electrons are quite small in the common charge state for the Y and Z transitions the most probable common charge state is zero. Especially in the light of a total absence of a Poole-Frenkel effect[14], even in the samples with the highest Ga concentration. This implies that the barrier for capture of holes is not due to a repulsive center but instead should be related to a reconfiguration of the defect as it changes

[14]Even a slight field effect would make the transient deviate from a perfect exponential form.

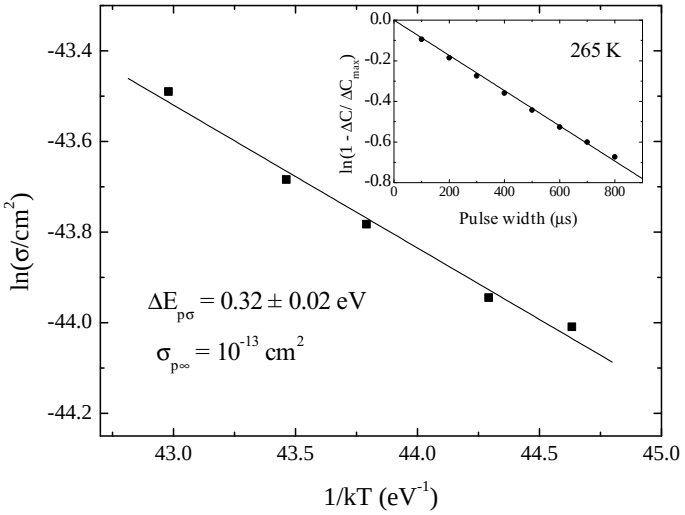

Figure 4.28: Arrhenius plot of the capture cross section as a function of temperature demonstrating that there is an energy barrier for hole capture ($\Delta E_{p\sigma}$). The capture cross section was measured by varying the filling pulse duration and extracting the capture rate as shown in the inset for one of the temperatures.

from the 0 to the + charge state.

It is seen that Y and Z anneal within minutes at RT with bias off, and thus with the defect in the positive charge state. However, the defect is much more stable at RT with reverse bias on the diode, which means it is in the neutral charge state. This difference in annealing kinetics is demonstrated in figure 4.29, which shows the result of isothermal annealing[15] experiments plotted in Arrhenius plots. Straight line fits demonstrate that the annealing rate follows Arrhenius laws, $1/\tau(T) = 1/\tau_0 \cdot \exp[-Q/(k_B T)]$. The extracted parameters for the annealing process differ in both prefactor and energy barrier for the two different conditions.

For the zero bias case the energy barrier is found to be $Q^{(+)} = 0.30 \pm 0.02$ eV, which is very close to the barrier for hole capture on the neutral defect, and a pre-exponential factor of $1/\tau_0^{(+)} = 5 \times 10^2$ s^{-1} is found. When a neutral charge state is enforced on the defect by having a reverse bias on the diode

[15]The remaining concentration of Y is followed as a function of annealing time at a fixed temperature. In all cases the concentration follows the simple expression $C(t) = C_0 \cdot \exp[-t/\tau(T)]$), allowing simple extraction of the annealing rate $1/\tau(T)$.

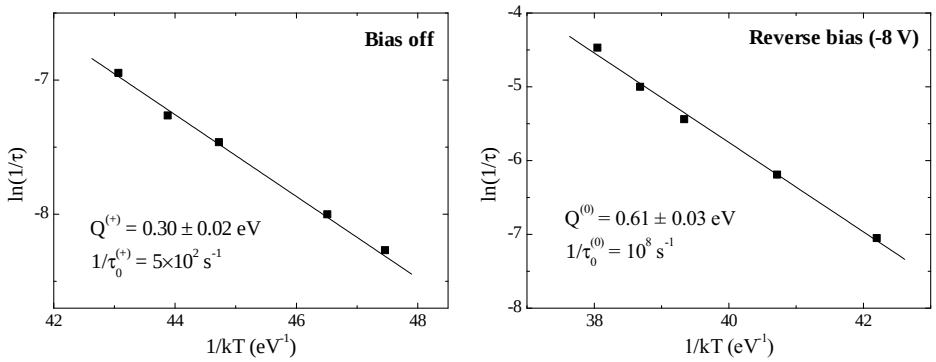

Figure 4.29: Arrhenius plots of the annealing rate of Y in the neutral charge state, with bias off (left) and the positive charge state, with reverse bias on the diode (right). The extracted energy barrier and prefactor for annealing in the two cases are shown on the figures.

the barrier is increased to $Q^{(0)} = 0.61 \pm 0.03$ eV with a pre-exponential factor of $1/\tau_0^{(0)} = 10^8$ s^{-1}. In the latter case the prefactor fits qualitatively to a long range diffusion to traps, in which case the prefactor would be on the order of the Debye frequency ($10^{12} - 10^{13}$ s^{-1} in Ge [Batterman 1962]) reduced by the number of required jumps to reach a trap ($10^4 - 10^5$).

A likely trap for the positively charged defect would be negatively charged substitutional Ga which is by far the most abundant impurity in the crystal ([Ga] $\approx 4\times10^{14}$ cm^{-3} in this case). The former prefactor is about a factor of 10^6 lower indicating that a different mechanism is dominating. The similarity of the activation energy for annealing with bias off, $Q^{(+)} = 0.29$ eV, with the energy barrier for capture of a hole on the neutral defect, $\Delta E_{p\sigma} = 0.31$ eV, could indicate that the capture of a hole is the limiting factor for annealing.

Additional enlightenment is gained by monitoring the annealing under forward bias and thus under the injection of minority carrier electrons. It is observed that an injection current of $J \approx 2$ A/cm^2 increases the annealing rate by about a factor of 4 at 252 K. Such a behavior has been observed before in the case of a recombination enhanced diffusion reaction [Lang 1974b], however with a much stronger enhancement of the annealing rate of about a factor of 10^6. An alternative explanation could be the Bourgoin mechanism [Bourgoin 1972] which is believed to be responsible for the athermal migration of self-interstitials in Si produced by electron irradiation at cryo-

genic temperatures. This mechanism describes migration through the lattice by repeated cycling between charge states.

The injection of minority carriers should be expected to increase the rate at which our defect switches between the + and 0 charge states[16] so a Bourgoin mechanism seems likely.

The annealing behavior of this defect is rather similar to that of the B_i defect in Si [Troxell 1980]. A marked difference however is that the two energy levels of B_i in Si have a negative-U ordering which there is no obvious sign of in our case. Based on this similarity, the fact that Ga must be involved in the defect and that positively charged self-interstitials are very likely to interact with negatively charged substitutional Ga, we conclude that our defect is the interstitial Ga defect, Ga_i produced by a Watkins replacement mechanism.

The energy levels corresponding to the two peaks are thus Y $\sim Ga_i^{(0/+)}$ and Z $\sim Ga_i^{(-/0)}$. No new energy levels are seen when Ga_i disappears, possibly forming Ga_i-Ga_s pairs, which is similar to the case of B in Si where B_i-B_s has no known energy levels in the band gap.

4.3.3 The vacancy-oxygen pair (A-center)

The vacancy-oxygen pair (VO) or A-center in Ge has been studied in n-type Ge using DLTS and MCTS by others [Markevich 2002] leading to the level scheme shown in figure 4.30 along with the one level of VO in Si for comparison. In that study the samples used for making Schottky diodes were grown with an intentional interstitial oxygen content of up to 10^{17} cm^{-3}. This is necessary since Ge crystals grown by the CZ process without deliberate introduction of water vapor contain a very low amount of oxygen.

Figure 4.31 shows the result of an electron irradiation of a Schottky diode made from CZ-grown n-type material. The arrow shows the position in the spectrum where the VO double acceptor peak would be. There is only a weak signal at this position, which sets an upper limit on the oxygen content of around 3×10^{12} cm^{-3} (calculated from (2.23)) in sharp contrast to Si-CZ crystals where 10^{18} cm^{-3} is typical, making VO a very important defect in CZ n-type Si.

[16]The rate of the transition + $\rightarrow$ 0 is increased under minority carrier injection by the addition of an electron capture term to the hole emission term.

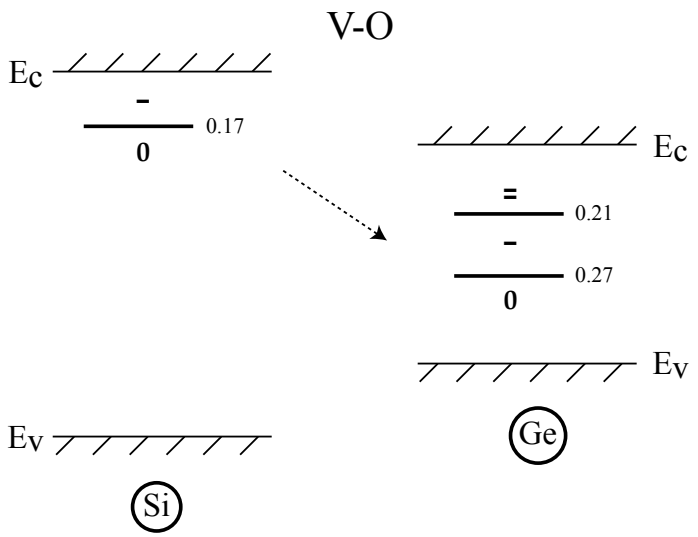

Figure 4.30: The single (acceptor) energy level of the vacancy-oxygen pair (A-center) in Si (left) and the two energy levels of the same defect in Ge (right). The dotted arrow indicates the shift of the single acceptor towards the valence band. Just as for the E-center the extra energy level in Ge is a double acceptor that has moved away from or emerged from the conduction band.

4.3.3.1 VO in MBE grown n-type

We have grown a 3 μm epitaxial MBE n-type Ge layer doped with Sb to a concentration of about $3-4\times10^{16}$ cm^{-3} to investigate MBE-grown Ge material. Schottky diodes are formed on this material as described in chapter 3. These diodes will be treated in more detail in section 4.3.4. As it has been observed in other MBE grown samples doped with Sb, oxygen comes along with this dopant, probably due to oxidation of Sb in the source.

A crude estimate based on the Sb and oxygen content in the top layer of the n^+p-diodes, grown by MBE as described in chapter 3, gives that the oxygen content is about 13% of the Sb content. Thus the oxygen content is estimated to be $3-4\times10^{15}$ cm^{-3} in the present n-type diodes. Regardless of the validity of this estimate we note that the oxygen concentration must certainly be lower than the Sb concentration, as the former is believed to be due to the presence of Sb oxide in the effusion cell.

The DLTS spectrum before as well as after irradiation is shown in figure 4.32. The emission rates as a function of temperature for the two major peaks

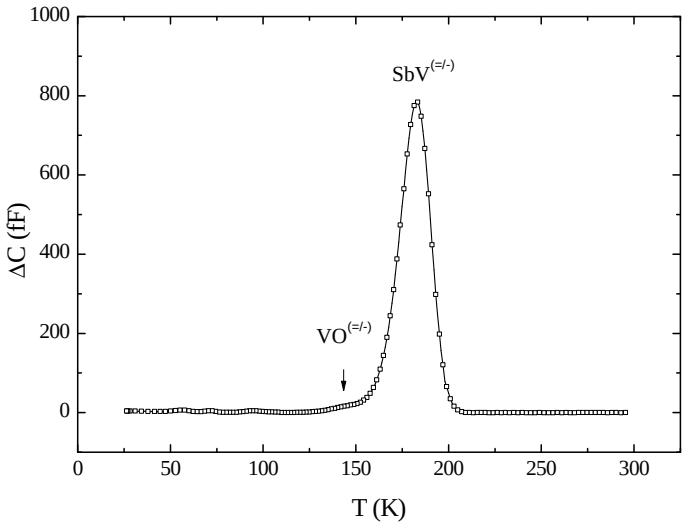

Figure 4.31: DLTS spectrum measured on an n-type Schottky diode after RT irradiation with 2 MeV electrons to a dose of 1.6×10^{14} cm^{-2}. The measurement settings were $e_n = 20$ s^{-1}, $\tau = 1$ ms, $V_r = -5$ V and $V_p = -1$ V. The arrow indicates the temperature where the A-center double acceptor would be present and does not represent an assignment of the minor feature present there. The E-center peak concentration is about 1.3×10^{14} cm^{-3}. Every other data point has been omitted for clarity.

are compared to literature values for the E- and A-center double acceptor energy levels in figure 4.33 confirming their origin. Surprisingly the VO concentration is much higher than the E-center concentration, despite the oxygen concentration being lower than the Sb concentration as remarked above. This then leads us to the interesting conclusion that the interstitial oxygen, O_i is more efficient at trapping vacancies than the positively charged Sb atoms. In addition this explains why there is no sign at all of the E-center in the spectra presented in [Markevich 2002] even though the diodes are doped with Sb.

4.3.3.2 VO in p-type

Previously DLTS spectra recorded on a n^+p mesa diode, after 2 MeV electron irradiation at RT, were shown in figure 4.15. Focusing now on the last peak labeled H330, we note that the position in temperature is in fact very close to the position that would be predicted for the VO level found by MCTS in [Markevich 2002].

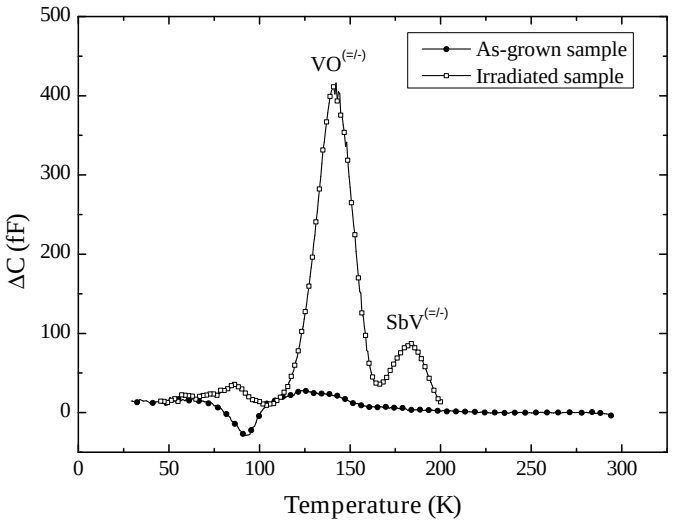

Figure 4.32: DLTS spectrum (filled circles) from an as-grown MBE n-type Ge diode (e_n = 20 s^{-1}, τ = 1 ms, V_r = −5 V and V_p = 0 V). DLTS spectrum (open squares) from a MBE diode irradiated at 200 K with 2 MeV electrons to a dose of 1.6×10^{14} cm^{-2} (e_n = 20 s^{-1}, τ = 1 ms, V_r = −2 V and V_p = −0.2 V). Only every third data point is shown for clarity.

Figure 4.34 shows a comparison of the emission rate found for the H330 peak with the emission rate found for $VO^{(-/0)}$ by MCTS in [Markevich 2002] demonstrating that they match very well. Referring to figure 4.15 again we note that H330 is stronger compared to the other prominent peaks H140 and H190 in the region closer to the junction. This is an indication then that H330 is enhanced towards the junction. In fact as mentioned above the concentration of oxygen is rather low in the CZ-Ge which is what the p-type part of the diode is made from. There is however a relatively high content of oxygen in the MBE n^+ top layer, and the n^+p structure is annealed during the growth (cf chapter 3). The diffusion parameters of oxygen in Ge has been estimated by [Corbett 1964] from the studies of the annealing of an infrared band related to oxygen. Using these parameters (D_0 = 0.40 cm^2/s, Q = 2.076 eV) and the annealing details (10 minutes at 750°C) gives a diffusion length of about 1.4 μm. Given the approximate nature of these diffusion parameters it is then certainly plausible that oxygen has diffused far enough into the CZ-Ge to allow the formation of the A-center at detectable concentrations.

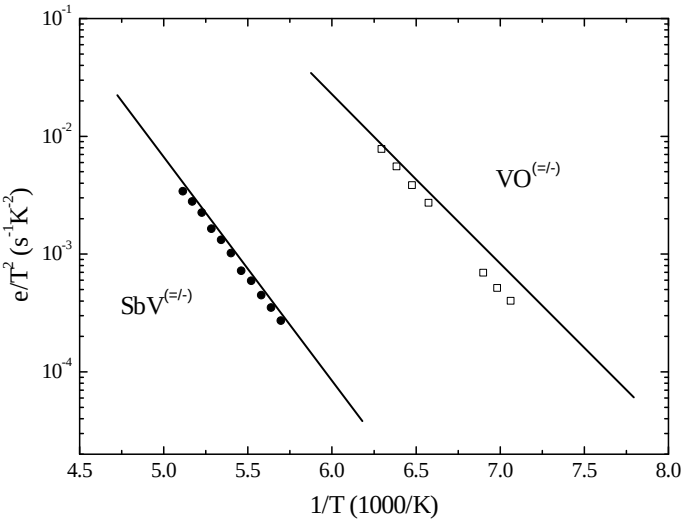

Figure 4.33: Comparison of Laplace DLTS measurement of the emission rates of the two peaks shown in figure 4.32 with literature values (solid lines) for the E-center [Fage-Pedersen 2000] and A-center [Markevich 2002] double acceptors. The agreement is satisfactory enough to conclude that the two DLTS lines are indeed due to the E- and A-center.

The annealing temperature found by isochronal annealing with 20 minutes duration every 10 K, is about 380 K. This should be compared to the annealing temperature from [Markevich 2002] which is not listed but can be estimated to be around 410 K from the shown annealing curve with 30 minutes duration and 20 K steps. The steps are not the same and the results are thus not directly comparable. We may however note that the Sb E-center showed a similar tendency when comparing annealing temperatures from n-type (30 minutes duration and 20 K steps [Markevich 2004b]) with those from p-type (20 minutes duration and 10 K steps [Lindberg 2005]). In n-type the value was around 430 K [Markevich 2004b] while in p-type it was found to be 385 K [Lindberg 2005]. According to the authors, this is attributed to the different charge states that the defect anneal in. The same is then likely the case for the annealing of VO. In conclusion H330 is assigned to the A-center single acceptor, $VO^{-/0}$, formed by association of vacancies with oxygen that has diffused in from the top layer.

The detection of the VO single acceptor as a majority carrier trap in p-type

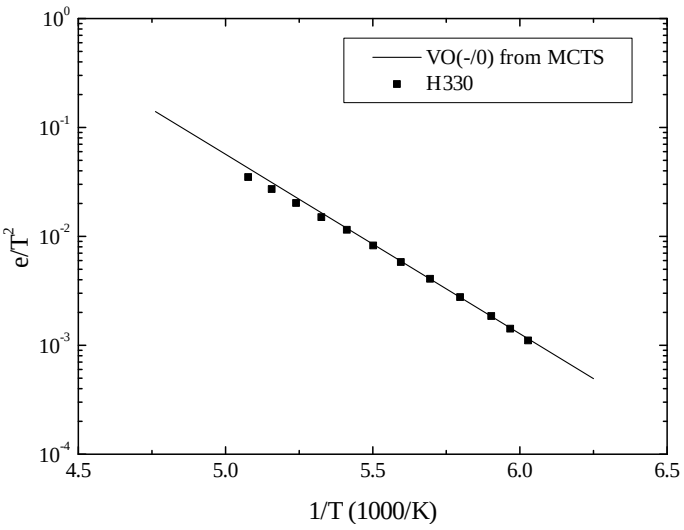

Figure 4.34: An Arrhenius plot comparing the emission characteristics of the A-center single acceptor level, $VO^{(-/0)}$ measured by MCTS (solid line) in n-type Ge [Markevich 2002] with those of H330 measured by Laplace DLTS in p-type Ge (open squares).

allows the determination of the capture cross section directly by varying the width of the filling pulse. This is not possible, or at least very complicated, by MCTS. Figure 4.35 shows the capture cross section as a function of temperature in an Arrhenius plot demonstrating that there is a barrier for capture. It was in fact speculated by the authors of [Markevich 2002] that such a barrier and/or an entropy difference between the states existed. This was due to a discrepancy between the activation energy found by Hall measurements ($\Delta G_{\mathrm{p}} = 0.27$ eV) and DLTS. The presence of such a barrier has thus been confirmed but does not account for the full difference since (cf equation (2.13)) $\Delta H_{\mathrm{p}} = E_{\mathrm{pa}} - \Delta E_{\mathrm{p}\sigma} \approx 0.30$ eV. Although the uncertainties on σ_{pa} and $\sigma_{\mathrm{p}\infty}$ are large in nature it is apparent that they differ by several orders of magnitude and hole emission is therefore accompanied by an entropy change, $\Delta S_{\mathrm{p}} \approx 5k_{\mathrm{B}}$. This entropy change has been estimated from equation (2.13) and implies that $\Delta G_{\mathrm{p}} \approx 0.3\,\mathrm{eV} - 5k_{\mathrm{B}}T$ which could account for the lower energy measured by Hall effect measurements.

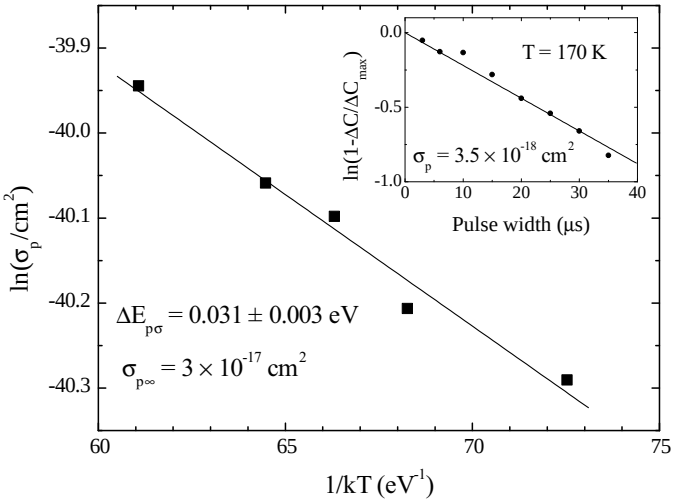

Figure 4.35: The measured capture cross section for capture of a hole on the neutral VO defect as a function of temperature, showing that there is an energy barrier for capture. The inset demonstrates the measurement of the capture cross section at 170 K by varying the filling pulse duration.

4.3.4 Carbon related defects

The solubility of carbon in Ge is very low and an upper limit for the typical carbon content in CZ-grown Ge can be set at 6×10^{12} cm^{-3} based[17] on [Haller 1982]. For comparison CZ-grown Si crystals can contain carbon concentrations on the order of 10^{18} cm^{-3} [Bean 1971]. In a CZ-Ge crystal carbon related defects can therefore be expected to be present at much lower concentrations than in a similar CZ-Si crystal.

On the other hand it has recently been shown that high concentrations of carbon, on the order of 10^{20} cm^{-3}, can be used to strongly retard the diffusion of group-V elements in Ge [Brotzmann 2008a]. This makes carbon technologically interesting in the context of device engineering. However, given the large concentrations of carbon required it is important to know the stability and electronic properties of defects involving carbon. These might arise as a consequence of processing steps such as ion implantation. While the car-

[17] This is the carbon concentration found in a carbon doped Ge crystal that has been regrown in a quartz crucible.

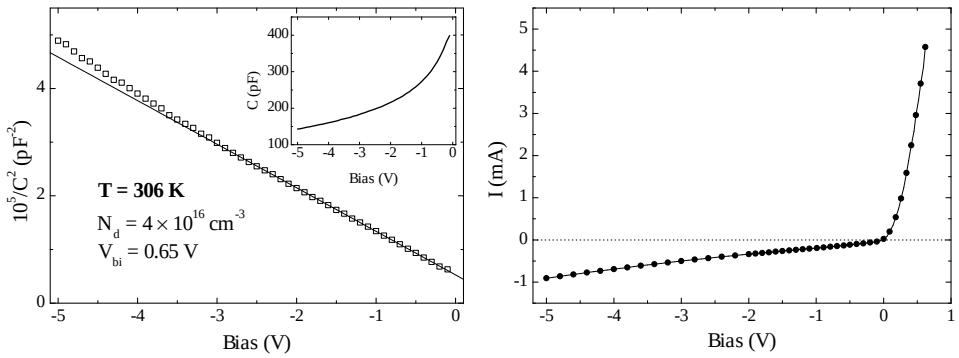

Figure 4.36: The C-V (left) and I-V (right) characteristics of a Schottky diode made from MBE grown Sb doped n-type Ge. The measured C-V is shown in the inset on the left graph while the main graph shows $1/C^2$ which is theoretically a straight line (cf (2.20)). From a straight line fit on the interval -3 V to 0 V the donor concentration can be estimated (diode area 0.52 mm^2) to $N_d = 4 \times 10^{16}$ cm^{-3}.

bon concentration mentioned is much higher than the solid solubility, MBE allows the growth of meta-stable structures with a substitutional carbon content of several percent [D'Arcy-Gall 2001] due to the surface solubility being higher.

Motivated by this we attempted to prepare n-type Ge, Au contact Schottky diodes by the procedure outlined in section 3.2 on MBE grown epitaxial Ge doped with Sb. From the analysis of the top layer on n^+p mesa-diodes the carbon content is known to be about 6×10^{16} cm^{-3} (cf figure 3.3). The result of optimizing the MBE growth procedure to obtain optimal diodes is shown in figure 4.36 where the C-V and I-V characteristics of such a diode is shown.

These diodes were irradiated with 2 MeV electrons and a DLTS spectrum resulting from this has already been presented in connection with the A-center in Ge, figure 4.32. In figure 4.37 the DLTS spectrum resulting after keeping the diode at RT for a few days following electron irradiation is shown. All of the peaks present has been observed previously after electron irradiation of Schottky diodes on CZ-grown Ge [Fage-Pedersen 2000]. There is thus no sign of any stable carbon related defects with energy levels in the upper part of the bandgap.

Low temperature irradiations and subsequent annealing at progressively higher temperatures were carried out as well, but that did not result in any

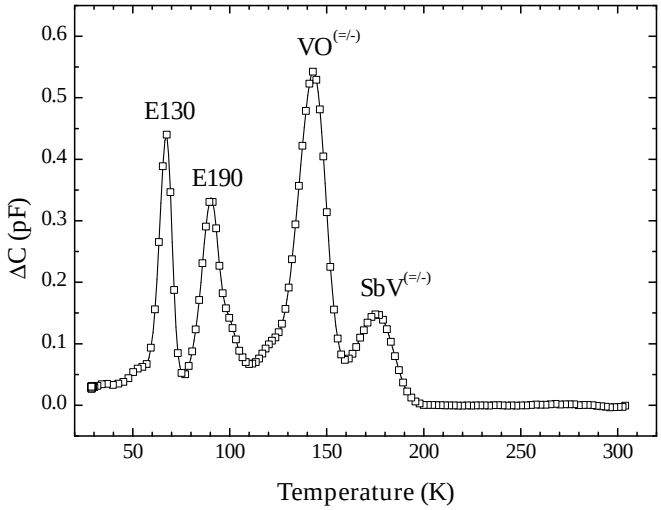

Figure 4.37: DLTS spectrum recorded on a Schottky MBE n-type Ge diode after annealing at RT for a few days after 2 MeV electron irradiation to a dose of 1.2×10^{14} cm^2. DLTS parameters were $e_p = 10$ s^{-1}, $\tau = 1$ ms, $V_r = -5$ V and $V_p = 0$ V. The emission characteristics of the peaks labeled E130 and E190 match those of the similarly named peaks in [Fage-Pedersen 2000].

new DLTS peaks either. Figure 4.38 shows a DLTS spectrum recorded after electron irradiation at 28 K all the way up to RT where all peaks have been seen before in CZ-Ge. One interesting point can be deduced from this low temperature irradiation, namely that the VO double acceptor peak is present on the way up in temperature, meaning that the vacancy, likely in the double or triple negative charge state, has become mobile at a temperature below 140 K.

This null result regarding carbon related defects in the upper part of the bandgap could in a way have been anticipated. A DLTS investigation of carbon related defects in $Si_{1-x}Ge_x$ [Pedersen 1999] has shown that the single acceptor energy levels of the carbon interstitial defect, C_i, and the C_iC_s pair move down in the band gap with increasing Ge content. Extrapolating the results of these authors gives the indication that these acceptor levels will end up in the lower part of the bandgap in pure Ge. Thus p-type Ge diodes are required for the detection of energy levels of these defects unless a double acceptor level emerges from the conduction band. In the present work, no sign

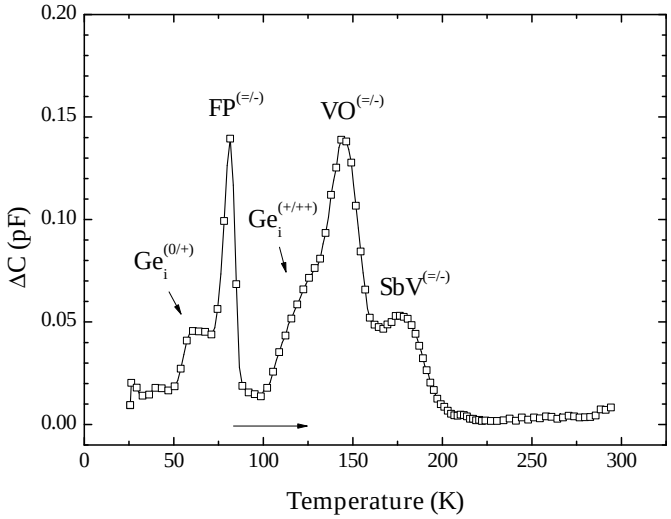

Figure 4.38: DLTS spectrum recorded on the way up in temperature after 2 MeV electron irradiation at 28 K to a dose of 1.6×10^{13} cm^2. Measurement settings were $e_p = 20$ s^{-1}, $\tau = 1$ ms, $V_r = -4.5$ V and $V_p = 0$ V. The peaks are labeled according to the attributions made in section 4.1.

of such a level has been seen.

Additionally this experiment proves that usable n-type Ge diodes can be made from MBE grown samples opening up the possibility of studying Ge MBE structures by DLTS. This includes samples simply doped by any element that can be introduced by MBE; the oxygen content however is unwanted and might be avoidable by using phosphorus or arsenic as the donor species. As it was mentioned previously it was attempted, although unsuccessfully, to study Ga in n-type Ge in this manner.

4.4 Summary

Electronically active defects in Ge were investigated with DLTS using n-type Schottky diodes and p-type n^+p mesa diodes subjected to different kinds of irradiation. *In situ* DLTS measurements in p-type after low temperature electron irradiation revealed a hole trap, which is attributed to the single acceptor state of the vacancy. Indirect evidence of the vacancy was seen in n-type as well. Along with the vacancy peak another peak, behaving in several respects

Label	Level	E_a (eV)	σ_a (cm^2)	ΔH (eV)	σ (cm^2)
X	$V^{(-/0)}$	$E_v + 0.124$	1.0×10^{-15}	0.128	
Y	$Ga_i^{(0/+)}$	$E_v + 0.65$	3.0×10^{-13}	0.34	$10^{-13} \times \exp(-0.32\text{eV}/k_B T)$
Z	$Ga_i^{(-/0)}$	$\sim E_c - 0.3$	$10^{-17} - 10^{-16}$		
FP	$(\text{V-Ge}_i)^{=/0}$	$\sim E_c - 0.14$	$\sim 5 \times 10^{-16}$		
A	$Ge_i^{(0/+)}$	$E_c - 0.08$	2.9×10^{-17}		
B	$Ge_i^{(+/++)}$	$E_c - 0.24$	1.8×10^{-16}		

Table 4.1: Summary of the energy levels that are not stable with bias off at RT, observed by *in situ* DLTS measurements. The values for ΔH are corrected for field dependence and barrier for capture except when the capture cross section was too high to measure ($V^{-/0}$).

like the boron interstitial in Si, was attributed to the Ga interstitial defect. A level coupled to this was seen by forward bias and optical MCTS. Investigation of this defect in n-type was attempted using MBE grown samples; this was however in vain. The equivalent *in situ* experiment in n-type resulted in the appearance of an unstable peak, which in several ways fits earlier observations of the Frenkel pair (FP) defect. In addition two coupled levels were observed that fit theoretical predictions of energy levels of the self-interstitial. These results are shown in table 4.1. A thorough search was carried out for energy levels related to the di-vacancy, using both n- and p-type diodes, and irradiating with electrons, protons and alpha particles. No energy levels that could be attributed to the di-vacancy was found in the upper part of the band gap. However, a vacancy-complex forming as a secondary defect in alpha irradiated samples was observed A similar defect has been observed in implantation damage by others [Auret 2006, Peaker 2005]. One of the peaks seen in p-type after RT electron irradiation was ruled out as a candidate, since it could be attributed to the single acceptor of the A-center. A combination of low temperature electron irradiations and proton irradiations indicated that two of the remaining peaks were linked through the addition of a vacancy. This was used to tentatively assign these peaks to energy levels of the di-vacancy and tri-vacancy. Additionally a lower annealing temperature of V_2 than expected

Label	Level	E_a (eV)	σ_a (cm^2)	ΔH (eV)	σ (cm^2)
E290	V-complex	$E_c - 0.286$	8×10^{-14}		3×10^{-16}
H330	$VO^{(-/0)}$	$E_v + 0.332$	1.4×10^{-14}	0.301	$3 \cdot 10^{-17} \times \exp(-0.031\text{eV}/k_B T)$
H80	$V_3^{(-/0)}$	$E_v + 0.076$	6×10^{-14}	0.091	3.6×10^{-15}
H140	I_2	$E_v + 0.138$	1.2×10^{-14}	0.139	$4.2 \cdot 10^{-15} \times \exp(-0.0029\text{eV}/k_B T)$
H190	$V_2^{(=/0)}$	$E_v + 0.186$	5×10^{-15}		
H320		$E_v + 0.324$	2×10^{-15}		

Table 4.2: Summary of the energy levels stable at RT, observed by DLTS measurements. The values for ΔH are corrected for field dependence and barrier for capture.

from other studies was observed. It was suggested that V_2 is annealing due to annihilation caused by the di-interstitial defect, I_2, also observed by DLTS. These investigated energy levels, that are stable at RT, are shown in table 4.2.

Finally MBE grown material was used to make Schottky diodes with the purpose of investigating carbon in Ge. No new energy levels were found after electron irradiation, and the preliminary conclusion is that carbon related defects are not active in the upper part of the bandgap.

CHAPTER 5

Atomic diffusion

Contents

The diffusion of the semiconductor atoms themselves is called *self-diffusion* and gives valuable information about the mechanisms of diffusion. In Ge it has been firmly established that the self-diffusion is mediated entirely by vacancies [Werner 1985, Vogel 1983] with a single activation energy over a very broad temperature range [Hüger 2008]; 429°C to 904°C. This is in sharp contrast to Si where at high temperature the self-diffusion is dominated by a self-interstitial mechanism [Bracht 1998] while at lower temperatures (less than about 850°C) vacancy mediated diffusion dominates [Shimizu 2007].

Evidently the interstitial diffusion mechanisms are suppressed in Ge either due to a high formation energy of self-interstitials, making the concentration too low to play a role, or due to a high barrier for migration of interstitial type defects. In fact both formation and migration energies of the self-interstitial are calculated to be higher than those of the vacancy in Ge [Vanhellemont 2007]; the former about 0.4-1 eV higher and the latter 0.4-0.5 eV.

Experimentally self-interstitials [Haesslein 1998] and gallium-interstitials (cf section 4.3.2) are seen to be very mobile at RT, so it is plausible that the suppression is due to a low concentration of self-interstitials.

Diffusion in Ge, impurity- as well as self-diffusion, has been studied by a number of different methods. The studies are generally based on one of three setups: 1) in-diffusion of an element deposited on the surface of the crystal, 2) diffusion of an implanted impurity profile or 3) diffusion of buried layers. The possible disadvantage of 1) is that the point defect concentration is most likely different from the bulk value, which can make the simulation complicated. Implantation causes radiation damage which can in turn lead to transient enhanced diffusion [Jain 2002] complicating method 2). On the other hand the samples for 3), which are usually grown by MBE, can be limited by difficulty of incorporating the impurity. This limitation is basically absent for 2) in which case the peak concentration can be very precisely controlled. 1) is mostly limited by finding a stable compound which includes the impurity and is suitable for deposition. In our case we focus entirely on 3) since we have the possibility of growing such samples in our research group. Also this method has been used very little, if at all, on Ge.

With respect to measuring the depth profile of the element in question several techniques have been used including: a) penetration depth measured by the position of a pn-junction [Dunlap 1954], b) depth profiling of a radioactive tracer from its activity [Riihimäki 2007], c) depth profiling of an electrically active impurity by measuring the carrier concentration by spreading resistance [Bracht 2006b], d) direct depth profiling by SIMS (cf section 2.2.1) and more recently e) measuring broadening of multi-layer structures by neutron reflectrometry (NR) [Hüger 2008]. The techniques a)-c) have in common that they generally require diffusion lengths substantially higher than 1 μm while in the case of d) 10-20 nm can be sufficient and e) can cope with less than 1 nm. Only d) SIMS is relevant for the present work as the samples are not suitable for long diffusion lengths.

In the following sections the experiments carried out in this work to gain more insight into the nature of the diffusion mechanisms in Ge are discussed.

5.1 Sample capping

Ge is very sensitive to oxidation and as compared to Si the impact is strengthened by the instability of the Ge oxide (GeO and GeO_2). At temperatures as

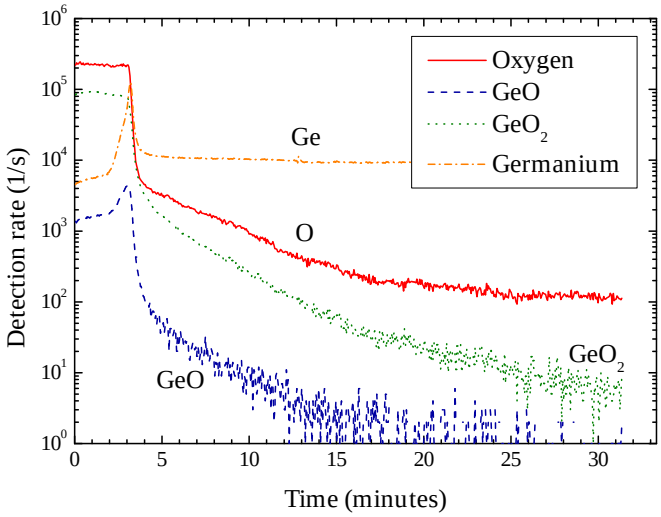

Figure 5.1: SIMS spectrum measured on a Ge sample after annealing at 570°C for 20 minutes demonstrating the oxidation near the surface. The Bi^+ current was 1.6 pA and the Cs^+ sputtering current was 11 nA at an energy of 1 keV.

low as 400°C the oxide transforms from the more stable GeO_2 form to the volatile GeO, strongly desorbing already at 500°C [Molle 2006].

At annealing temperatures above about 550°C we observe visually that the samples are strongly oxidized despite being annealed in a flow of high purity nitrogen, unless the annealing time is quite short that is. As seen in the SIMS spectrum in figure 5.1 there is a very strong oxygen signal present from a sample annealed at 570°C for 20 minutes. The GeO and GeO_2 signals demonstrate that the top of the sample has been oxidized.

Clearly no sensible information can be drawn from such a deteriorated sample. There are two relatively simple possible solutions to this problem. The first one is to encapsulate the sample in an evacuated ampoule that is subsequently filled with an inert gas as for example argon. This method was employed in the study of Si diffusion in Ge [Silvestri 2006].

It should be noted however that annealing at higher temperatures (650–700°C) does not lead to visual oxidation. This is probably due to the volatile GeO form being dominant at higher temperatures.

The choice in the present work was to use vacuum annealing (cf section 3.6), which will certainly lower the oxygen presence by many orders of magni-

tude. This however introduced another possible issue namely that of surface evaporation. As demonstrated in figure 5.2 there is an indication of possible evaporation from the surface at higher temperatures. The buried Si spike has moved closer to the surface (20-30 nm in the presented case). Not only does this complicate the analysis but could lead to injection of point defects from the surface. This is entirely unwanted and must be avoided.

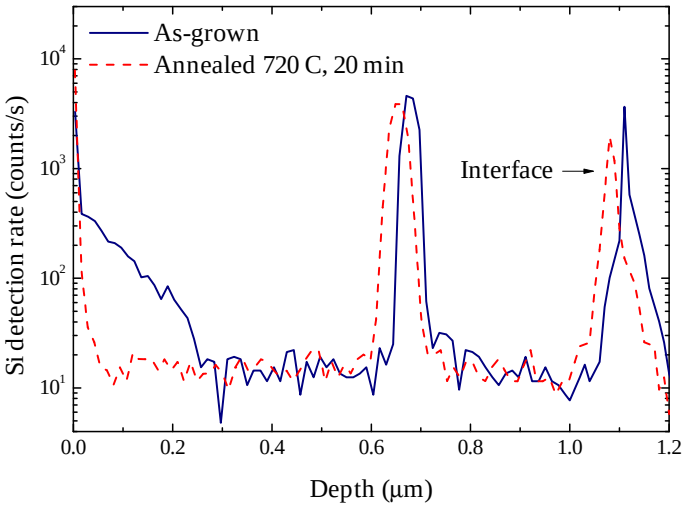

Figure 5.2: ToF SIMS spectra showing the concentration profile of Si in samples containing a buried Si spike. The solid line shows the profile before annealing of the sample while the dashed line demonstrates the effect of annealing at 720°C for 20 minutes. It is clearly seen that the buried spike appears to have moved 20-30 nm closer to the surface, possibly due to evaporation. These SIMS spectra were recorded on a Cameca 7f SIMS instrument at the University in Oslo thanks to the help of Jens S. Christensen. The primary ion was O_2^+ at a current of ~115 nA with an energy of 10 keV.

To prevent the evaporation from the samples the application of a capping layer is a natural choice. Using a magnetron sputtering equipment from AJA, 100-130 nm of SiO_2 was deposited on the samples prior to annealing. This technique brings the risk of injection of point defects due to reactions at the interface between Ge and SiO^2. To test if the oxide has an influence on the intrinsic diffusion, a sample with a buried Si spike was annealed with the capping layer on top. Figure 5.3 shows the resulting SIMS measurement done

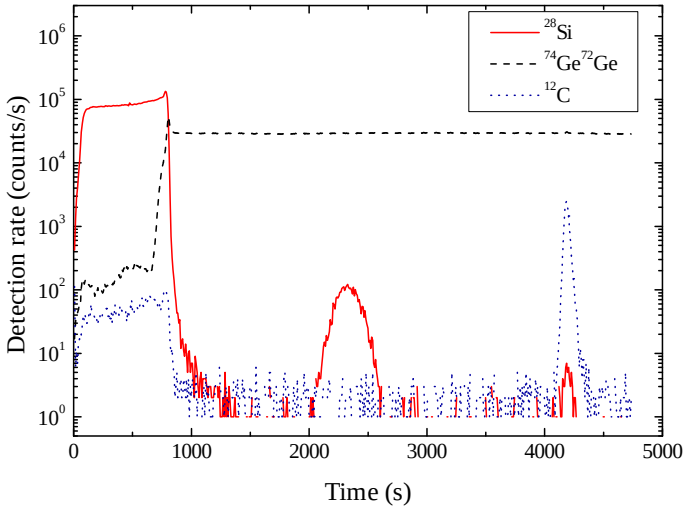

Figure 5.3: The raw SIMS measurement of Si in a sample containing a buried Si spike after annealing at 720°C for 30 minutes in a nitrogen flow. The SiO_2 cap is present on top of the sample and seen by a very high detection rate of Si. Also shown is the matrix signal from the $^{72}Ge^{74}Ge$ molecule and the carbon signal clearly showing the location of the interface to the original crystal. The Bi^+ current was 1.4 pA and the Cs^+ sputtering current was 24 nA at an energy of 3 keV.

by ToF SIMS. The resulting depth and concentration calibrated depth profile of Si is shown in figure 5.4 along with the simulated profile using the diffusion coefficient obtained from the results of [Silvestri 2006].

The agreement between simulation and measurement is very good and it is thus concluded that the capping layer does not affect the diffusion and can be used in further experiments. Using a SiO_2 capping layer has the advantage that the capping layer can easily be completely removed by etching with a 10% HF solution for some minutes without affecting the Ge part notably.

5.1.1 Diffusion into the cap layer

Before realizing that the temperature reading of the vacuum furnace was wrong (as described in chapter 3) a series of annealing experiments were carried out. This resulted in much stronger diffusion than expected and despite the buffer layer of Ge on top of the buried layer the diffusion went all the way to the interface with the cap layer. The SIMS measurements were done on the Cameca

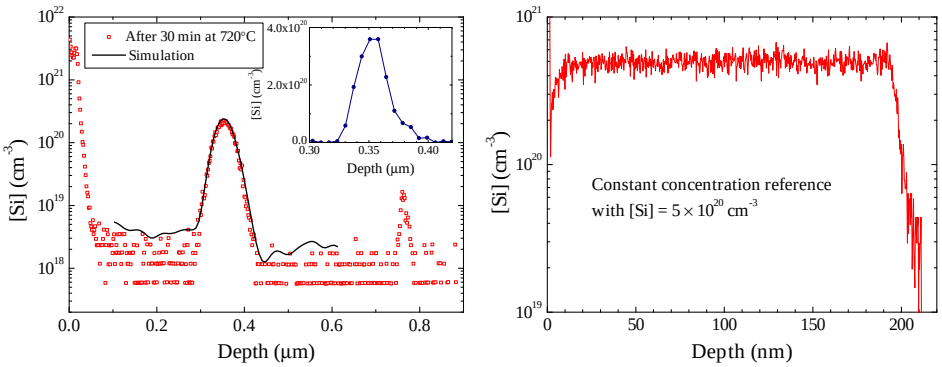

Figure 5.4: The concentration and depth calibrated Si profile below the oxide (left) from figure 5.3, a simulation of the annealing process based on the diffusion parameters from [Silvestri 2006], and the initial Si profile shown in the inset. The right hand side graph shows the reference sample used for converting detection rate into concentration for Si.

4f instrument at KTH in Stockholm, Sweden, which requires the sample to be conducting to avoid charging and thus the oxide was etched off using HF before measurements.

Because of this the presence of diffused impurities in the cap was not observed directly. However it was clearly visible from the measured profiles that there had been a loss of atoms to the cap layer. Only by introducing this in the form of δ in (2.68) as described in chapter 2 could the diffusion be satisfactory simulated. The actual value of δ to get the best fit between simulation and experimental profile however varied between 0.06 - 0.20 for samples with different annealing temperatures without a clear trend.

Also the actual annealing temperature is impossible to reconstruct since it was later found that it took very long time to stabilize with the improper thermocouple position. The conclusion is thus that δ is merely a construct to take into account loss and it should really be avoided having substantial diffusion all the way to the surface. For one of the annealing temperatures a sample without the SiO_2 cap was included for comparison. As shown in figure 5.5 the result of simulation was in fact that the diffusion coefficients found for the capped and uncapped sample agreed within 7%. So in this case the influence of evaporation on the diffusion is quite weak if any. Meanwhile the required value of δ was more than twice as high for the uncapped sample

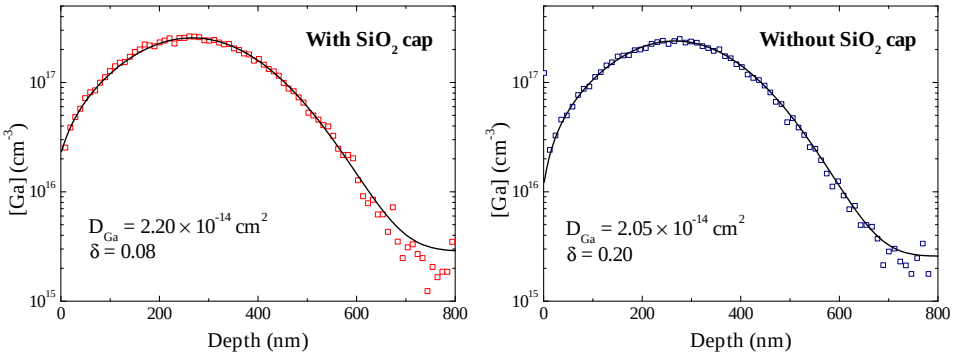

Figure 5.5: Diffusion of Ga in Ge at an unknown temperature (likely around 750°C) with a SiO_2 cap (left) and without (right). The O_2^+ current was ~120 nA at an energy of 10 keV.

which might be related to the evaporation from the surface. Due to the very broad impurity profile as a result of a higher temperature than expected the sample evaporation is not very evident here. Nevertheless it is definitely not satisfactory to have to include the δ parameter which emphasises the need to keep the diffusion away from the interface.

5.2 Donor diffusion

The donor impurities phosphorus (P), arsenic (As) and antimony (Sb) have been the subject of recent diffusion investigations in Ge [Brotzmann 2008b]. The conclusion, based on the observation of extrinsic diffusion, was that diffusion is mediated by a vacancy mechanism giving $D_X = D_X^i \cdot (n/n_i)^2$. This implies that double negative vacancies or single negative[1] vacancy-donor pairs govern the diffusion.

If the square dependence on carrier concentration is solely due to $(X-V)^-$ pairs it is surprising that there appears to be no contribution from $(X-V)^=$ since the single and double acceptor levels of the E-center are not far apart in the band gap (cf 4.3.1). This then leads to the speculation that the square dependence of D_X on n is due to the double negative vacancy, and that a triple

[1]Since 2 electrons are needed to convert a positively charged ionized donor atom plus a neutral vacancy into a single negative XV pair.

negative vacancy does not exist (contrary to theoretical predictions , cf 4.1.1) or does not contribute. However Brotzmann *et al*. used n_i as a fitting parameter and it has recently been suggested [Canneaux 2009] that fixing instead n_i at the value established in the literature [Morin 1954] leads to the necessity of the inclusion of a $(n/n_\mathrm{i})^3$ term in D_X. Thus an E-center mechanism for the diffusion would be consistent.

Both the experiments by Brotzmann *et al*. and those by Canneaux *et al*. involved diffusion very close to the surface. The study of the diffusion of a buried spike of a donor impurity is thus still of interest. We have chosen to investigate the diffusion of As in this manner. For this purpose a sample with the depth profile shown on the left hand side in figure 5.6 was grown by MBE. On the right hand side of the same figure is shown the depth profile of the implant of $6{\times}10^{14}$ cm^{-2} ^{75}As which serves as a concentration reference. Unfortunately the concentration of the As spike was higher than planned so extrinsic diffusion will not be avoidable. In particular the influence at temperatures around 500°C should be very strong as $n_\mathrm{i} \approx 10^{18}$ cm^2 at this temperature (cf figure 2.2).

SIMS measurements on As were done at the Cameca 4f equipment at KTH in Sweden. The molecule ^{76}Ge-^{75}75 was used as the marker for As to suppress the mass interference of ^{75}As with ^{74}Ge-H. Cs^+ is used as the primary ion since As yields very few negative ions.

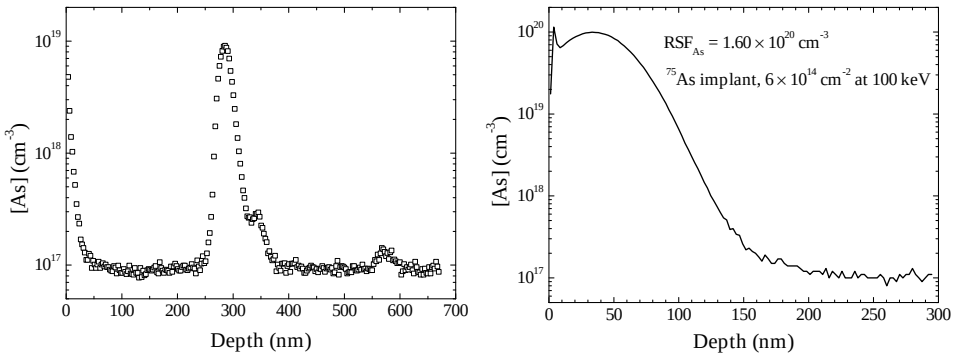

Figure 5.6: The depth profile of As measured by SIMS in a MBE grown sample designed to study As diffusion (left) and a sample implanted with As to serve as a concentration reference (right). The Cs^+ current was ~220 nA at an energy of 9 keV.

5.2.1 The effect on diffusion of surface oxidation

As shown above it is known that annealing in the flow furnace under nitrogen flow is associated with oxidation. To study the influence of oxidation on the diffusion the samples shown in figure 5.6 were annealed with and without a SiO_2 cap. Figure 5.7 demonstrates the results for annealing at 470°C and 510°C. There is a striking difference between annealing with and without the cap as the diffusion is clearly much stronger without the capping layer.

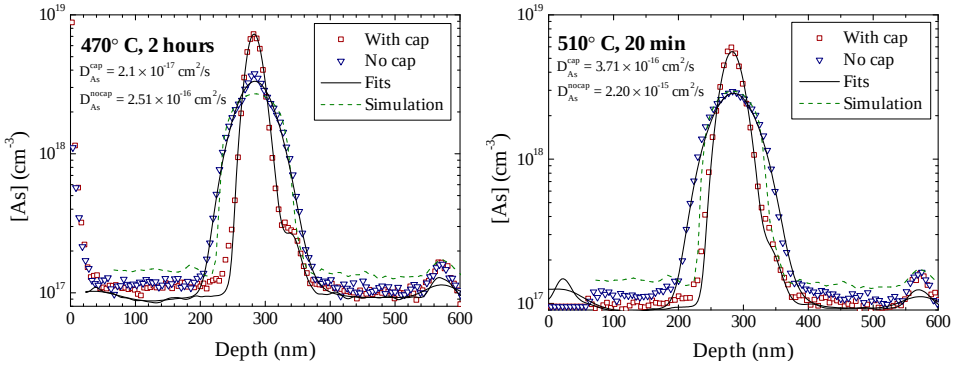

Figure 5.7: SIMS depth profiles showing the result of annealing at 470°C (left) and 510°C (right) in the flow furnace both with and without an SiO_2 capping layer. The Cs^+ current was ~220 nA at an energy of 9 keV.

In the case of the capped samples (shown by red open squares) the diffusion can be fitted very well through simulation using the simple concentration independent model of the diffusion coefficient, $D_{As}(n) = D^i_{As}$. On the other hand the As concentration is substantially above n_i, so the effect of the field factor h in (2.64) should be included. With this taken into account the diffusion can still be described well by simulation, as shown by the solid line fit following the red open squares, however with a lower D^i_{As}. The values found and indicated on the figures are 2-4 times higher than the values calculated from the parameters found by [Brotzmann 2008b]. This apparent concentration independent D_{As} is puzzling since the As concentration is well above $n_i(510°C) = 1.2 \times 10^{18}$ cm^{-3} over a broad depth range. The simulation according to the extrinsic form of the diffusion coefficient found by Brotzmann *et al.* is shown by the dashed green line in the figure. It is very evident that the extrinsic diffusion predicted by simulation would be much stronger than

what is observed. Furthermore the characteristic flat non-Gaussian shape of the simulated profile resulting from extrinsic diffusion is not at all present in the measured profile. To explain this unexpected observation of a concentration independent diffusion one could suppose that the oxidation at the back of the sample, despite being around 500 μm away, is causing a vacancy supersaturation.

Turning now to the samples annealed without a capping layer (blue open triangles in the figure), the diffusion does actually resemble the extrinsic diffusion slightly. However the characteristic flat shape of the peak after extrinsic diffusion is not present in the measured concentration profile. In fact, as shown by the solid black line following the data points, the diffusion without a capping layer can again be fitted by the same concentration independent model as above, but with a different value of D^{i}_{As}. Furthermore the profile can in this case not be accurately reproduced unless h in (2.64) is included. Note that there appears to be an immobile fraction of As in the peak at 470°C. This could be simply due to As clustering, but it is probable that oxygen is also playing a role being an efficient trap for vacancies (cf section 4.3.3).

Based on these observations it can be concluded that oxidation is injecting vacancies; the injection of self-interstitials should retard the diffusion more when the capping layer is not there[2]. This is opposite to Si where oxidation has been determined to lead to self-interstitial injection [Antoniadis 1982]. The experiment could in principle be repeated at more different temperatures as well as annealing times to investigate the influence of oxidation in detail. In any case the effect of oxidation is seen to strongly effect the diffusion of As.

Annealing experiments on As diffusion were carried out using the vacuum furnace as well to avoid the influence of oxidation. All samples were covered with 130 nm of SiO_2 during annealing. Figure 5.8 shows the lowest temperature annealing (open red squares) carried out at 510°C for 18.5 hours. In order to investigate if a concentration independent diffusion coefficient can describe the diffusion, a least squares fit was done resulting in the black solid line ($D^{i}_{As} = 1.27 \times 10^{-15}$ cm^2/s); the field factor h was however included. This is seen not to reproduce the profile shape accurately; the diffused profile is

[2]The concentration of injected point defects can be expected to decrease with the distance from the surface.

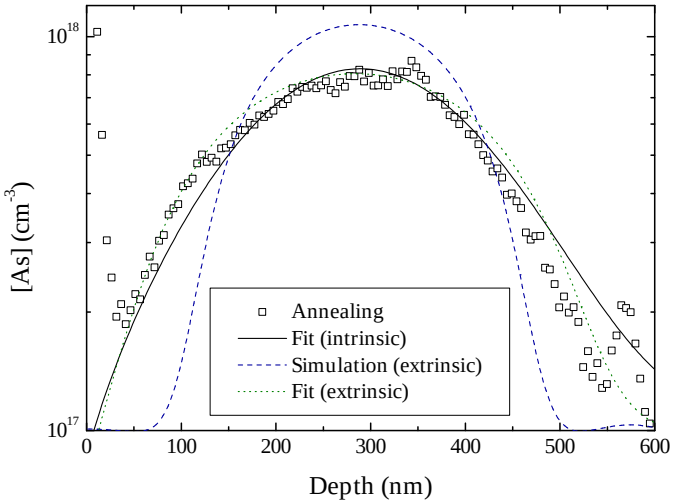

Figure 5.8: Depth profile of As measured by SIMS after annealing in vacuum at 510°C for 18.5 hours (open red squares). The least squares fit using concentration independent (intrinsic) diffusion is shown by the black solid line. The diffusion predicted by the parameters from [Brotzmann 2008b] taking into account extrinsic diffusion, $D_{\mathrm{As}}(n) = D^{\mathrm{i}}_{\mathrm{As}} \cdot (n/n_{\mathrm{i}})^2$ is shown by the blue dashed line. Finally a least squares fit using this extrinsic model is shown by the green dotted line. See the text for parameter values. The Cs^+ current was ~75 nA at an energy of 9 keV.

more flat near the maximum indicative of extrinsic diffusion.

Using the parameters determined by [Brotzmann 2008b][3] the blue dashed line shows a simulation of extrinsic diffusion by the model mentioned previously. A larger diffusion coefficient is clearly required to describe the measured profile which is demonstrated by a least squares fit incorporating the extrinsic diffusion shown by the green dotted line yielding $D^{\mathrm{i}}_{\mathrm{As}} = 3.11 \times 10^{-16}$ cm^2/s. This fit reproduces the profile shape well, although there is some deviation which could indicate an insufficient model. Note also that the immobile fraction of As around 350 nm, similar to that seen in the as-grown sample (cf figure 5.6), is not taken into account by the simulation which will cause some deviation. This fraction is present due to a problem with the As effusion cell shutter during MBE growth, which introduced some C as well as As in the sample. As mentioned in section 4.3.4, carbon has been clearly seen

[3] $D^{\mathrm{i}}_{\mathrm{As}}(510\ \mathrm{K}) = 1.15 \times 10^{-16}$ cm^2/s

to be lead to the strong trapping of donor atoms, so there is nothing abnormal about this immobile fraction of As.

The value of D^{i}_{As} determined by fitting is higher by almost a factor of three relative to the value extracted from the parameters found by Brotzmann *et al*. which is definitely significant. In total 5 different temperature annealing experiments were carried out ranging from 510°C to 590°C in 20 degree steps. It should be noted that, except at the lowest temperature, it has been observed that the samples have small voids with a diameter of around[4] 10 nm. These voids have probably formed by vacancy agglomeration during the rapid cooling from the diffusion temperature and it could thus be expected that they did not affect the diffusion substantially.

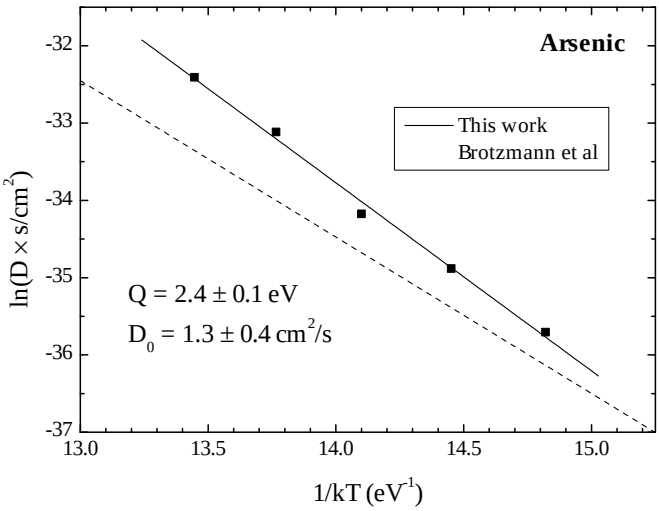

Figure 5.9: Arrhenius plot of the As intrinsic diffusion coefficient extracted by modeling the extrinsic diffusion coefficient as $D_{As}(n) = D^{i}_{As} \cdot (n/n_i)^2$. The solid line is a linear fit showing that the intrinsic diffusion coefficient follows an Arrhenius expression. The dashed line represents the parameters found by [Brotzmann 2008b] which does not match the values found in this work.

The values of D^{i}_{As} extracted by the same least squares minimization procedure as above, taking into account extrinsic diffusion, fit a Boltzmann expression nicely as shown by the Arrhenius type plot in figure 5.9. The parameters

[4]Except at 530°C where the diameter was ten times larger and it was not possible to avoid voids inside the SIMS crater.

found by Brotzmann *et al.* is represented by the dashed line which does not match the extracted values. The results of the remaining four annealing experiments, including the resulting least squares fit (solid lines), are shown in figure 5.10 for reference.

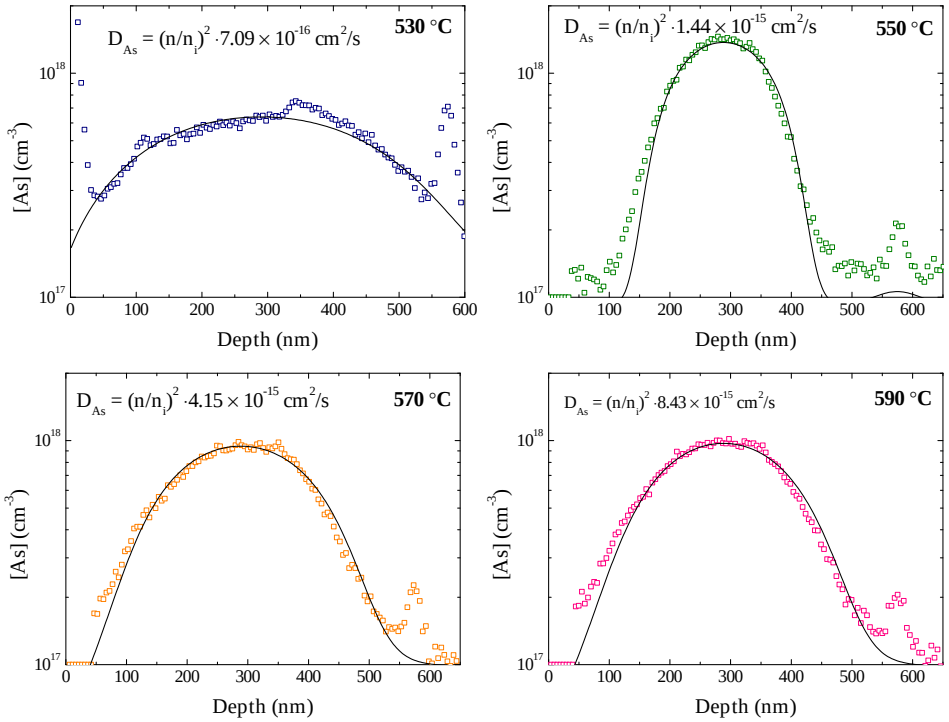

Figure 5.10: As depth profiles, measured by SIMS (open symbols), and the result of a least squares fit (solid lines). All simulations used $\delta = 0.05$ and the model $D_{\mathrm{As}}(n) = D^{\mathrm{i}}_{\mathrm{As}} \cdot (n/n_{\mathrm{i}})^2$. The Cs^+ current was ~75 nA at an energy of 9 keV.

It appears thus that the diffusional broadening of a buried layer of As in Ge gives results different from those obtained by [Brotzmann 2008b] studying in-diffusion of As from the surface. In order to elaborate on the disagreement the present experiment should be redone with a lower concentration As spike to investigate intrinsic diffusion directly, as it was done by Brotzmann *et al.* Also it would be of interest to redo the above experiment with at least 4 times lower diffusion times as the diffusional broadening was not really intended to be that high. This would also make the extrinsic diffusion more evident since the diffusion becomes intrinsic when the As concentration goes substantially

below n_i.

Perhaps a more complicated model is needed as it was suggested for P by [Canneaux 2009] (including a cubic n/n_i term in D_X), this would certainly yield a lower value of D^i_{As} if it could fit the data. Determining the intrinsic diffusion coefficient directly, as opposed to through a model for extrinsic diffusion, would tell if a quadratic term is sufficient.

5.3 Acceptor diffusion

Acceptor atoms (boron - B, aluminum - Al, gallium - Ga and indium - In) are negatively charged in Ge unless the temperature is extremely low (below 20 K). Since vacancies in Ge are very unlikely to possess positive charge states (cf section 4.1.1), the mechanisms of acceptor diffusion will be quite different from donor diffusion. There is no Coulomb attraction between vacancies and acceptor atoms and the vacancy concentration will not be enhanced by acceptor concentrations exceeding n_i. Actually a much faster donor diffusion as compared to acceptor diffusion is one of the challenges in producing Ge devices.

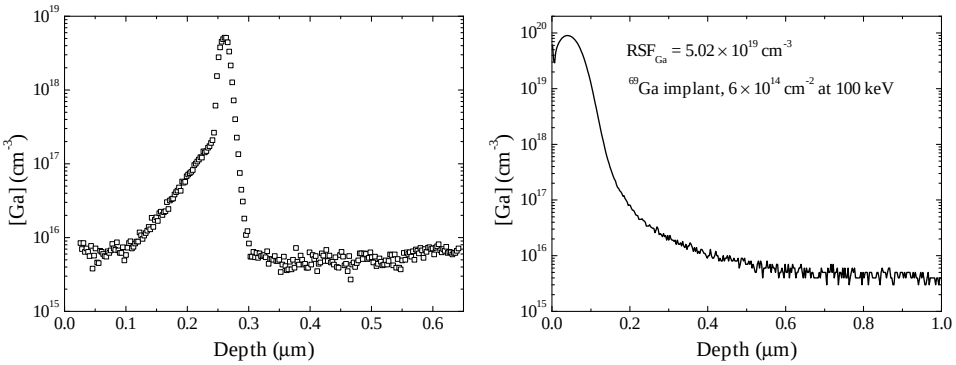

Figure 5.11: The depth profile of Ga measured by SIMS on a Ge sample containing a buried spike of Ga (left) grown by MBE. On the right is shown the profile of a sample implanted with Ga to serve as a concentration reference. The O_2^+ current was ~130 nA at an energy of 10 keV.

In fact B has been seen to diffuse extremely slow in thermal equilibrium [Uppal 2004] with an activation energy as high as 4.65 eV. Very recently it

has been demonstrated that proton irradiation strongly enhances the B diffusion [Bruno 2009], which also gave indications that the diffusion proceeds by a kick-out reaction. Finally it was decisively shown that a self-interstitial supersaturation is produced by proton irradiation, and thus that B diffusion is indeed mediated by an interstitial diffusion mechanism [Bracht 2009]. This is the only case where is has been unambiguously shown that an acceptor, or donor for that matter, diffuses by an interstitial mechanism in Ge. The other three acceptors (Al, Ga and In) are theoretically predicted to be able to diffuse via a vacancy mechanism, and the literature does indeed indicate them to diffuse with substantially lower activation energies than B [Chroneos 2008].

The most recent study investigating Ga diffusion in Ge was carried out using an implanted Ga profile [Riihimäki 2007]. We wanted to carry out diffusion experiments using instead a buried Ga spike to try and reproduce those results. For this purpose a Ge sample with the Ga depth profile shown in the left hand side of figure 5.11 was grown by MBE. The right hand side shows an implanted concentration reference.

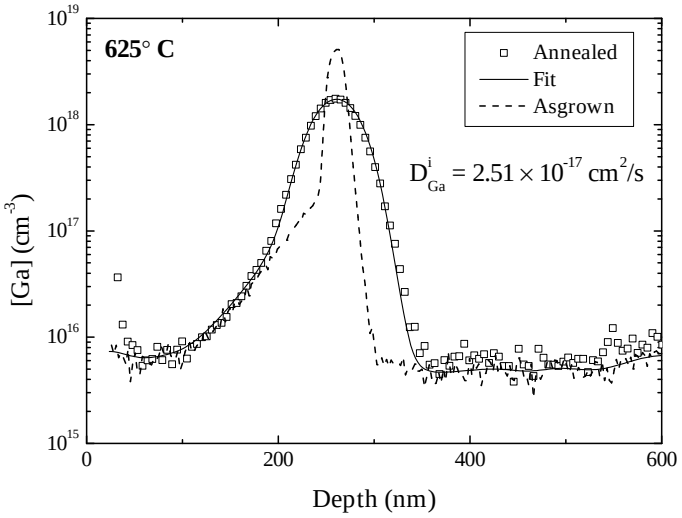

Figure 5.12: The Ga depth profile measured by SIMS after annealing in vacuum at 625°C for 20 hours (open squares). The dashed line shows the as-grown sample while the black solid line is a fit resulting from a least squares minimization process. The O_2^+ current was ~130 nA at an energy of 10 keV.

SIMS measurements on Ga were done at the Cameca 4f equipment at KTH

in Sweden. Ga can be detected directly by ^{69}Ga, and there are no mass interferences. O_2^+ is used as the primary ion since Ga yields very few positive ions.

Annealing such a sample in vacuum at 625°C for 20 hours (with a 130 nm SiO_2 cap on top) results in the Ga depth profile in figure 5.12 after the cap has been etched away. The solid black line is the result of a fit using a concentration independent diffusion coefficient, but including the electric field factor h in (2.64). The best fit has been determined by a least squares minimization process varying D^{i}_{Ga}. This fit reproduces the diffusion due to annealing well, and we thus conclude that the diffusion coefficient is independent of the carrier concentration. If the opposite was true the profile shape would be more flat. It should be noted that omitting the h factor produces a slightly better fit, but there is no physical reason to omit it in this case.

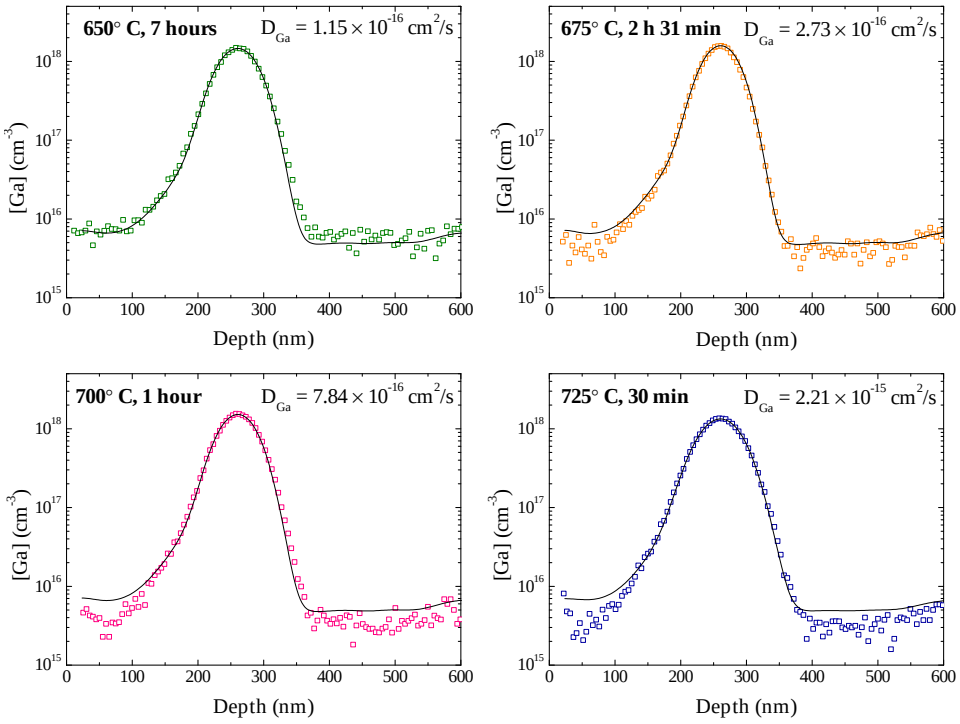

Figure 5.13: Depth profiles of Ga after annealing measured by SIMS (open squares). The solid black lines show the simulation of the annealing obtained by a least squares minimization process. The O_2^+ current was ~130 nA at an energy of 10 keV.

Carrying out annealing a higher temperatures results in the depth profiles

shown in figure 5.13. The fits resulting from the same method as above are shown by solid black lines, and again the agreement between simulation and measurement is very good.

The extracted diffusion coefficients fit an Arrhenius expression nicely as shown in an Arrhenius plot, figure 5.14. The extracted value of the activation energy $Q = 3.4 \pm 0.1$ eV agrees relatively well with the results of [Riihimäki 2007] (shown in the figure by the dashed line). They find an activation energy lower by 0.2 eV and a lower prefactor, but judging from figure 5.14 the prefactor is responsible for the main difference between the experiments. This difference could be due to the type of experiment used in the two cases (implanted Ga in their case).

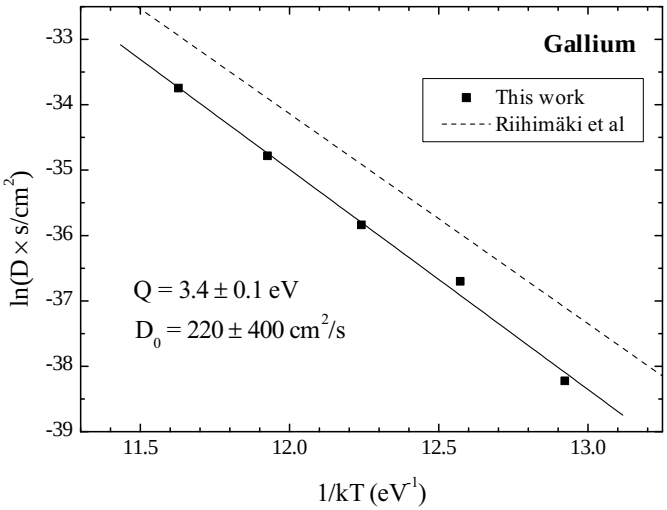

Figure 5.14: Arrhenius plot of the Ga diffusion coefficient demonstrating it follows an Arrhenius expression by the; the solid line is a linear fit. The diffusion parameters found by [Riihimäki 2007] are represented by the dashed line.

In line with the findings by Riihimäki *et al*. we have seen that the diffusion coefficient does not depend on carrier concentration. This is a strong indication that the diffusion is mediated by a neutral point defect. In the light that the diffusion parameters are comparable to those of self-diffusion ($Q = 3.13$ eV and $D_0 = 25$ cm^2/s) a vacancy mediated diffusion of Ga in Ge is very likely. As mentioned earlier this agrees with the theoretical calculations by Chroneos *et al*. We thus arrive at the conclusion that Ga diffusion in

Ge proceeds via neutral vacancies. It would however be very interesting to see if the diffusion can proceed via an interstitial method as well. This could be done by carrying out an experiment of diffusion under proton irradiation similar to that of [Bracht 2009].

5.4 Summary

Annealing experiments showed clearly that even with a protective SiO_2 cap layer, annealing of Ge in a nitrogen flow around 500 °C does not yield equilibrium diffusion. The oxidation of Ge causes a supersaturation of vacancies, which is however reduced by the cap. Vacuum annealing was used to circumvent the influence of oxidation, and a SiO_2 cap (100–130 nm) was maintained to prevent evaporation.

Buried impurity profiles grown by MBE were used to study diffusion of donors and acceptors as a function of temperature. The SiO_2 cap was deposited using magnetron sputtering before the annealing, and removed by etching with a 10% HF solution before depth profiling with SIMS.

For arsenic (As) a concentration dependent diffusion coefficient was required to get a satisfactory description of the diffusion. The model used was that of [Brotzmann 2008b], $D_{\mathrm{As}} = D^{\mathrm{i}}_{\mathrm{As}} \cdot (n/n_{\mathrm{i}})^2$, recently used to describe As, Sb and P diffusion.

This resulted in the following expression for the intrinsic diffusion coefficient:

$$D^{\mathrm{i}}_{\mathrm{As}}(T) = 1.3 \times \exp\left(-\frac{2.4\mathrm{eV}}{k_{\mathrm{B}}T}\right) \mathrm{cm}^2/\mathrm{s}. \tag{5.1}$$

These parameters do not agree with those from Brotzmann *et al.* ($D_0 = 32\,\mathrm{cm}^2/\mathrm{s}$ and $Q = 2.71$ eV), so this indicates that a more detailed model, such as that of [Canneaux 2009] used for phosphorus diffusion, is needed. More studies with a lower As concentration is needed to answer which model is correct.

The acceptor gallium (Ga) was studied. Despite the peak concentration being well over n_{i} in the samples, a concentration dependent model for D_{Ga} was not required. This is in agreement with a recent experiment investigating ^{66}Ga[5] diffusion in a high concentration Ga background; they saw no influence

[5] A radioactive isotope.

of the doping on the Ga diffusion. The field effect from a gradient in the impurity profile (2.64), which becomes important for high concentrations, is however included in the simulations. The resulting expression for $D_{\mathrm{Ga}} = D^{\mathrm{i}}_{\mathrm{Ga}}$ is:

$$D_{\mathrm{Ga}}(T) = 220 \times \exp\left(-\frac{3.4\mathrm{eV}}{k_{\mathrm{B}}T}\right) \mathrm{cm}^2/\mathrm{s}. \tag{5.2}$$

This does not agree perfectly with the expression found by Riihimäki *et al.* ($D_0 = 8\ \mathrm{cm}^2/\mathrm{s}$ and $Q = 3.21$ eV), but the disagreement is mainly in the prefactor, which could be due to the different nature of the experiments. The independence of D_{Ga} on the carrier concentration can readily be interpreted as the diffusion being mediated by neutral vacancies, since interstitial mediated diffusion proceeds with a substantially higher activation energy ($Q_{\mathrm{B}} = 4.65$ eV [Uppal 2004]). This is in line with the self-diffusion activation energy (3.13 eV [Hüger 2008]) being close to, but slightly lower than that of Ga. Finally the absence of positively charged vacancies can be inferred, which is in line with results from DLTS as well as DFT calculations (cf section 4.1.1).

CHAPTER 6

Conclusions and perspectives

6.1 Conclusions

The main topics in this thesis were defects in germanium with electronic levels in the band gap and the diffusion of donors and acceptors in crystalline germanium. In chapter 4 a study of defect energy levels in the band gap, introduced by irradiation with high energy electrons, protons and alpha particles, in n-type as well as p-type, was presented.

- The di-vacancy, being an important defect for silicon, was of special interest. It was concluded that it introduces no electronic levels in the upper part of the band gap in line with theory and other experiments. A DLTS peak in p-type germanium, which is present after irradiation, was assigned to a negative-U transition of the di-vacancy, $V_2^{(=/0)}$. The double acceptor level has thus moved further down in the band gap than the single acceptor, and both levels are represented by a single DLTS peak. Annealing of the di-vacancy was suggested to be due to the annihilation by another defect, suggested to be the di-interstitial, I_2, giving a DLTS peak in p-type as well. Finally if the temperature of irradiation was low enough, leaving the di-vacancy neutral when the vacancy becomes mobile, the di-vacancy is claimed to convert to a tri-vacancy through vacancy capture.

- *In situ* experiments after electron irradiation at cryogenic temperatures (less than ~60 K) allowed the observation of energy levels of the vacancy, self-interstitial, Frenkel-pair and Ga_i defects. These defects are unstable at RT and can thus not be observed after ordinary RT irradiations.

- In addition the single acceptor of the oxygen-vacancy pair, previously only described in n-type germanium, was observed in p-type n^+p mesa

diodes, due to the in-diffusion of oxygen from the top-layer.

Chapter 5 reports first of all the challenges encountered, when attempting to do diffusion experiments on germanium under equilibrium conditions. It was found that annealing in vacuum was absolutely crucial to avoid oxygen influence. The samples used for diffusion studies consisted of buried layers of the impurity in question grown by MBE. This approach is complementary to that in the literature, where in-diffusion from the surface or implantation in a region near the surface is used. The goal with this approach is to avoid implantation damage and possible influence from the surface.

- Arsenic (As) diffusion was studied in the interval between 510°C and 590°C, and a concentration dependent diffusion coefficient was used to model the diffusion, $D_{\mathrm{As}} = D^{\mathrm{i}}_{\mathrm{As}} \cdot (n/n_{\mathrm{i}})^2$. This resulted in an Arrhenius expression for the intrinsic diffusion coefficient with the parameters $D^{\mathrm{i}}_{\mathrm{As},0} = 1.3 \pm 0.4$ cm^2/s and $Q^{\mathrm{i}}_{\mathrm{As}} = 2.4 \pm 0.1$ eV. These values does not perfectly match recent literature values ($D^{\mathrm{i}}_{\mathrm{As},0} = 32$ cm^2/s and $Q^{\mathrm{i}}_{\mathrm{As},0} = 2.71$ eV [Brotzmann 2008b]), but more experiments are needed to elaborate on the difference.

- Gallium (Ga) diffusion was studied between 625°C and 725°C, which clearly demonstrated that the gallium diffusion coefficient does not exhibit a concentration dependence. This shows the absence of positively charged vacancies and that Ga diffusion is mediated by neutral vacancies. The resulting Arrhenius expression has the parameters $D^{\mathrm{i}}_{\mathrm{Ga},0} = 220 \pm 400$ cm^2/s and $Q^{\mathrm{i}}_{\mathrm{Ga}} = 3.4 \pm 0.1$ eV. This mainly deviates from recent experimental values in the prefactor ($D^{\mathrm{i}}_{\mathrm{Ga},0} = 8$ cm^2/s and $Q^{\mathrm{i}}_{\mathrm{Ga}} = 3.21$ eV [Riihimäki 2007]), which is likely due to the different nature of the experiments.

6.2 Future perspectives

The defect studies in germanium could benefit greatly from EPR examinations, so it is a hope for the future that someone succeeds in such a project. In addition electron irradiations at substantially higher energies (at least 10 MeV)

would be interesting, so as to bridge the gap between 2 MeV electron and proton irradiation.

Carbon related defects would be interesting to study in p-type germanium by the implantation of carbon (at an energy of several MeV) into the substrate before MBE growth of n^+p structures.

Diffusion studies of buried layers of arsenic and gallium, with concentrations higher than n_i at the diffusion temperatures, indicated diffusion parameters different from other studies by different methods. Therefore it would be highly interesting to carry out the same experiments with concentrations strictly below n_i.

Gallium could be a very interesting element to subject to radiation enhanced diffusion (RED) in germanium, as has been done for boron [Bruno 2009, Bracht 2009]. This could reveal if an interstitial diffusion mechanism is possible for gallium, even though it diffuses by a vacancy mechanism under thermal equilibrium.

APPENDIX A

MATLAB code for diffusion simulation

The MATLAB code presented in this appendix is available at `http://www.phys.au.dk/~mcp/diffsim.zip`.

A.1 diffsim.m

This function simulates the diffusion with a given diffusion coefficient.

```
1  function [x C RSS R2 SDW] = diffsim (x,C,D,t,padding,noncons,
       compare_x,compare_y)
2  if nargin<5, padding = 0; end
3  if nargin<6, noncons = 0.06; end
4  if nargin<7, compare_x = []; end
5  if nargin<8, compare_y = []; end
6  RSS = 0;
7  SDW = 0;
8  R2 = 0;
9  % 1 cm^2 = 1e14 nm^2
10 dx = x(2,1) - x(1,1);
11
12 % Calculate the no of steps required to keep the concentration
       change at 2%
13 steps = ceil(1e14*t*D/(0.01*dx^2));
14
15 dt = t/steps;
16
17 p = D*dt/dx^2*1e14;
18 points = size(x,1)+padding;
19 C = vertcat(C,C(size(x,1),1)*ones(padding,1));
20 x = vertcat(x,dx*size(x,1)*ones(padding,1)+dx*(1:padding)');
```

```
21
22 M = diag(ones(points,1))+1e14*D*dt/dx^2*(-2*diag(ones(points,1))
       ...
23      +diag(ones(points-1,1),1)...
24      +diag(ones(points-1,1),-1));
25 M(1,1) = M(1,1)+(1-noncons)*1e14*D*dt/dx^2;
26 noncons2 = 0; % non-conservative contribution set to zero at
       right end
27 M(points,points)=M(points,points)+(1-noncons2)*1e14*D*dt/dx^2;
28 C = M^steps*C;
29 if ¬isempty(compare_x)
30      xm = x'*C/sum(C);
31      [RSS R2 SDW] = diffsim_compare(compare_x,compare_y,x,C,xm);
32      %fprintf('Root of Sum of Squares comparison: %.7s\n',SSD);
33 end
34 if nargout==0, plot(x,C,compare_x,compare_y,'o'); end
```

A.2 diffsim_leastsquares.m

This function determines the diffusion coefficient best fitting the diffused impurity profile by minimizing the sum of squares of the residuals (RSS) between the simulated and measured profile.

```
1  function [D D_lower D_upper RSS xsim Csim] = diffsim_leastsquares
       (x,C,Dstart,t,tolerance,padding,noncons,compx,compC,sigma)
2  if nargin<10; sigma=0; end
3  D_lower = 0;
4  D_upper = 0;
5
6  D = Dstart;
7  N = size(compx,1);
8  R2 = 0;
9
10 chisq_conf = chi2inv(0.95,N); % chi^2 less than this occurs with
       95% probability
11 [x2 C2 RSS2 R2_2] = diffsim(x,C,D,t,padding,noncons,compx,compC);
12 if (isnan(RSS2)), error('NaN encountered, add more steps!'); end
13
14 iteration = 1;
```

```
15 ΔD = D/10;
16
17 fprintf('Start parameters: D = %.3e, ΔD = %.2e, ',D,ΔD);
18 if sigma>0; fprintf('chi^2= %.3e/%.3e <-- 95%% confidence
       threshold.',RSS2/sigma^2,chisq_conf); else fprintf('R^2= %.6f,
        ',R2_2); end
19 fprintf('\n');
20 while iteration==1||ΔD>tolerance
21     fprintf('Iteration no. %.0f, D = %.4e, ΔD = %.4e\n',iteration
           ,D,ΔD);
22     % Try decreasing D by ΔD
23     [x1 C1 RSS1 R2_1] = diffsim(x,C,D-ΔD,t,padding,noncons,compx,
           compC);
24
25     % Try increasing D by ΔD
26     [x3 C3 RSS3 R2_3] = diffsim(x,C,D+ΔD,t,padding,noncons,compx,
           compC);
27     if (isnan(RSS1)||isnan(RSS3)), error('NaN encountered, add
           more steps!'); end
28
29     j = 0;
30     while RSS2>RSS1
31         % if increasing D is better cancel decreasing it
32         if RSS1>RSS3; break; end
33
34         iteration = iteration + 1;
35         % We already took two steps of this size so lets try
               larger steps
36         if j>1, ΔD = 3*ΔD; j = 0; fprintf('  ++Increasing ΔD to %
               .4e\n',ΔD); end
37
38         %plot(x1,C1);
39         %legend(sprintf('iteration no. %.0f',iteration));
40
41         % Decrease D until RSS no longer decreases
42         D = D - ΔD;
43
44         while D<0; % ensure that D is not negative
45             D = D+ΔD/2;
46             ΔD = ΔD/2;
47         end
48
```

```
49          fprintf('Iteration no. %.0f, D = %.4e, ',iteration,D);
50          if sigma>0; fprintf('chi^2 = %.3e/%.3e',RSS1/sigma^2,
                chisq_conf); else fprintf('R^2 = %.6f',R2_1); end
51          fprintf('\n');
52
53
54          RSS2 = RSS1;
55          R2 = R2_1;
56          x2 = x1;
57          C2 = C1;
58          [x1 C1 RSS1 R2_1] = diffsim(x,C,D-ΔD,t,padding,noncons,
                compx,compC);
59          if (isnan(RSS1)), error('NaN encountered, add more steps!
                '); end
60          j = j + 1;
61      end
62
63      j = 0;
64      while RSS2>RSS3
65          iteration = iteration + 1;
66
67          % We already took two steps of this size so lets try
                larger steps
68          if j>1, ΔD = 3*ΔD; j = 0; fprintf('  ++Increasing ΔD to %
                .4e\n',ΔD); end
69
70          % Increase D until RSS no longer decreases
71          D = D + ΔD;
72          fprintf('Iteration no. %.0f, D = %.4e, ',iteration,D);
73          if sigma>0; fprintf('chi^2 = %.3e/%.3e',RSS3/sigma^2,
                chisq_conf); else fprintf('R^2 = %.6f',R2_3); end
74          fprintf('\n');
75
76          RSS2 = RSS3;
77          R2 = R2_3;
78          x2 = x3;
79          C2 = C3;
80          [x3 C3 RSS3 R2_3] = diffsim(x,C,D+ΔD,t,padding,noncons,
                compx,compC);
81          if (isnan(RSS3)), error('NaN encountered, add more steps!
                '); end
82          j = j+1;
```

```
    end

    ΔD = ΔD/2;

    iteration = iteration + 1;
end
i=1;
xmax = compx(size(compx,1),1);
imax = size(x2,1);
if x2(imax,1)<xmax; i = imax; end
while x2(i,1)<xmax&&i<imax, i = i+1; end

if nargout<5; plot(x2(1:i,1),C2(1:i,1),compx,compC,'o'); end

xsim = x2;
Csim = C2;

RSS=RSS2;
fprintf('Done: D = %.4e , ',D);
if sigma>0;
    fprintf('chi^2 = %.3e/%.3e <-- 95%% confidence threshold.\n\n
        ',RSS/sigma^2,chisq_conf);
    if nargout>1; [D_lower D_upper] = diffsim_confidence(x,C,D,t,
        padding,noncons,chisq_conf+RSS/sigma^2,sigma,compx,compC);
         end
else
    fprintf('R^2 = %.6f\n\n',R2);
end

end
```

A.3 diffsim_compare.m

This function compares the diffused profile with the measured profile, interpolating between points if necessary, and returns the sum of squared residuals (RSS).

```
% C1 should be the measured profile and C2 the simulated one
% Given that the profile is a localized spike a positive rdiffw
```

```
    signifies
% too little diffusion and a negative too much.
%
% Returns the square root of the sum of square differences (SSD) between the two
% profiles (rdiffsq) and a weighted difference sum (rdiffw) if a reference point (xm),
% usually a peak position, is given. If there is a difference between the
% sample spacing in the depth profiles an interpolation is made to properly
% compare the two.
function [RSS R2 diffw] = diffsim_compare(x1,C1,x2,C2,xm)
if nargin<5, xm = 0; end
dx1 = x1(2,1)-x1(1,1);
dx2 = x2(2,1)-x2(1,1);
x1_0 = x1(1,1);
x2_0 = x2(1,1);
dx = abs(x1_0-x2_0);

if dx>min(dx1,dx2)
    % need to pad one of the profiles on the left to have the same depth range
    if x1_0>x2_0
        n0 = floor(dx/dx1);
        C1 = vertcat(C1(1,1)*ones(n0,1),C1);
        x1 = vertcat(dx1*(-n0:-1)'+x1(1,1)*ones(n0,1),x1);
        x1_0 = x1(1,1);
    else
        n0 = floor(dx/dx2);
        C2 = vertcat(C2(1,1)*ones(n0,1),C2);
        x2 = vertcat(dx2*(-n0:-1)'+x2(1,1)*ones(n0,1),x2);
        x2_0 = x2(1,1);
    end
end

if abs(dx1-dx2)/dx1>0.01 % suitable threshold for dx1 and dx2 being different
    % need to interpolate x2 to be able to compare
    m = floor(size(x2,1)*dx2/dx1);
    if (m*dx1+x1_0-x2_0)/dx2>size(x2,1); m = m-1; end
    C2i = zeros(m,1);
```

```
38
39      C2i(1,1) = C2(1,1)-(x2_0-x1_0)*(C2(2,1)-C2(1,1))/dx2;
40      for i=2:m
41          j = (i*dx1+x1_0-x2_0)/dx2;
42          jlow = floor(j);
43          jhigh = ceil(j);
44          C2i(i,1) = C2(jhigh,1)*(j-jlow)+C2(jlow,1)*(1-j+jlow);
45      end
46  else
47      C2i = C2;
48  end
49
50  n = size(C1,1)-size(C2i,1);
51
52  if n≠0
53      if n>0, C2i=vertcat(C2i,C2i(size(C2i,1),1)*ones(n,1)); else
            C1=vertcat(C1,C1(size(C1,1),1)*ones(-n,1)); end
54  end
55
56  x = dx1*(0:size(C2i,1)-1)'+x1_0*ones(size(C2i,1),1);
57  C_diff = C2i-C1;
58
59  RSS = sum((C_diff).^2);
60  SStot = sum((C1-mean(C1)*ones(size(C1))).^2);
61  R2 = 1-RSS/SStot;
62  diffw = 0;
63  if xm≠0, diffw =sum(C_diff./(1+(x-xm).^2/xm^2)); end
```

A.4 diffsim_extrinsic.m

This function simulates extrinsic diffusion with $D = D0 + D1 \cdot (n/n_i) + D2 \cdot (n/n_i)^2 + D3 \cdot (n/n_i)^3$.

```
1  function [x C RSS R2 SDW] = diffsim_extrinsic (x,C,D0,D1,D2,D3,t,
       padding,noncons,temp,compare_x,compare_y)
2  if nargin<8, padding = 0; end
3  if nargin<9, noncons = 0.06; end
4  if nargin<11, compare_x = []; end
5  if nargin<12, compare_y = []; end
6  RSS = 0;
```

```
SDW = 0;
R2 = 0;
% 1 cm^2 = 1e14 nm^2

dx = x(2,1) - x(1,1);
points = size(x,1)+padding;

ni = 1.8e16*temp^1.5*exp(-4555/temp); % intrinsic carrier
    concentration

% Determine the initially needed stepsize - given that the
    maximum concentration change is 2%
z = C/ni; % N/ni
n_r = 0.5*z + sqrt(ones(points,1) + 0.25*z.^2); % n/ni
k = max(n_r);
Dmax = (1+0.5*k/sqrt(1+0.25*k^2))*(D0+D1*k+D2*k^2+D3*k^3);
steps = 1e14*t*Dmax/(dx^2*0.02);

dt = t/steps;

C = vertcat(C,C(size(x,1),1)*ones(padding,1));
x = vertcat(x,dx*size(x,1)*ones(padding,1)+dx*(1:padding)');
dM = 1e14*dt/dx^2*(-2*diag(ones(points,1))...
    +diag(ones(points-1,1),1)...
    +diag(ones(points-1,1),-1));
dM(1,1) = dM(1,1)+(1-noncons)*1e14*dt/dx^2;
noncons2 = 0; % non-conservative contribution set to zero at
    right end
dM(points,points)=dM(points,points)+(1-noncons2)*1e14*dt/dx^2;

p = round(steps/50);

i = 1;
y = 0;
while i≤steps
    z = C/ni; % N/ni
    n_r = 0.5*z + sqrt(ones(points,1) + 0.25*z.^2); % n/ni

    % Determine how large a step we can take
    k = max(n_r);
    Dmax = (1+0.5*k/sqrt(1+0.25*k^2))*(D0+D1*k+D2*k^2+D3*k^3);
    u = 1e14*Dmax*dt/dx^2; % 1cm^2 = 1e14nm^2
```

```
46      n_combine = max(floor(0.02/u),1); % take larger steps to
            speed things up if steps are unnessecary small
47      if n_combine+i>steps, n_combine = max(steps-i,1); end
48
49      C = (diag(ones(points,1))+n_combine*dM*(diag((ones(points,1)+
            z./(2*sqrt(1+z.^2/4))).*(D0+D1*n_r+D2*n_r.^2+D3*n_r.^3))))
            *C;
50      i = i+n_combine;
51
52      % Print out dots to show that something is happening
53      if floor(i/p)>y
54          fprintf('.');
55      y = floor(i/p);
56      end
57  end
58
59  fprintf('\n');
60
61  if ¬isempty(compare_x)
62      xm = x'*C/sum(C);
63      [RSS R2 SDW] = diffsim_compare(compare_x,compare_y,x,C,xm);
64      %fprintf('Root of Sum of Squares comparison: %.7s\n',SSD);
65  end
66  if nargout==0, plot(x,C); end
```

A.5 diffsim_leastsquares_extrinsic.m

This function finds the set of diffusion coefficients (D0,D1,D2,D3), as defined in connection with diffsim_extrinsic.m, best fitting the diffusion along a straight line defined by the vector (D0start,D1start,D2start,D3start). It is thus most suitable for testing if a single term will describe the diffusion. Setting

$$(D0start, D1start, D2start, D3start) = (D, 0, 0, 0)$$

will do the same as diffsim.m but with the field factor, h, included.

```
1  function [D D_lower D_upper RSS xsim Csim] =
       diffsim_leastsquares_extrinsic(x,C,D0start,D1start,D2start,
       D3start,t,tolerance,padding,noncons,temperature,compx,compC,
       sigma)
```

```
2  if nargin<14; sigma=0; end
3  D_lower = 0;
4  D_upper = 0;
5
6  Dm = [D0start D1start D2start D3start];
7  D = max(Dm);
8  Dm = Dm/D;
9  N = size(compx,1);
10 chisq_conf = chi2inv(0.95,N); % chi^2 less than this occurs with
       95% probability
11
12 [x2 C2 RSS2 R2] = diffsim_extrinsic(x,C,D*Dm(1,1),D*Dm(1,2),D*Dm
       (1,3),D*Dm(1,4),t,padding,noncons,temperature,compx,compC);
13 if (isnan(RSS2)), error('NaN encountered, add more steps!'); end
14
15 iteration = 1;
16 ΔD = D/10;
17
18 fprintf('Start parameters: D = %.3e, ΔD = %.2e, ',D,ΔD);
19 if sigma>0; fprintf('chi^2= %.3e/%.3e <-- 95%% confidence
       threshold.',RSS2/sigma^2,chisq_conf); else fprintf('R^2= %.6f,
        ',R2); end
20 fprintf('\n');
21 while iteration==1||ΔD>tolerance
22     fprintf('Iteration no. %.0f, D = %.4e, ΔD = %.4e\n',iteration
           ,D,ΔD);
23     % Try decreasing D by ΔD
24     [x1 C1 RSS1 R2_1] = diffsim_extrinsic(x,C,(D-ΔD)*Dm(1,1),(D-Δ
           D)*Dm(1,2),(D-ΔD)*Dm(1,3),(D-ΔD)*Dm(1,4),t,padding,noncons
           ,temperature,compx,compC);
25
26     % Try increasing D by ΔD
27     [x3 C3 RSS3 R2_3] = diffsim_extrinsic(x,C,(D+ΔD)*Dm(1,1),(D+Δ
           D)*Dm(1,2),(D+ΔD)*Dm(1,3),(D+ΔD)*Dm(1,4),t,padding,noncons
           ,temperature,compx,compC);
28     if (isnan(RSS1)||isnan(RSS3)), error('NaN encountered, add
           more steps!'); end
29
30     j = 0;
31     while RSS2>RSS1
32         % if increasing D is better cancel decreasing it
33         if RSS1>RSS3; break; end
```

```
34
35          iteration = iteration + 1;
36          % We already took two steps of this size so lets try
                larger steps
37          if j>1, ΔD = 3*ΔD; j = 0; fprintf('  ++Increasing ΔD to %
                .4e\n',ΔD); end
38
39          % Decrease D until RSS no longer decreases
40          D = D - ΔD;
41
42          while D<0; % ensure that D is not negative
43              D = D+ΔD/2;
44              ΔD = ΔD/2;
45          end
46
47          fprintf('Iteration no. %.0f, D = %.4e, ',iteration,D);
48          if sigma>0; fprintf('chi^2 = %.3e/%.3e',RSS1/sigma^2,
                chisq_conf); else fprintf('R^2 = %.6f',R2_1); end
49          fprintf('\n');
50
51          RSS2 = RSS1;
52      R2 = R2_1;
53          x2 = x1;
54          C2 = C1;
55          [x1 C1 RSS1 R2_1] = diffsim_extrinsic(x,C,(D-ΔD)*Dm(1,1)
                ,(D-ΔD)*Dm(1,2),(D-ΔD)*Dm(1,3),(D-ΔD)*Dm(1,4),t,
                padding,noncons,temperature,compx,compC);
56          if (isnan(RSS1)), error('NaN encountered, add more steps!
                '); end
57          j = j + 1;
58      end
59
60      j = 0;
61      while RSS2>RSS3
62          iteration = iteration + 1;
63
64          % We already took two steps of this size so lets try
                larger steps
65          if j>1, ΔD = 3*ΔD; j = 0; fprintf('  ++Increasing ΔD to %
                .4e\n',ΔD); end
66
67          % Increase D until RSS no longer decreases
```

```
68          D = D + ΔD;
69          fprintf('Iteration no. %.0f, D = %.4e, ',iteration,D);
70          if sigma>0; fprintf('chi^2 = %.3e/%.3e',RSS3/sigma^2,
                chisq_conf); else fprintf('R^2 = %.6f',R2_3); end
71          fprintf('\n');
72
73          RSS2 = RSS3;
74      R2 = R2_3;
75          x2 = x3;
76          C2 = C3;
77          [x3 C3 RSS3 R2_3] = diffsim_extrinsic(x,C,(D+ΔD)*Dm(1,1)
                ,(D+ΔD)*Dm(1,2),(D+ΔD)*Dm(1,3),(D+ΔD)*Dm(1,4),t,
                padding,noncons,temperature,compx,compC);
78          if (isnan(RSS3)), error('NaN encountered, add more steps!
                '); end
79          j = j+1;
80      end
81
82      ΔD = ΔD/2;
83
84      iteration = iteration + 1;
85  end
86  i=1;
87  xmax = compx(size(compx,1),1);
88  imax = size(x2,1);
89  if x2(imax,1)<xmax; i = imax; end
90  while x2(i,1)<xmax&&i<imax, i = i+1; end
91
92  if nargout<5; plot(x2(1:i,1),C2(1:i,1),compx,compC,'o'); end
93
94  xsim = x2;
95  Csim = C2;
96
97  RSS=RSS2;
98  fprintf('Done: D = %.4e , ',D);
99  fprintf('R^2 = %.6f\n\n',R2);
100
101 end
```

Bibliography

[Antoniadis 1982] D. A. Antoniadis and I. Moskowitz. *Diffusion of substitutional impurities in silicon at short oxidation times: An insight into point defect kinetics*. Journal of Applied Physics, vol. 53, no. 10, pages 6788–6796, 1982. 116

[Auret 2006] F. D. Auret, P. J. Janse van Rensburg, M. Hayes, J. M. Nel, W. E. Meyer, S. Decoster, V. Matias and A. Vantomme. *Electrical characterization of defects introduced in n-type Ge during indium implantation*. Applied Physics Letters, vol. 89, no. 15, page 152123, 2006. 74, 76, 105

[av Skardi 2002] H. av Skardi, A. Bro Hansen, A. Mesli and A. Nylandsted Larsen. *The di-vacancy in particle-irradiated, strain-relaxed SiGe*. Nuclear Instruments and Methods in Physics Research Section B: Beam Interactions with Materials and Atoms, vol. 186, no. 1-4, pages 195 – 200, 2002. 66, 68

[Bardeen 1948] J. Bardeen and W. H. Brattain. *The Transistor, A Semi-Conductor Triode*. Phys. Rev., vol. 74, no. 2, pages 230–231, Jul 1948. 1

[Batterman 1962] Boris W. Batterman and David R. Chipman. *Vibrational Amplitudes in Germanium and Silicon*. Phys. Rev., vol. 127, no. 3, pages 690–693, Aug 1962. 94

[Bean 1971] A.R. Bean and R.C. Newman. *The solubility of carbon in pulled silicon crystals*. Journal of Physics and Chemistry of Solids, vol. 32, no. 6, pages 1211 – 1219, 1971. 101

[Blood 1992] P. Blood and J. W. Orton. The electrical characterization of semiconductors: majority carriers and electron states. Academic Press, 1992. 21

[Bourgoin 1972] J.C Bourgoin and J.W Corbett. *A new mechanism for interstitial migration*. Physics Letters A, vol. 38, no. 2, pages 135 – 137, 1972. 64, 94

[Bracht 1998] H. Bracht, E. E. Haller and R. Clark-Phelps. *Silicon Self-Diffusion in Isotope Heterostructures*. Phys. Rev. Lett., vol. 81, no. 2, pages 393–396, Jul 1998. 107

[Bracht 2006a] Hartmut Bracht and Sergej Brotzmann. *Atomic transport in germanium and the mechanism of arsenic diffusion*. Materials Science in Semiconductor Processing, vol. 9, no. 4-5, pages 471 – 476, 2006. Proceedings of Symposium T E-MRS 2006 Spring Meeting on Germanium based semiconductors from materials to devices. 55

[Bracht 2006b] Hartmut Bracht and Sergej Brotzmann. *Atomic transport in germanium and the mechanism of arsenic diffusion*. Materials Science in Semiconductor Processing, vol. 9, no. 4-5, pages 471 – 476, 2006. Proceedings of Symposium T E-MRS 2006 Spring Meeting on Germanium based semiconductors from materials to devices. 108

[Bracht 2007] H. Bracht. *Self- and foreign-atom diffusion in semiconductor isotope heterostructures. I. Continuum theoretical calculations*. Physical Review B (Condensed Matter and Materials Physics), vol. 75, no. 3, page 035210, 2007. 29

[Bracht 2009] H. Bracht, S. Schneider, J. N. Klug, C. Y. Liao, J. Lundsgaard Hansen, E. E. Haller, A. Nylandsted Larsen, D. Bougeard, M. Posselt and C. Wündisch. *Interstitial-Mediated Diffusion in Germanium under Proton Irradiation*. Phys. Rev. Lett., vol. 103, no. 25, page 255501, Dec 2009. 121, 124, 129

[Brotzmann 2008a] S. Brotzmann, H. Bracht, J. Lundsgaard Hansen, A. Nylandsted Larsen, E. Simoen, E. E. Haller, J. S. Christensen and P. Werner. *Diffusion and defect reactions between donors, C, and vacancies in Ge. I. Experimental results*. Physical Review B (Condensed Matter and Materials Physics), vol. 77, no. 23, page 235207, 2008. 101

[Brotzmann 2008b] Sergej Brotzmann and Hartmut Bracht. *Intrinsic and extrinsic diffusion of phosphorus, arsenic, and antimony in germanium*. Journal of Applied Physics, vol. 103, no. 3, page 033508, 2008. 113, 115, 117, 118, 119, 124, 128

[Bruno 2009] E. Bruno, S. Mirabella, G. Scapellato, G. Impellizzeri, A. Terrasi, F. Priolo, E. Napolitani, D. De Salvador, M. Mastromatteo and A. Carnera. *Mechanism of B diffusion in crystalline Ge under proton irradiation*. Phys. Rev. B, vol. 80, no. 3, page 033204, Jul 2009. 121, 129

[Callcott 1967] T. A. Callcott and J. W. Mackay. *Irradiation Damage in n-Type Germanium at 4.2°K*. Phys. Rev., vol. 161, no. 3, pages 698–710, Sep 1967. 9, 64, 71

[Canneaux 2009] Thomas Canneaux, Daniel Mathiot, Jean-Pierre Ponpon and Yann Leroy. *Modeling of phosphorus diffusion in Ge accounting for a cubic dependence of the diffusivity with the electron concentration*. Thin Solid Films, vol. In Press, Corrected Proof, pages –, 2009. 55, 114, 120, 124

[Carvalho 2007] A. Carvalho, R. Jones, C. Janke, J. P. Goss, P. R. Briddon, J. Coutinho and S. Öberg. *Self-Interstitial in Germanium*. Physical Review Letters, vol. 99, no. 17, page 175502, 2007. 64

[Chelikowsky 1976] James R. Chelikowsky and Marvin L. Cohen. *Nonlocal pseudopotential calculations for the electronic structure of eleven diamond and zinc-blende semiconductors*. Phys. Rev. B, vol. 14, no. 2, pages 556–582, Jul 1976. 3

[Chroneos 2006] A. Chroneos, R.W. Grimes and C. Tsamis. *Atomic scale simulations of arsenic-vacancy complexes in germanium and silicon*. Materials Science in Semiconductor Processing, vol. 9, no. 4-5, pages 536 – 540, 2006. Proceedings of Symposium T E-MRS 2006 Spring Meeting on Germanium based semiconductors from materials to devices. 68, 69

[Chroneos 2008] A. Chroneos, H. Bracht, R. W. Grimes and B. P. Uberuaga. *Vacancy-mediated dopant diffusion activation enthalpies for germanium*. Applied Physics Letters, vol. 92, no. 17, page 172103, 2008. 121

[Corbett 1961] J. W. Corbett and G. D. Watkins. *Silicon Divacancy and its Direct Production by Electron Irradiation*. Phys. Rev. Lett., vol. 7, no. 8, pages 314–316, Oct 1961. 70

[Corbett 1964] J.W. Corbett, R.S. McDonald and G.D. Watkins. *The configuration and diffusion of isolated oxygen in silicon and germanium*. Journal of

Physics and Chemistry of Solids, vol. 25, no. 8, pages 873 – 879, 1964. 98

[Coutinho 2005] J Coutinho, R Jones, V J B Torres, M Barroso, S Öberg and P R Briddon. *Electronic structure and Jahn-Teller instabilities in a single vacancy in Ge*. Journal of Physics: Condensed Matter, vol. 17, no. 48, page L521, 2005. 55, 62

[Coutinho 2006] J. Coutinho, V. J. B. Torres, R. Jones, A. Carvalho, S. Öberg and P. R. Briddon. *Calculation of deep carrier traps in a divacancy in germanium crystals*. Applied Physics Letters, vol. 88, no. 9, page 091919, 2006. 67, 68

[D'Arcy-Gall 2001] J. D'Arcy-Gall, D. Gall, I. Petrov, P. Desjardins and J. E. Greene. *Quantitative C lattice site distributions in epitaxial $Ge_{1-y}C_y$/Ge(001) layers*. Journal of Applied Physics, vol. 90, no. 8, pages 3910–3918, 2001. 102

[Dash 1955] W. C. Dash and R. Newman. *Intrinsic Optical Absorption in Single-Crystal Germanium and Silicon at 77°K and 300°K*. Phys. Rev., vol. 99, no. 4, pages 1151–1155, Aug 1955. 23

[Day 1979] D. S. Day, M. Y. Tsai, B. G. Streetman and D. V. Lang. *Deep-level-transient spectroscopy: System effects and data analysis*. Journal of Applied Physics, vol. 50, no. 8, pages 5093–5098, 1979. 16

[Dobaczewski 2004] L. Dobaczewski, A. R. Peaker and K. Bonde Nielsen. *Laplace-transform deep-level spectroscopy: The technique and its applications to the study of point defects in semiconductors*. Journal of Applied Physics, vol. 96, no. 9, pages 4689–4728, 2004. 19

[Dobaczewski 2009] Leszek Dobaczewski. *Laplace DLTS software*. `http://www.laplacedlts.eu`, 2009. 19, 45

[Dunlap 1954] W. C. Dunlap. *Diffusion of Impurities in Germanium*. Phys. Rev., vol. 94, no. 6, pages 1531–1540, Jun 1954. 108

[Emtsev 2006] Vadim Emtsev. *Point defects in germanium: Reliable and questionable data in radiation experiments*. Materials Science in Semiconductor

Processing, vol. 9, no. 4-5, pages 580 – 588, 2006. Proceedings of Symposium T E-MRS 2006 Spring Meeting on Germanium based semiconductors from materials to devices. 60, 63

[Fage-Pedersen 2000] J. Fage-Pedersen, A. Nylandsted Larsen and A. Mesli. *Irradiation-induced defects in Ge studied by transient spectroscopies*. Phys. Rev. B, vol. 62, no. 15, pages 10116–10125, Oct 2000. 22, 26, 70, 71, 72, 88, 99, 102, 103

[Fahey 1989] P. M. Fahey, P. B. Griffin and J. D. Plummer. *Point defects and dopant diffusion in silicon*. Rev. Mod. Phys., vol. 61, no. 2, pages 289–384, Apr 1989. 30

[Frenkel 1938] J. Frenkel. *On Pre-Breakdown Phenomena in Insulators and Electronic Semi-Conductors*. Phys. Rev., vol. 54, no. 8, pages 647–648, Oct 1938. 25

[Ganichev 2000] SD Ganichev, E. Ziemann, W. Prettl, IN Yassievich, AA Istratov and ER Weber. *Distinction between the Poole-Frenkel and tunneling models of electric-field-stimulated carrier emission from deep levels in semiconductors*. Physical Review B, vol. 61, no. 15, pages 10361–10365, 2000. 24, 25

[Gaubas 2006] E. Gaubas and J. Vanhellemont. *Dependence of carrier lifetime in germanium on resisitivity and carrier injection level*. Applied Physics Letters, vol. 89, no. 14, page 142106, 2006. 22

[Haesslein 1998] Helmut Haesslein, Rainer Sielemann and Christian Zistl. *Vacancies and Self-Interstitials in Germanium Observed by Perturbed Angular Correlation Spectroscopy*. Phys. Rev. Lett., vol. 80, no. 12, pages 2626–2629, Mar 1998. 56, 62, 107

[Haller 1982] E. E. Haller, W. L. Hansen, P. Luke, R. McMurray and B. Jarrett. *Carbon in High-Purity Germanium*. IEEE Transactions on Nuclear Science, vol. 29, pages 745–750, 1982. 101

[Hartke 1968] J. L. Hartke. *The Three-Dimensional Poole-Frenkel Effect*. Journal of Applied Physics, vol. 39, no. 10, pages 4871–4873, 1968. 25

[Hemment 1969] P. L. F. Hemment and P. R. C. Stevens. *Study of the Anisotropy of Radiation Damage Rates in n-Type Silicon*. Journal of Applied Physics, vol. 40, no. 12, pages 4893–4901, 1969. 71

[Hüger 2008] E. Hüger, U. Tietze, D. Lott, H. Bracht, D. Bougeard, E. E. Haller and H. Schmidt. *Self-diffusion in germanium isotope multilayers at low temperatures*. Applied Physics Letters, vol. 93, no. 16, page 162104, 2008. 107, 108, 125

[Istratov 1999] Andrei A. Istratov and Oleg F. Vyvenko. *Exponential analysis in physical phenomena*. Review of Scientific Instruments, vol. 70, no. 2, pages 1233–1257, 1999. 19

[Jain 2002] S. C. Jain, W. Schoenmaker, R. Lindsay, P. A. Stolk, S. Decoutere, M. Willander and H. E. Maes. *Transient enhanced diffusion of boron in Si*. Journal of Applied Physics, vol. 91, no. 11, pages 8919–8941, 2002. 108

[Janke 2007] C. Janke, R. Jones, S. Öberg and P. R. Briddon. *Supercell and cluster density functional calculations of the thermal stability of the divacancy in germanium*. Physical Review B (Condensed Matter and Materials Physics), vol. 75, no. 19, page 195208, 2007. 68

[Khirunenko 1995] L.I. Khirunenko, N.A. Tripachko, V.I. Shakhovtsov, V.I. Yashnik and V.V. Shumov. *EPR and IR Absorption of Defects in Isotopically Enriched Germanium*. Materials Science Forum, vol. 196-201, pages 167–172, 1995. 54

[Kolkovsky 2007] Vl. Kolkovsky, M. Christian Petersen and A. Nylandsted Larsen. *Alpha-particle irradiation-induced defects in n-type germanium*. Applied Physics Letters, vol. 90, no. 11, page 112110, 2007. 71

[Kolkovsky 2008a] Vl. Kolkovsky, M. Christian Petersen, A. Nylandsted Larsen and A. Mesli. *No trace of divacancies at room temperature in germanium*. Materials Science in Semiconductor Processing, vol. 11, no. 5-6, pages 336 – 339, 2008. E-MRS 2008 Spring Conference Symposium J: Beyond Silicon Technology: Materials and Devices for Post-Si CMOS. 86

[Kolkovsky 2008b] Vl. Kolkovsky, M. Christian Petersen, A. Mesli, J. Van Gheluwe, P. Clauws and A. Nylandsted Larsen. *Gallium interstitial in irradiated germanium: Deep level transient spectroscopy*. Physical Review B (Condensed Matter and Materials Physics), vol. 78, no. 23, page 233201, 2008. 89

[Kuitunen 2008] K. Kuitunen, F. Tuomisto, J. Slotte and I. Capan. *Divacancy clustering in neutron-irradiated and annealed n-type germanium*. Physical Review B (Condensed Matter and Materials Physics), vol. 78, no. 3, page 033202, 2008. 69, 86, 88

[Lang 1974a] D. V. Lang. *Deep-level transient spectroscopy: A new method to characterize traps in semiconductors*. Journal of Applied Physics, vol. 45, no. 7, pages 3023–3032, 1974. 16

[Lang 1974b] D. V. Lang and L. C. Kimerling. *Observation of Recombination-Enhanced Defect Reactions in Semiconductors*. Phys. Rev. Lett., vol. 33, no. 8, pages 489–492, Aug 1974. 94

[Larsen 2006] A. Nylandsted Larsen, A. Mesli, K. Bonde Nielsen, H. Kortegaard Nielsen, L. Dobaczewski, J. Adey, R. Jones, D. W. Palmer, P. R. Briddon and S. Öberg. *E Center in Silicon Has a Donor Level in the Band Gap*. Physical Review Letters, vol. 97, no. 10, page 106402, 2006. 88

[Larsen 2008] A. Nylandsted Larsen, A. Bro Hansen and A. Mesli. *Irradiation-induced defects in SiGe*. Materials Science and Engineering: B, vol. 154-155, pages 85 – 89, 2008. Front-End Junction and Contact Formation in Future Silicon/Germanium Based Devices. 69, 89

[Lindberg 2005] C. E. Lindberg, J. Lundsgaard Hansen, P. Bomholt, A. Mesli, K. Bonde Nielsen, A. Nylandsted Larsen and L. Dobaczewski. *The antimony-vacancy defect in p-type germanium*. Applied Physics Letters, vol. 87, no. 17, page 172103, 2005. 88, 99

[Loferski 1958] J. J. Loferski and P. Rappaport. *Radiation Damage in Ge and Si Detected by Carrier Lifetime Changes: Damage Thresholds*. Phys. Rev., vol. 111, no. 2, pages 432–439, Jul 1958. 9, 70

[Macfarlane 1957] G. G. Macfarlane, T. P. McLean, J. E. Quarrington and V. Roberts. *Fine Structure in the Absorption-Edge Spectrum of Ge*. Phys. Rev., vol. 108, no. 6, pages 1377–1383, Dec 1957. 4

[Markevich 2002] V. P. Markevich, I. D. Hawkins, A. R. Peaker, V. V. Litvinov, L. I. Murin, L. Dobaczewski and J. L. Lindström. *Electronic properties of vacancy–oxygen complex in Ge crystals*. Applied Physics Letters, vol. 81, no. 10, pages 1821–1823, 2002. 95, 97, 98, 99, 100

[Markevich 2003] V. P. Markevich, A. R. Peaker, L. I. Murin and N. V. Abrosimov. *Vacancy–oxygen complex in $Si_{1-x}Ge_x$ crystals*. Applied Physics Letters, vol. 82, no. 16, pages 2652–2654, 2003. 69

[Markevich 2004a] V. P. Markevich, I. D. Hawkins, A. R. Peaker, K. V. Emtsev, V. V. Emtsev, V. V. Litvinov, L. I. Murin and L. Dobaczewski. *Vacancy–group-V-impurity atom pairs in Ge crystals doped with P, As, Sb, and Bi*. Phys. Rev. B, vol. 70, no. 23, page 235213, Dec 2004. 88

[Markevich 2004b] V. P. Markevich, A. R. Peaker, V. V. Litvinov, V. V. Emtsev and L. I. Murin. *Electronic properties of antimony-vacancy complex in Ge crystals*. Journal of Applied Physics, vol. 95, no. 8, pages 4078–4083, 2004. 22, 82, 88, 99

[Mesli 2008] A. Mesli, L. Dobaczewski, K. Bonde Nielsen, Vl. Kolkovsky, M. Christian Petersen and A. Nylandsted Larsen. *Low-temperature irradiation-induced defects in germanium: In situ analysis*. Physical Review B (Condensed Matter and Materials Physics), vol. 78, no. 16, page 165202, 2008. 54, 57, 61, 62, 64, 89

[Mikelsen 2005] M. Mikelsen, E. V. Monakhov, G. Alfieri, B. S. Avset and B. G. Svensson. *Kinetics of divacancy annealing and divacancy-oxygen formation in oxygen-enriched high-purity silicon*. Phys. Rev. B, vol. 72, no. 19, page 195207, Nov 2005. 85

[Miller 1977] G L Miller, D V Lang and L C Kimerling. *Capacitance Transient Spectroscopy*. Annual Review of Materials Science, vol. 7, no. 1, pages 377–448, 1977. 11

[Molle 2006] Alessandro Molle, Md. Nurul Kabir Bhuiyan, Grazia Tallarida and Marco Fanciulli. *Formation and stability of germanium oxide induced by atomic oxygen exposure*. Materials Science in Semiconductor Processing, vol. 9, no. 4-5, pages 673 – 678, 2006. Proceedings of Symposium T E-MRS 2006 Spring Meeting on Germanium based semiconductors from materials to devices. 109

[Morin 1954] F. J. Morin and J. P. Maita. *Conductivity and Hall Effect in the Intrinsic Range of Germanium*. Phys. Rev., vol. 94, no. 6, pages 1525–1529, Jun 1954. 4, 6, 114

[Nagesh 1988] V. Nagesh and J. W. Farmer. *Study of irradiation-induced defects in germanium*. Journal of Applied Physics, vol. 63, no. 5, pages 1549–1553, 1988. 72

[Nielsen 1996] K. Bonde Nielsen and E. Andersen. *Significance of blackbody radiation in deep-level transient spectroscopy*. Journal of Applied Physics, vol. 79, no. 12, pages 9385–9387, 1996. 43

[Nielsen 2003] H. Kortegaard Nielsen, B. G. Svensson, J.-J. Goubet and A. Nylandsted Larsen. *Electrically active defects in silicon produced by ion channeling*. Applied Physics Letters, vol. 82, no. 22, pages 3865–3867, 2003. 75

[Peaker 2005] A.R. Peaker, V.P. Markevich, L.I. Murin, N.V. Abrosimov and V.V. Litvinov. *Ion implantation and electron irradiation damage in unstrained germanium and silicon-germanium alloys*. Materials Science and Engineering: B, vol. 124-125, pages 166 – 169, 2005. EMRS 2005, Symposium D - Materials Science and Device Issues for Future Technologies. 74, 76, 105

[Pedersen 1999] T. P. Leervad Pedersen, A. Nylandsted Larsen and A. Mesli. *Carbon-related defects in proton-irradiated, n-type epitaxial $Si_{1-x}Ge_x$*. Applied Physics Letters, vol. 75, no. 26, pages 4085–4087, 1999. 103

[Pells 1969] G P Pells and M Shiga. *The optical properties of copper and gold as a function of temperature*. Journal of Physics C: Solid State Physics, vol. 2, no. 10, page 1835, 1969. 23

[Petersen 2006] M. Christian Petersen, C.E. Lindberg, K. Bonde Nielsen, A. Mesli and A. Nylandsted Larsen. *DLTS studies of irradiation-induced defects in p-type germanium*. Materials Science in Semiconductor Processing, vol. 9, no. 4-5, pages 597 – 599, 2006. Proceedings of Symposium T E-MRS 2006 Spring Meeting on Germanium based semiconductors from materials to devices. 81

[Pinto 2006] H.M. Pinto, J. Coutinho, V.J.B. Torres, S. Öberg and P.R. Briddon. *Formation energy and migration barrier of a Ge vacancy from ab initio studies*. Materials Science in Semiconductor Processing, vol. 9, no. 4-5, pages 498 – 502, 2006. Proceedings of Symposium T E-MRS 2006 Spring Meeting on Germanium based semiconductors from materials to devices. 55

[Posselt 2000] Matthias Posselt, Bruno Schmidt, Thomas Feudel and Norbert Strecker. *Atomistic simulation of ion implantation and its application in Si technology*. Materials Science and Engineering B, vol. 71, no. 1-3, pages 128 – 136, 2000. 75

[Poulin 1980] F. Poulin and J.C. Bourgoin. *Threshold energy for atomic displacement in electron irradiated germanium*. Rev. Phys. Appl. (Paris), vol. 15, no. 1, pages 15–19, 1980. 72

[Riihimäki 2007] I. Riihimäki, A. Virtanen, S. Rinta-Anttila, P. Pusa, J. Räisänen and The ISOLDE Collaboration. *Vacancy-impurity complexes and diffusion of Ga and Sn in intrinsic and p-doped germanium*. Applied Physics Letters, vol. 91, no. 9, page 091922, 2007. 108, 121, 123, 128

[Shimizu 2007] Yasuo Shimizu, Masashi Uematsu and Kohei M. Itoh. *Experimental Evidence of the Vacancy-Mediated Silicon Self-Diffusion in Single-Crystalline Silicon*. Physical Review Letters, vol. 98, no. 9, page 095901, 2007. 107

[Silvestri 2006] H. H. Silvestri, H. Bracht, J. Lundsgaard Hansen, A. Nylandsted Larsen and E. E. Haller. *Diffusion of silicon in crystalline germanium*. Semiconductor Science Technology, vol. 21, pages 758–762, June 2006. 109, 111, 112

[Srour 2003] J.R. Srour, C.J. Marshall and P.W. Marshall. *Review of displacement damage effects in silicon devices*. Nuclear Science, IEEE Transactions on, vol. 50, no. 3, pages 653–670, June 2003. 9

[Sze 1981] SM Sze. Physics of semiconductor devices. New York: John Wiley and sons, 2nd ed. édition, 1981. 22

[Troxell 1980] J. R. Troxell and G. D. Watkins. *Interstitial boron in silicon: A negative-U system*. Phys. Rev. B, vol. 22, no. 2, pages 921–931, Jul 1980. 95

[Uppal 2004] Suresh Uppal, Arthur F. W. Willoughby, Janet M. Bonar, Nick E. B. Cowern, Tim Grasby, Richard J. H. Morris and Mark G. Dowsett. *Diffusion of boron in germanium at 800–900°C*. Journal of Applied Physics, vol. 96, no. 3, pages 1376–1380, 2004. 120, 125

[Vanhellemont 2007] Jan Vanhellemont, Piotr Spiewak and Koji Sueoka. *On the solubility and diffusivity of the intrinsic point defects in germanium*. Journal of Applied Physics, vol. 101, no. 3, page 036103, 2007. 107

[Vogel 1983] G Vogel, G Hettich and H Mehrer. *Self-diffusion in intrinsic germanium and effects of doping on self-diffusion in germanium*. Journal of Physics C: Solid State Physics, vol. 16, no. 32, page 6197, 1983. 107

[Waite 1957] T. R. Waite. *Theoretical Treatment of the Kinetics of Diffusion-Limited Reactions*. Phys. Rev., vol. 107, no. 2, pages 463–470, Jul 1957. 73

[Watkins 1965] G. D. Watkins and J. W. Corbett. *Defects in Irradiated Silicon: Electron Paramagnetic Resonance of the Divacancy*. Phys. Rev., vol. 138, no. 2A, pages A543–A555, Apr 1965. 68

[Watkins 2000] George D. Watkins. *Intrinsic defects in silicon*. Materials Science in Semiconductor Processing, vol. 3, no. 4, pages 227 – 235, 2000. 53, 54, 55, 58, 64, 65, 89

[Werner 1985] M. Werner, H. Mehrer and H. D. Hochheimer. *Effect of hydrostatic pressure, temperature, and doping on self-diffusion in germanium*. Phys. Rev. B, vol. 32, no. 6, pages 3930–3937, Sep 1985. 107

[Zangenberg 2002] N. Zangenberg, J.J. Goubet and A. Nylandsted Larsen. *On-line DLTS investigations of the mono-and di-vacancy in p-type silicon after low temperature electron irradiation*. Nuclear Inst. and Methods in Physics Research, B, vol. 186, no. 1-4, pages 71–77, 2002. 26

[Ziegler 2008] James F. Ziegler. *The Stopping and Range of Ions in Matter (SRIM)*. `http://www.srim.org`, 2008. 9

[Zillgen 1997] H. Zillgen and P. Ehrhart. *Bound vacancy interstitial pairs in irradiated silicon*. Nuclear Instruments and Methods in Physics Research Section B: Beam Interactions with Materials and Atoms, vol. 127-128, pages 27 – 31, 1997. Ion Beam Modification of Materials. 63